Theoretical investigation of ferroic instabilities in confined geometries and distorted lattices

Ruihao Qiu

Ecole Doctorale des Sciences Chimiques, Université de Bordeaux
Ecole Doctorale de Physique, Université de Liège

Theoretical investigation of ferroic instabilities in confined geometries and distorted lattices

A thesis submitted for the degree of
PhilosophiæDoctor (PhD) in Sciences

by

Ruihao QIU

Supervisor:
Dr. Eric BOUSQUET
Co-supervisors:
Dr. Andrés CANO
Prof. Antoine VILLESUZANNE
Jury members:
Prof. Philippe GHOSEZ (Secrétaire)
Dr. Maël GUENNOU
Prof. Sverre Magnus SELBACH
Prof. Virginie SIMONET (Président)
Dr. Zeila ZANOLLI

10. 2017

Acknowledgements

The key to growth is the introduction of higher dimensions of consciousness into our awareness.

– Lao Tsu

When I first arrived Bordeaux, Andrés picked me up at the train station and led me to the city center. To be honest, it took me a while to fully understand his English with Spanish accent. However, it has been already three years, I am still not able to know how deep is his comprehension in physics and in the world. Working with him is of great pleasure, our discussions always induce the "phase transition" – from unknown to known. He is patient and tolerant of my ignorance, weakness and limits, keeps pushing me to go beyond.

When I arrived Liège, the same thing happened. It was Eric, who picked me up and showed me the way. Eric is always curious, passionate and enthusiastic, with a lot of ideas in sciences and stories in life. I never felt tired while working with him. He told me a good wine need to be balanced, in the meantime, he showed me how a good life is balanced.

I am truly grateful that they "picked me up and showed me the way", supported me all along and made me independent. As Andrés said, a PhD will have a "strange" relation with his supervisor in his whole life.

I would like to express my sincere appreciation to Philippe and Antoine, for their continues supports and a lot of helps during my PhD.

Big thanks to our big family in Liège, Fabio, Alexandre, Alain, Karandeep, Xu, Yajun, Hanen, Danila, Marcus, Sébastien, Camilo, Sergei, Naihua, Matthius, Zeila, Antoine, Nick, Thomas. We had a lot of great moments together, cooking, coffee&tea break, discussing, laughing, ...

Many thanks to my flatmates and friends, Beatrize, Jenny, Karine, Ricarda and Nick, we share our foods, cultures, experiences and opinions.

Thanks to Kostantin and our team Fischer, without climbing, beer and these guys, life will be boring.

I feel really lucky to meet all these smart and lovely people, they introduce the "higher dimensions" into my life, makes me growing quickly.

Finally, I would like to thank to my family for their constant love and support.

Contents

Introduction

Multiferroics are generally defined as the materials that exhibit more than one of the ferroic order parameters – (anti-)ferromagnetism, ferroelectricity, ferroelasticity and ferrimagnetism – in the same phase. In a restricted sense, the term multiferroics is frequently used to describe the magnetoelectric multiferroics, in which ferroelectricity and (anti-)ferromagnetism coexist. Ferroelectricity and (anti-)ferromagnetism are two particular examples of long-rage order.

A very insightful understanding of multiferroic phenomena has emerged from first-principles calculations based on Density Functional Theory (DFT), which have experienced an enormous and fruitful development in recent years [1, 2, 3]. They enable the investigation of the electronic and structural properties in a variety of materials. Particularly for multiferroics, microscopic calculations on the relevant properties, such as the spontaneous polarization and magnetic moments, become accessible [4, 5]. They also allow the determination of the coupling constants and other input parameters that can be subsequently used to formulate Landau-like models and effective Hamiltonians. A spectacular achievement concerns the correct descriptions of the sequence of both ferroelectric and magnetic phase transitions, revealing the microscopic origins of these transitions.

At the same time, the Landau theory of phase transition continues to be very helpful especially in the context of multiferroics, where the coupling between different order parameters plays a crucial role. By construction, it is also a very suitable approach to describe the emergence of long-range modulated orders and multi-domain structures. This theory builds the foundations of a more general theory from simple but very deep concepts. In particular, it exploits the fact that, when a system approaches a continuous phase transition (or critical point), the correlation length diverges and hence the microscopic details of the system become no longer important. Instead, the initial symmetry and how it changes as a result of the transition are important. These ideas happen to be fruitful and universal. Different phase transitions having the same initial and final symmetries are isomorphic. Also, it indicates that the amplitude of irreducible representation of the initial symmetry group emerging after transition can be taken as a measure of the symmetry breaking (i.e. the order parameter) [6, 7].

In this thesis, we exploit these two approaches to investigate the ferroic instabilities in confined geometries and distorted lattices. In Chapter 1, we give a brief introduction on the phenomenological descriptions and the microscopic model on ferroelectricity and the magnetic orders appear in rare-earth manganites. In Chapter 2, we introduce and describe the first-principles calculations within the DFT framework. In Chapter 3, we consider structural instabilities in standard ferroelectrics confined to novel nanotube and nanoshell geometries. Here, the Landau-like description provides a very convenient framework to describe the the competition between different instabilities, which include vortex-like distributions of polarization. In Chapter 4, we consider magnetic instabilities rare-earth manganites under pressure. These systems represent a model-case family of multiferroic materials, and we use first-principles calculations to predict novel ground states that can be induced by pressure. In Chapter 5, we extend this study to thin films to demonstrate that their ground state properties can also be tuned by means of epitaxial strain.

1

Fundamentals of (multi-)ferroics

1.1 Phenomenological description of ferroelectricity

We start by discussing different type of ferroelectrics according to their phenomenological description in terms of Landau theory, namely, proper, improper and pseudo-proper ferroelectrics. The Landau theory of phase transitions is constructed near the phase transition point from the Taylor series expansion of an effective thermodynamic potential in terms of a primary parameter [5, 8, 9, 10, 11, 12]. The above three cases are distinguished from the physical meaning of this order parameter, which directly determines the symmetry breaking associated to the transition and hence the new physical properties that emerge as a result of it.

1.1.1 Proper ferroelectrics

If the primary order parameter can be directly associated to the electric polarization P, then we have the case of a proper ferroelectric. We start by reviewing some basic features of this case, which will be further developed in Chapter 3 to take into account finite-size effects related to specific geometries such as the nanotube geometry. For the moment, we restrict ourselves to the case of uniform polarization in an infinite system. Thus, near the phase transition point, we expand the Landau free energy as:

$$F(T,P) = F_0(T) + \frac{1}{2}a(T)P^2 + \frac{1}{4}b(T)P^4. \tag{1.1}$$

Here F_0 represents the free energy of the initial (high-symmetry) state and, for the sake of concreteness, we assume that temperature represents the control parameter. Since the free energy is a scalar quantity that is invariant under the space-inversion symmetry operation, the free energy expansion cannot contain odd powers of P. In order to describe a second-order transition at $T = T_c$, we assume that the sign of the coefficient a changes from positive to negative in continuous way (so that it vanishes at T_c), while the coefficient b

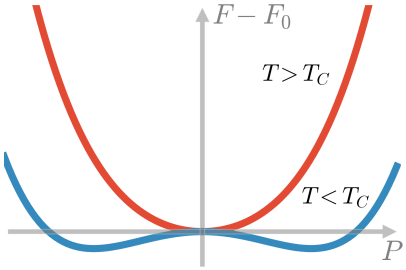

Figure 1.1: The Landau free energy as a function of the order parameter P at $T > T_c$ and $T < T_c$.

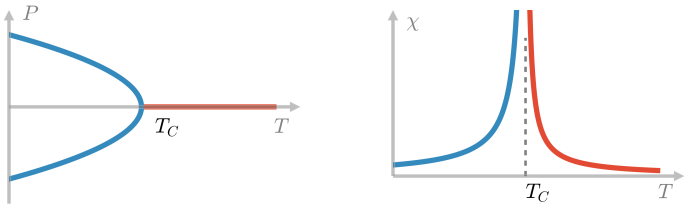

(a) (b)

Figure 1.2: Temperature dependence of (a) the order parameter P and (b) the electric susceptibility χ for proper ferroelectrics.

stays positive. Thus, near T_c, it suffices to consider the first-order terms in the expansion of these coefficients: $a = a'(T - T_c)$ with $(a' > 0)$, and $b(T) = b(T_c) = const.$ In Figure 1.1 we show the resulting (non-equilibrium) free energy as a function of the order parameter P. If $T > T_c$ $(a > 0)$, the energy displays only one minimum that corresponds to $P = 0$. If $T < T_c$ $(a < 0)$, however, we obtain two symmetric minima that correspond to $P \neq 0$. These equilibrium values of polarization are determined by the conditions of minimization of the free energy:

$$\frac{\partial F}{\partial P} = 0, \tag{1.2}$$

$$\frac{\partial^2 F}{\partial P^2} > 0. \tag{1.3}$$

From these conditions, we obtain the expression for the polarization

$$P = \begin{cases} 0 & (T \geq T_c) \\ \pm\sqrt{\frac{a'|T - T_c|}{b}} & (T \leq T_c) \end{cases}. \tag{1.4}$$

We plot the polarization as a function of temperature in Fig. 1.2(a), which shows that there are two nonzero equilibria P corresponding to each temperature.

Then we consider a case that an external electric field is applied on the system. An

additional coupling term $-EP$ should be taken into account in the free energy, which is written as

$$F(T,P) = F_0(T) + \frac{1}{2}a'(T-T_c)P^2 + \frac{1}{4}bP^4 - EP. \tag{1.5}$$

By minimizing the free energy with respect to the polarization, we get

$$\frac{\partial F}{\partial P} = a'(T-T_c)P + bP^3 - E = 0. \tag{1.6}$$

Then, we differentiate this equation with respect to E,

$$a'(T-T_c)\frac{\partial P}{\partial E} + 3bP^2\frac{\partial P}{\partial E} - 1 = 0. \tag{1.7}$$

Therefore we obtain the electric susceptibility

$$\chi = \frac{\partial P}{\partial E} = \frac{1}{a'(T-T_c) + 3bP^2}. \tag{1.8}$$

By using expression (1.4), we find

$$\chi = \begin{cases} \frac{1}{a'(T-T_c)} & (T \geq T_c) \\ -\frac{1}{2a'(T-T_c)} & (T \leq T_c) \end{cases}. \tag{1.9}$$

In Figure 1.2(b), we plot the electric susceptibility, which shows that it is divergent at transition temperature T_c and and obeys "the 1/2 law" [13].

When the temperature is slightly higher than T_c, the dielectric constant is $\varepsilon \approx 4\pi\chi$ ($\chi \gg 1$). Thus, the temperature dependence of dielectric constant can be described by the Curie-Weiss law

$$\varepsilon = \frac{C}{T-T_c}, \tag{1.10}$$

where C is Curie-Weiss constant related to the Landau coefficients and the transition temperature T_c is called Curie temperature or Curie point.

1.1.2 Improper ferroelectrics

In the case of improper ferroelectrics, the primary order parameter is a different variable, say Q, and the electric polarization is just a by-product of it [12]. This situation takes place in the magnetically-induced ferroelectrics that we will study in Chapters 4 and 5. For the sake of simplicity, let us compare the basic properties of these ferroelectrics and the standard ones by considering the Landau free energy

$$F(T,P) = F_0(T) + \frac{1}{2}aP^2 + \frac{1}{2}AQ^2 + \frac{1}{4}BQ^4 - \lambda PQ^2. \tag{1.11}$$

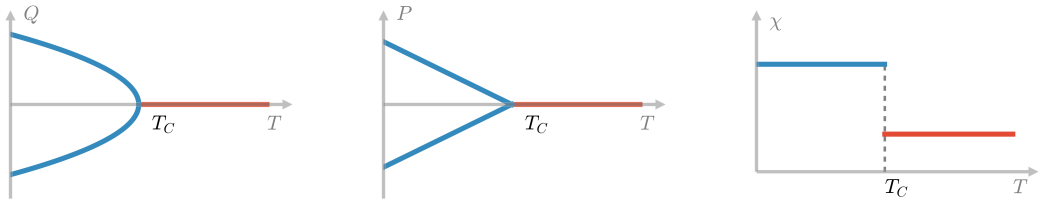

(a) (b) (c)

Figure 1.3: Temperature dependence of the order parameter (a) Q and (b) P and (c) the electric susceptibility χ for improper ferroelectrics.

Here, the nominal polarization stiffness a can be assumed to be constant so that there is no ferroelectric instability. Instead, the phase transition is due to the spontaneous emergence of the quantity Q. Accordingly, we can take $A = A'(T - T_c)$ and B as a positive constant. The coefficient λ, in its turn, describes the coupling between the electric polarization and the primary order parameter of the transition Q. In general, this quantity is a multicomponent quantity $Q = (Q_1, Q_2, \dots)$. However, here we restrict ourselves to one particular direction in order-parameter space [say $Q = (Q, 0, \dots)$] assuming that the coupling to P involves the square of the Q components only. The latter is eventually determined by the symmetry properties of these variables.

The minimization of the free energy (1.11) implies

$$\frac{\partial F}{\partial P} = aP - \lambda Q^2 = 0, \tag{1.12}$$

$$\frac{\partial F}{\partial Q} = AQ + BQ^3 - 2\lambda PQ = 0. \tag{1.13}$$

According to these equations we obtain

$$Q = \begin{cases} 0 & (T \geq T_c) \\ \pm\sqrt{\frac{A'|T-T_c|}{B'}} & (T \leq T_c) \end{cases}, \tag{1.14}$$

where $B' = B - 2\lambda^2/a$, and the electric polarization is

$$P = \frac{\lambda Q^2}{a} = \begin{cases} 0 & (T \geq T_c) \\ \frac{\lambda A'|T-T_c|}{aB} & (T \leq T_c) \end{cases}. \tag{1.15}$$

In Figure 1.3(a) and (b), we plot the order parameter P and Q as a function of temperature respectively. The order parameter Q in this case have the similar dependence of temperature as P in proper case [see Fig. 1.2]. However, the polarization in improper case becomes linear below the critical point [see Fig. 1.3(b)]. There are two ferroelectric domains, the positive and the negative one, which correspond to $Q = (Q, 0)$ and $Q = (0, Q)$ respectively.

In the presence of an external electric field, we have the additional term $-EP$ in the free energy:

$$F(T,P) = F_0(T) + \frac{1}{2}aP^2 + \frac{1}{2}AQ^2 + \frac{1}{4}BQ^4 - \lambda PQ^2 - EP. \tag{1.16}$$

The minimization of the free energy now implies

$$\frac{\partial F}{\partial P} = aP - \lambda Q^2 - E = 0, \tag{1.17}$$
$$\frac{\partial F}{\partial Q} = AQ + BQ^3 - 2\lambda PQ = 0. \tag{1.18}$$

The variation of these two equations (1.17) and (1.18) with respect to the electric field gives

$$a\frac{\partial P}{\partial E} - 2\lambda Q\frac{\partial Q}{\partial E} = 1, \tag{1.19}$$
$$-2\lambda Q\frac{\partial P}{\partial E} + (A + 3BQ^2 - 2\lambda P)\frac{\partial Q}{\partial E} = 0.. \tag{1.20}$$

Substitute the expressions of Q and P [see Eq. (1.14) and (1.15)] into these two equations, we have

$$\chi = \begin{cases} \frac{1}{a} & (T \geq T_c) \\ \frac{1}{a}(1 + \frac{\lambda^2}{aB'}) & (T \leq T_c) \end{cases}, \tag{1.21}$$

where B' has been defined above. According to these functions, in Figure 1.3(c), we plot the electric susceptibility of the improper ferroelectrics as a function of temperature. We can see that, the behavior of susceptibility of improper case is totally different with the proper one. It is constant with a jump of $\frac{\lambda^2}{a^2B'}$ at the critical point.

1.1.3 Pseudo-proper ferroelectrics

In addition to proper and improper ferroelectrics, it is sometimes useful to distinguish a third "intermediate" case: the pseudo-proper case. In this case, even if P is "qualified" to be the primary order parameter from the symmetry point of view, it turns out to be more physical to identify the primary order parameter to another quantity, Q, with the same symmetry properties but a different physical meaning. This will be the case of the spin-spiral ferroelectrics studied in Sec. 1.2.3.1. In this case, the Landau free energy can be taken in the form

$$F(T,P) = F_0(T) + \frac{1}{2}aP^2 + \frac{1}{2}AQ^2 + \frac{1}{4}BQ^4 - \lambda PQ. \tag{1.22}$$

where a and B are positive constants and $A = A'(T - T_0)$, T_0 is the critical temperature of Q in absent of P. Here the coupling between P and Q is bilinear owing the fact that

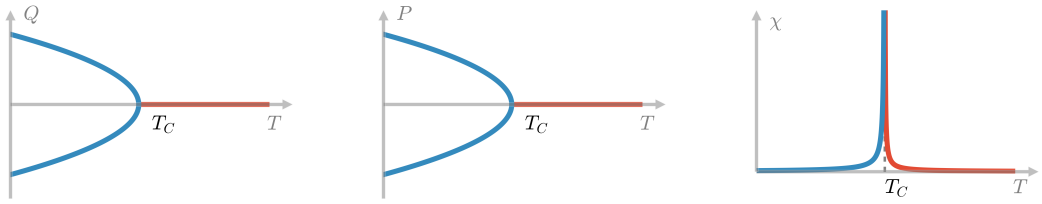

(a) (b) (c)

Figure 1.4: Temperature dependence of the order parameter (a) Q and (b) P and (c) the electric susceptibility χ for pseudo-proper ferroelectrics.

these quantities have the same symmetry properties.

The minimization of the free energy now implies:

$$\frac{\partial F}{\partial P} = aP - \lambda Q = 0, \tag{1.23}$$

$$\frac{\partial F}{\partial Q} = AQ + BQ^3 - \lambda P = 0. \tag{1.24}$$

Then we obtain:

$$Q = \begin{cases} 0 & (T \geq T_c) \\ \pm\sqrt{\frac{A'|T-T_c|}{B}} & (T \leq T_c) \end{cases}, \tag{1.25}$$

and

$$P = \frac{\lambda}{a}Q = \begin{cases} 0 & (T \geq T_c) \\ \pm\frac{\lambda}{a}\sqrt{\frac{A'|T-T_c|}{B}} & (T \leq T_c) \end{cases}. \tag{1.26}$$

Here we have set $A = A'(T - T_c) + \frac{\lambda^2}{a}$, where T_c is the critical temperature of Q by considering the coupling term. There is a shift between T_c and T_0: $T_c = T_0 + \frac{\lambda^2}{aA'}$. In Figure 1.4 (a) and (b), we plot the temperature dependence of the order parameter Q and P respectively. We find that both order parameter Q and P have the similar behavior as P in proper ferroelectrics [see Fig. 1.2(a)].

By considering an external electric field, we have

$$F(T, P) = F_0(T) + \frac{1}{2}aP^2 + \frac{1}{2}AQ^2 + \frac{1}{4}BQ^4 - \lambda PQ - EP. \tag{1.27}$$

Following the same process as the improper case [see Sec. 1.1.2],

$$\frac{\partial F}{\partial P} = aP - \lambda Q - E = 0, \tag{1.28}$$

$$\frac{\partial F}{\partial Q} = AQ + BQ^3 - \lambda P = 0. \tag{1.29}$$

The variation of both equations with respect to the electric field:

$$a\frac{\partial P}{\partial E} - \lambda\frac{\partial Q}{\partial E} = 1, \tag{1.30}$$

$$-\lambda\frac{\partial P}{\partial E} + (A + 3BQ^2)\frac{\partial Q}{\partial E} = 0. \tag{1.31}$$

By considering the expression of Q in Eq. (1.25), we obtain the electric susceptibility:

$$\chi = \begin{cases} \frac{1}{a} + \frac{\lambda^2}{a^2}\frac{1}{A'(T-T_c)} & (T \geq T_c) \\ \frac{1}{a} - \frac{\lambda^2}{a^2}\frac{1}{2A'(T-T_c)} & (T \leq T_c) \end{cases}. \tag{1.32}$$

In Fig. 1.4(c), we show the temperature dependence of the electric susceptibility. It has a similar behavior as that in the proper case. However, near T_c, the divergence of the susceptibility is more narrow and sharp due to the factor λ^2/a^2. When the temperature is such that $|T - T_c|$ and $|T - T_0| \gg 0$, then the susceptibility tends to its nominal value $\frac{1}{a}$.

1.2 Magnetic order in rare-earth manganites

In Chapters 4 and 5 we will focus on the magnetism of the rare-earth manganites $TbMnO_3$ and $EuMnO_3$, and consider also that of the rare-earth ferrites in Appendix. This type of perovskite generally displays a very rich phase diagram in which various magnetic orders compete with each other. These orders include inversion-symmetry breaking orders that give rise to multiferroicity, and also other ones that preserve this symmetry. Since the competition between all these orders will be crucial in our investigation of these systems, we find it convenient to give a brief overview of the overall experimental situation in this Section.

In Figure 1.5 we show the original *Pbnm* crystal structure of the RMO_3 systems of our interest and its cubic prototype, R is a lanthanide (rare-earth) ion and M is a transition-metal element. The *Pbnm* structure can be viewed as deriving from cubic perovskite prototype, where the M ion occupies the centre of the oxygen octahedron, and the R ion takes up the centre of the cage formed by octahedron. The structure distortion is affected by the size of R and M ion cooperatively. A convenient measure of the distortion can be indicated by the Goldschmidt tolerance factor $t = (r_R + r_O)/[\sqrt{2}(r_M + r_O)]$. $t = 1$ corresponds to a perfect cubic phase. When $t < 1$, the symmetry is reduced to orthorhombic phase with space group *Pbnm*. This occurs when the R-size decrease, and the R-O bond length shrinks, leading to the rotation and buckling of the MO_6 octahedra.

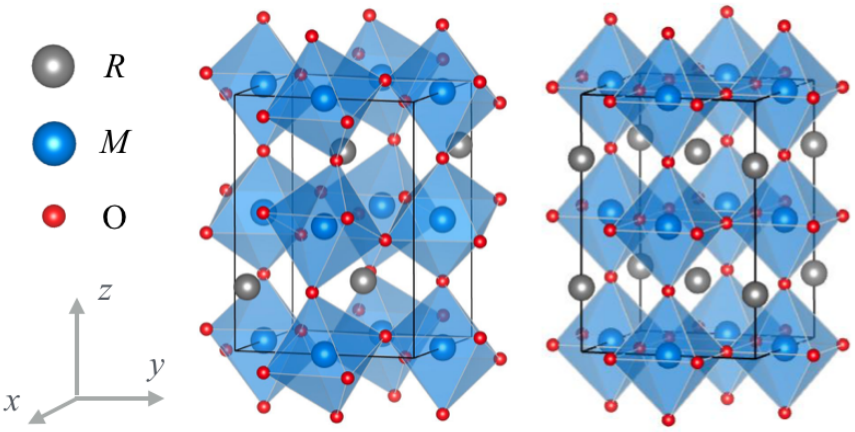

Figure 1.5: Crystal structure of orthorhombic RMO_3 with *Pbnm* space group and its cubic prototype, visualized by VESTA [14].

1.2.1 Conventional magnetic orders in perovskites

In *Pbnm* perovskites like $CaMnO_3$, the dominant interaction between the Mn spins is the isotropic exchange interaction between nearest-neighbors. Since the unit cell contains four magnetic Mn atoms, then there are four types of collinear orders that can emerge at this level depending on the relative sign of these interactions [see Fig. 1.6]:

- F-type, with all the spins pointing in the same direction (FM ordering),
- A-type, with spins pointing in opposite directions in consecutive planes (AFM order of FM planes),
- C-type, with spins pointing in opposite directions in consecutive lines (AFM order of FM chains),
- G-type, with nearest-neighboring spins pointing in opposite directions ('full' AFM ordering).

In terms of the cubic lattice with one spin per unit cell, these orders are associated to the propagation vectors $q = (0, 0, 0)$, $(0, 0, 1/2)$, $(0, 1/2, 1/2)$, and $(1/2, 1/2, 1/2)$ respectively. Alternatively, these configurations can also be defined from the relative orientation of four magnetic sublattices (one per magnetic Mn atom of the unit cell). Thus, in terms of the spin cluster depicted in Fig. 1.6, they correspond to non-zero values of the following order

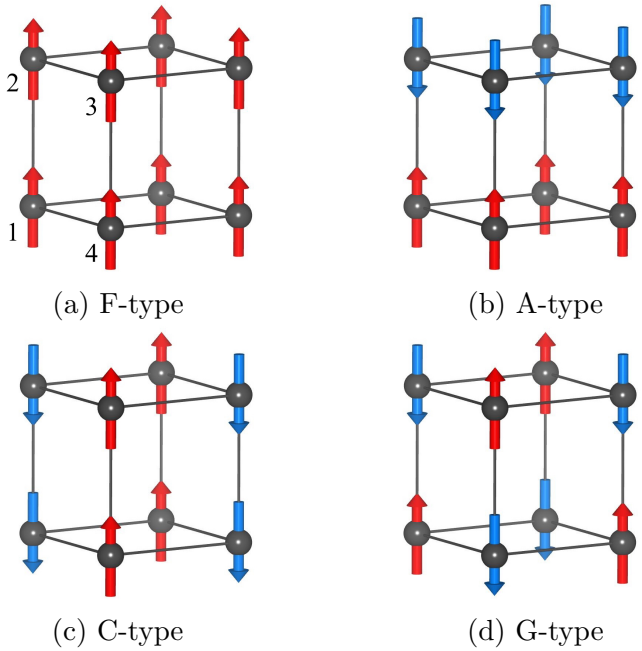

(a) F-type (b) A-type

(c) C-type (d) G-type

Figure 1.6: Conventional collinear spin orders in *Pbnm* unit cell.

parameters:

$$\mathbf{F} = \mathbf{S_1} + \mathbf{S_2} + \mathbf{S_3} + \mathbf{S_4} \tag{1.33}$$

$$\mathbf{A} = \mathbf{S_1} - \mathbf{S_2} - \mathbf{S_3} + \mathbf{S_4} \tag{1.34}$$

$$\mathbf{C} = \mathbf{S_1} + \mathbf{S_2} - \mathbf{S_3} - \mathbf{S_4} \tag{1.35}$$

$$\mathbf{G} = \mathbf{S_1} - \mathbf{S_2} + \mathbf{S_3} - \mathbf{S_4} \tag{1.36}$$

1.2.2 Experimental phase diagram in the rare-earth manganites

In Fig. 1.7, we show the experimentally-determined magnetic phase diagram of the rare-earth manganites $R\mathrm{MnO_3}$ [15, 16]. The relative complexity of this phase diagram and the emergence of additional orders compared to the ones discussed before are due to more complex interactions between spins that give rise to magnetic frustration. This will be discussed in Landau framework and microscopic model in the following sections.

Specifically, we can see that there is a first transition from the paramagnetic (PM) state to the incommensurate (IC) sinusoidal antiferromagnetic state [see Fig. 1.7], that occurs at $T_{N1} = 40 \sim 50$ K for all the systems. By lowering the temperature, Mn spins are stabilized in different type of orderings depending on the size of the rare-earth R ion, at different transition temperature T_{N2}. Four magnetoelectric phases successively appear at low temperatures by decreasing the R size.

- A-type phase with the FM Mn spins aligning in the *ab*-plane;

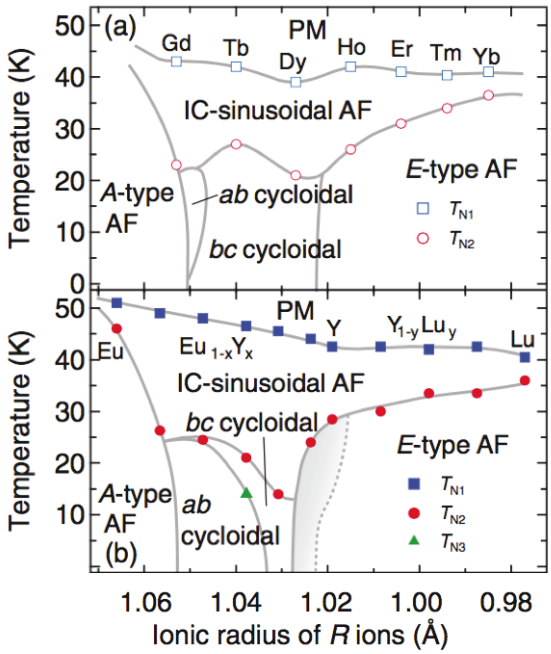

Figure 1.7: Experimentally obtained magnetoelectric phase diagram of $R\mathrm{MnO_3}$ and solid-solution systems in the plane of temperature and (effective) ionic radius of the R ion [15].

- spiral spin phase in ab-plane with $P \| a$;
- spiral spin phase in bc-plane with $P \| c$;
- collinear E-type phase with very large $P \| a$.

In all of these magnetic phases, the Mn spins along the c axis is strongly antiferromagnetically coupled. We note that, A-AFM order is the only conventional collinear order appears in the phase diagram. It is stabilized as the ground state of $\mathrm{EuMnO_3}$. However, the ground states of most of the systems are cycloidal spirals or E-AFM states, which are not conventional spin orders in perovskites.

$\mathrm{TbMnO_3}$ is one of the most studied orthorhombic rare-earth manganites and can be considered as a representative of this family. Its magnetic structure has been determined by neutron and x-ray resonant scattering experiments [17, 18, 19, 20, 21]. It undergoes successive magnetic phase transitions [see Fig. 1.7]:

$$bc \text{ cycloidal phase} \quad \overset{28K}{\longleftrightarrow} \quad \text{IC-sinusoidal AFM} \quad \overset{42K}{\longleftrightarrow} \quad \text{PM}$$

At $T_{N1} = 42$ K, the Mn spins transform into an incommensurate sinusoidal spin wave, forming a longitudinal spin-density-wave along the b direction and an AFM structure along c with the wave-vector $\mathbf{q}_{Mn} = (0,\ 0.28,\ 1)$. The Mn spins further develop a transverse component along the c-axis at $T_{N2} = 28$ K that transforms the structure into a (non-collinear) cycloidal in the bc plane. In addition, the spin order of Tb $4f$-electron at $T_N^{Tb} = 7$ K is stabilized in a cycloidal order with wave vector $\mathbf{q}_{Tb} = (0,\ 0.42,\ 1)$.

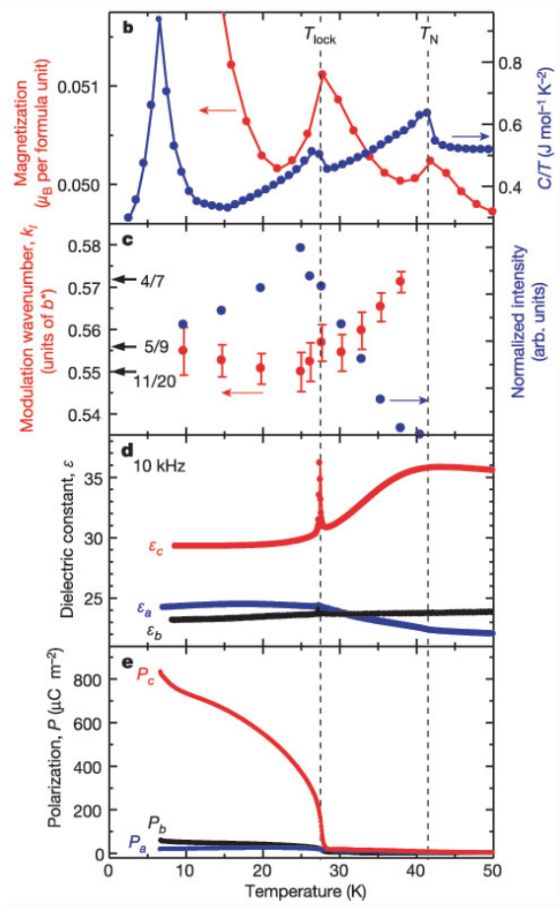

Figure 1.8: Magnetic and dielectric anomalies of $TbMnO_3$ [18].

In Fig. 1.8, we show the magnetic and dielectric anomalies of $TbMnO_3$ from experiments [18]. The anomaly in magnetization and specific heat confirms the above phase transitions. There exists a narrow divergence in the dielectric constant measurement at the second critical temperature T_{N2}, which is similar with that in pseudo-proper ferroelectrics [see Figure 1.4(c)]. The polarization starts to appear along the c direction below T_{N2}. These electric properties change during the magnetic sinusoidal $\rightarrow$ spiral phase transition, implying there is a strong magnetoelectric coupling between them.

A pressure-induced transition from the bc cycloidal spiral state to the E-AFM state has been observed at around $4 \sim 5$ GPa, accompanied with a spontaneous polarization flopping from the c to the a-axis and its amplitude increases about ten times of the magnitude [22]. Neutron diffraction and electric measurements confirm a commensurate E-AFM order stabilized in highly strained (010) oriented $TbMnO_3$ thin film grown on $YAlO_3$ substrate. The polarization of the thin film is relatively larger compared to that of the bulk materials [23]. These observations indicate that the specific E-AFM order should have stronger coupling with polarization than the cycloidal spiral.

1.2.3 Spin orders breaking inversion-symmetry

As we can see from the above experiments, the multiferroic properties of the $R\mathrm{MnO_3}$ systems trace back to the emergence of spin spirals and E-AFM orders. These two particular magnetic orders break the inversion symmetry and hence induce ferroelectricity. In the following, we briefly discuss the main features of these two orders from the phenomenological point of view.

1.2.3.1 Spin-spiral order

Emergence of the spin spiral In terms of the Landau theory, the pure magnetic free energy can be written as

$$F_m = \sum_i \frac{a_i}{2} M_i^2 + \frac{b}{4} M^4 + \frac{c}{2} \mathbf{M}(q^2 + \nabla^2)^2 \mathbf{M}. \tag{1.37}$$

Here a, b, c are the Landau coefficients of second-order, fourth-order and gradient term respectively, $\mathbf{M}$ represents the distribution of magnetization. In the following we consider the easy-axis case such that $a_x < a_y < a_z$. The last term involving the gradients comes from the magnetic frustration and takes into account that the system favors a periodic spin density wave (SDW) with vector q. We seek the distribution of magnetization in the form

$$\mathbf{M} = \sum_{\mathbf{q}} [M_x \cos(\mathbf{q} \cdot \mathbf{r}) \hat{\mathbf{x}} + M_y \sin(\mathbf{q} \cdot \mathbf{r}) \hat{\mathbf{y}} + M_z \hat{\mathbf{z}}], \tag{1.38}$$

where $\mathbf{q}$ is the propagation wave vector in reciprocal space and $\mathbf{r}$ is the position vector in real space. M_x, M_y and M_z are the components of magnetic moment along the orthogonal x, y and z axes, respectively.

For each spin density wave, $M_z = 0$ indicates a coplanar spin wave in xy-plane. Hence if either M_x or M_y is zero, it transforms to a sinusoidal wave. Specifically, when the $\mathbf{q}$ vector and $\mathbf{M}$ are along the same direction, the sinusoidal wave is longitudinal, otherwise it is transverse. In Figure 1.9(a) we plot the longitudinal wave $\mathbf{M} = M_x \sin(q_x x) \hat{\mathbf{x}}$ with both $\mathbf{M}$ and $\mathbf{q}$ along x-axis. If neither M_x nor M_y is zero, it describes a non-collinear cycloidal wave. When the $\mathbf{q}$ vector is along z-axis, *e.g.* $\mathbf{M} = M_x \cos(q_z z) \hat{\mathbf{x}} + M_y \sin(q_z z) \hat{\mathbf{y}}$, it is a longitudinal cycloidal wave. Whereas when the $\mathbf{q}$ vector lies in xy-plane, *e.g.* $\mathbf{M} = M_x \cos(q_x x) \hat{\mathbf{x}} + M_y \sin(q_x x)$, it specifies a transverse cycloidal wave, which is plotted in Fig. 1.9(b). The case of $M_z \neq 0$ indicates a three-dimensional conical spiral order with a net magnetic moment along the z-axis. It can be simply viewed as a coplanar spin density wave adding a net out-of-plane component. In Fig. 1.9(c) we plot one of the transverse conical waves, formatted as $\mathbf{M} = M_x \cos(q_x x) \hat{\mathbf{x}} + M_y \sin(q_x x) \hat{\mathbf{y}} + M_z \hat{\mathbf{z}}$ [15, 24].

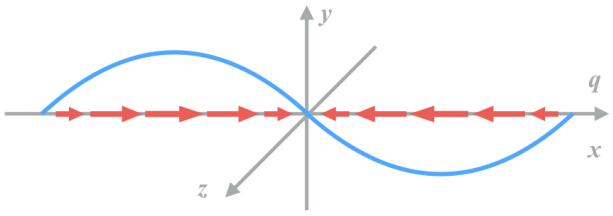

(a) Sinusoidal wave

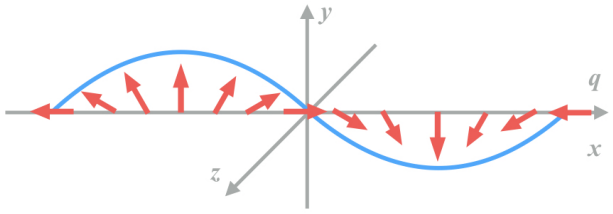

(b) Cycloidal spiral

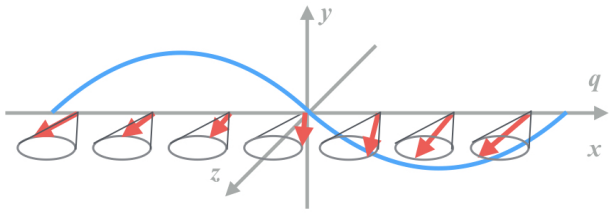

(c) Conical spiral

Figure 1.9: Three types of spin density wave from expression (1.38).

First we discuss a longitudinal sinusoidal SDW state with both **q**-vector and **M** are along x-axis [see Figure 1.9(a)]:

$$\mathbf{M} = M_x \cos(qx)\hat{\mathbf{x}}. \tag{1.39}$$

By substituting it into the magnetic free energy (1.37), we got

$$F_m = \frac{a_x}{2} M_x^2 \cos^2(qx) + \frac{b}{4} M_x^4 \cos^4(qx). \tag{1.40}$$

If we consider only the uniform term, we got

$$F_m = \frac{a_x}{4} M_x^2 + \frac{3b}{32} M_x^4. \tag{1.41}$$

If we minimize this magnetic free energy with respect to M_x, we can easily obtain

$$M_x^2 = \begin{cases} 0 & (T \geq T_{N1}) \\ -\frac{4a_x}{3b} & (T \leq T_{N1}) \end{cases}. \tag{1.42}$$

The energy minimum is

$$F_{min} = -\frac{a_x^2}{6b}, \tag{1.43}$$

when the wave vector of the sinusoidal SDW state with $M_x^2 = -\frac{4a_x}{3b}$.

Another case refers to the cycloidal SDW state [see Figure 1.9(b)] in xy-plane, formulated as

$$\mathbf{M} = M_x \cos(qx)\hat{\mathbf{x}} + M_y \sin(qx)\hat{\mathbf{y}}. \tag{1.44}$$

By substituting it into the magnetic free energy Eq. (1.37) and using Eq. (1.43), we will have

$$F_m = -\frac{a_x^2}{6b} + \frac{a_y}{2}M_y^2 \sin^2(qx) + \frac{b}{4}[2M_x^2 M_y^2 \cos^2(qx)\sin^2(qx) + M_y^4 \sin^4(qx)], \tag{1.45}$$

By neglecting the higher harmonics and using the magnetic moment M_x in Eq. (1.42), the expression becomes

$$F_m = -\frac{a_x^2}{6b} + \frac{3a_y - a_x}{12}M_y^2 + \frac{3b}{32}M_y^4. \tag{1.46}$$

By minimizing this magnetic free energy with respect to M_y, we obtain

$$M_y^2 = \begin{cases} 0 & (T \geq T_{N2}) \\ -\frac{4}{9b}(3a_y - a_x) & (T \leq T_{N2}) \end{cases}. \tag{1.47}$$

This indicates that the cycloidal ordering appears at $a_y = a_x/3$, since $a_x = a'(T - T_{N1})$ and we assume that the anisotropy parameter $\Delta = a_x - a_y$ is not too large, we have

$$T_{N2} = T_{N1} - \frac{3\Delta}{2a'} \tag{1.48}$$

At this point, the total free energy is

$$F_{min} = -\frac{a_x^2}{6b} - \frac{(a_x - 3a_y)^2}{54b}. \tag{1.49}$$

Compared with the energy of sinusoidal SDW in expression (1.43), the cycloidal state has the lowest energy at temperature lower than $T = T_{N2}$. Therefore, by the above formula, we can well explain the origin of the successive phase transitions observed in experiments, from PM to sinusoidal state at T_{N1}, then to cycloidal spiral state a T_{N2}. It is due to the successive appearance of the primary order parameters M_x and M_y by decreasing the temperature, which successively decrease the free energy of the system.

Emergence of the electric polarization We now discuss the coupling between the distribution of magnetization and the polarization, which is the origin of magnetic ferro-

electricity. This coupling can be found by using general symmetry analysis [25, 26]. The time reversal symmetry $t \to -t$, transforms $\mathbf{P} \to \mathbf{P}$ and $\mathbf{M} \to -\mathbf{M}$, requires the lowest-order coupling to be quadratic in $\mathbf{M}$. However, the spatial inversion symmetry, $\mathbf{r} \to -\mathbf{r}$, leading to $\mathbf{P} \to -\mathbf{P}$ and $\mathbf{M} \to \mathbf{M}$, is respected when the coupling between an uniform polarization and magnetization is linear in $\mathbf{P}$ and contains one gradient of $\mathbf{M}$. Therefore, the most general coupling can be written as [27]

$$F_{em} = \lambda \mathbf{P} \cdot [(\mathbf{M} \cdot \nabla)\mathbf{M} - \mathbf{M}(\nabla \cdot \mathbf{M})]. \tag{1.50}$$

Minimizing total free energy with respect to P, we obtain

$$\mathbf{P} = \frac{\lambda}{a}[(\mathbf{M} \cdot \nabla)\mathbf{M} - \mathbf{M}(\nabla \cdot \mathbf{M})]. \tag{1.51}$$

If the magnetic moments align according to a collinear pattern, either ferromagnetic (FM) or antiferromagnetic (AFM), the expression (1.51) gives a zero polarization. This result also applies the sinusoidal SDW state. However, in the case of the cycloidal order we obtain a non-zero polarization

$$< \mathbf{P} >= \frac{\lambda}{a} M_x M_y (\mathbf{z} \times \mathbf{q}). \tag{1.52}$$

since both M_x and M_y are different from zero in this state. This explains the experimental results in Fig. 1.8, in which the polarization and the cycloidal spiral state appear simultaneously at T_{N2}. Since the direction of the polarization is the cross product of the wave vector and the out-of-plane direction. The polarization induced by the *bc* cycloidal spiral in *Pbnm* structure is along the *c*-axis.

The expression (1.52) has the form $-\frac{\lambda Q^2}{a}$. Consequently, if the system transforms directly from the paramagnetic to the spiral state, we then have an improper ferroelectrics in which the susceptibility should behave as in Fig. 1.3(c). In $TbMnO_3$, however, the dielectric constant shows a large and narrow peak [see Fig. 1.8] [18]. This can be explained in terms of the phase transition process. It is not a direct transition from the paramagnetic state to the spiral state, but from the collinear sinusoidal wave to the spiral state. In this case, we have a pseudo-proper ferroelectric where the primary order parameter of the transition is $Q = M_y$ (and then the coupling effectively becomes $\lambda' PQ$).

In principle, we can build a structure for spiral spin wave with any propagation wave vector. However, more specifically and practically, we need to adapt the spiral orders into the real lattice structure for DFT calculations. In the practical implementation of the calculations, we have to simplify our models to the commensurate spirals. The spiral is limited by the size of the unit cell we use. In Figure 1.10(a) and (b), we construct

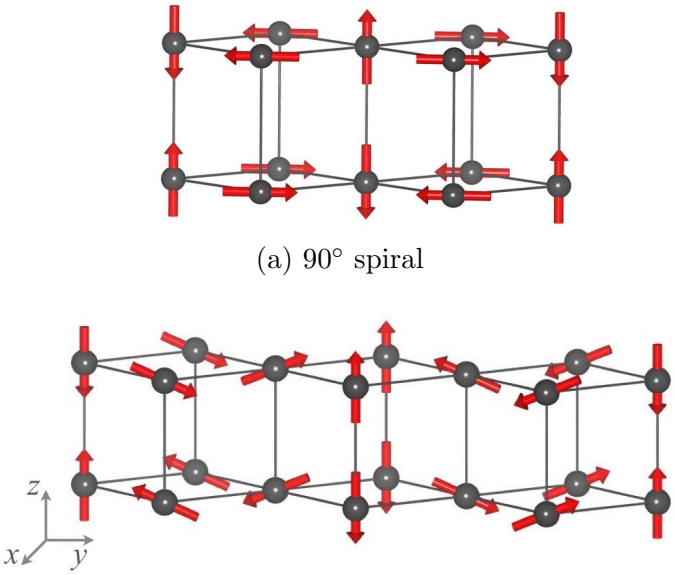

(a) 90° spiral

(b) 60° spiral

Figure 1.10: Non-collinear spin spiral orders

two typical representatives, 90° and 60° cycloidal spiral. They are with propagation wave vector $q = 1/2$ and $q = 1/3$ along y-axis. Thus we need a supercell of two and three $Pbnm$ unit cells respectively. We can reasonably use these two common models to simulate the actual ground state in the experiments.

1.2.3.2 E-type collinear AFM order

The rare-earth manganites of our interest display another important realization of magnetically induced ferroelectricity. In this case, the spins arrange according to a particular collinear ordering, which is denoted as E-AFM order. In Figure 1.11, we plot two types of E-AFM order. The propagation wave vector associated to this order is $q = 1/2$, and consequently we need to consider two $Pbnm$ unit cells to reproduce its pattern (for example $a \times 2b \times c$). E-AFM order is a specific magnetic state with up-up-down-down in-plane spin ordering and anti-parallel inter-plane alignment. Correspondingly, the two E-type order can be described by means of the order parameters:

$$\mathbf{E_1} = \mathbf{S_1} + \mathbf{S_2} - \mathbf{S_3} - \mathbf{S_4} - \mathbf{S_5} - \mathbf{S_6} + \mathbf{S_7} + \mathbf{S_8}, \tag{1.53}$$

$$\mathbf{E_2} = \mathbf{S_1} - \mathbf{S_2} - \mathbf{S_3} + \mathbf{S_4} - \mathbf{S_5} + \mathbf{S_6} + \mathbf{S_7} - \mathbf{S_8}, \tag{1.54}$$

where $\mathbf{S}_i$ refers to ith magnetic atom in unit cell.

The magnetic atoms are numbered according to Fig. 1.11(a), the same number corresponds to the identical atom. The switch from E_1 to E_2-type, is turning the in-plane

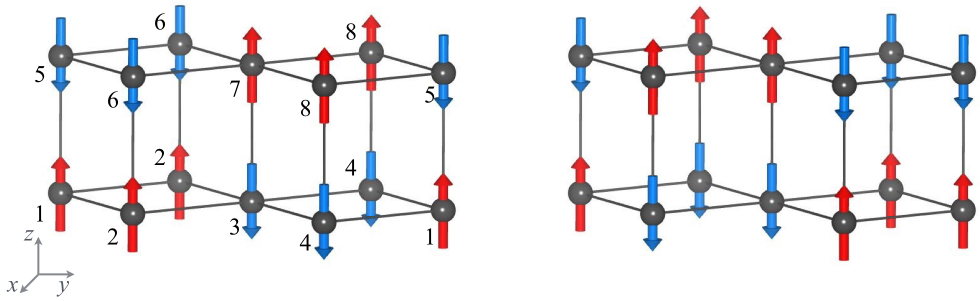

(a) E_1-AFM (b) E_2-AFM

Figure 1.11: Unit cell of two kinds E-AFM order in *Pbnm* space group.

magnetic series from up-up-down-down series to up-down-down-up. In the experimental phase diagram Fig. 1.7, several compounds with relative small R ion are stabilized as E-AFM state at low temperature.

Since E-AFM state is a collinear ordering, we consider $\mathbf{E_1}$ and $\mathbf{E_2}$ as scalars E_1 and E_2. The pure magnetic free energy of the system has the following form:

$$F_m = \frac{1}{2}A(E_1^2 + E_2^2) + \frac{1}{4}B_1(E_1^4 + E_2^4) + \frac{1}{2}B_2E_1^2E_2^2. \tag{1.55}$$

Minimizing this energy we obtain two possible sets of solutions. If $B_2 < 0$ (but still $|B_2| < B_1$), $(E_1, E_2) = (\pm E, \pm E)$ with

$$E = \begin{cases} 0 & (T \geq T_N) \\ \sqrt{\frac{A}{B_1+B_2}} & (T \leq T_N). \end{cases} \tag{1.56}$$

However, if $B_2 > 0$, we then have $(E_1, E_2) = (\pm E, 0)$ and $(E_1, E_2) = (0, \pm E)$ where

$$E = \begin{cases} 0 & (T \geq T_N) \\ \sqrt{\frac{A}{B_1}} & (T \leq T_N) \end{cases}. \tag{1.57}$$

Emergence of the electric polarization The couplings to the electric polarization can be obtained from the general symmetry analysis. The generators of the *Pbnm* space group in the irreducible representation can be obtained from GENPOS on Bilbao Crystallographic Server [28], which gives three generators – two-fold operator $\{2_a|\frac{1}{2}\frac{1}{2}0\}$, $\{2_c|00\frac{1}{2}\}$ and inversion operator $\{-1|0\}$. Under these operations, the symmetric coordinates can be transformed according to table 1.1.

The Landau free energy of the system should be invariant under the operation of the generators. According to the transformation table 1.1, it allows us to obtain the form of

	$\{2_a\|\frac{1}{2}\frac{1}{2}0\}$	$\{2_c\|00\frac{1}{2}\}$	$\{-1\|0\}$
E_1	$-E_1$	$-E_2$	E_2
E_2	E_2	$-E_1$	E_1
P_a	P_a	$-P_a$	$-P_a$
P_b	$-P_b$	$-P_b$	$-P_b$
P_c	$-P_c$	P_c	$-P_c$

Table 1.1: Table of transformation of the symmetric coordinates under the generators of space group *Pbnm*

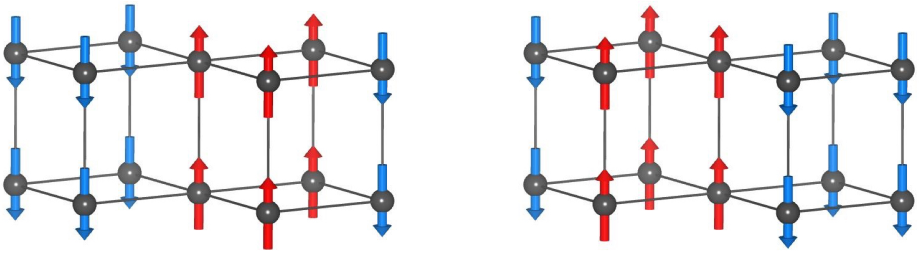

(a) E_1^*-AFM (b) E_2^*-AFM

Figure 1.12: Two E*-type collinear spin orders

the coupling term as follow

$$F_{em} = -\lambda_1 P_a(E_1^2 - E_2^2) - \lambda_2 P_b(E_1^2 - E_2^2)E_1E_2. \tag{1.58}$$

We have two coupling terms between the polarization and the magnetic order parameters, both of them persist the symmetric invariant. Minimizing the free energy with respect to the polarizations P_a and P_b, we obtain

$$P_a = \frac{\lambda_1}{a}(E_1^2 - E_2^2) \tag{1.59}$$

$$P_b = \frac{\lambda_2}{a}(E_1^2 - E_2^2)E_1E_2 \tag{1.60}$$

$$P_c = 0. \tag{1.61}$$

We will have four types of domains inducing polarizations: $(\pm E_1, 0) \rightarrow (P_a, 0)$, $(0, \pm E_2) \rightarrow (-P_a, 0)$, $(\pm E, \pm E) \rightarrow (0, 0)$ and $(\pm E_1, \pm E_2) \rightarrow (P_a, P_b)$. E_1 and E_2 are leading to polarizations oriented along $+a$ and $-a$ directions. The coexistence of E_1 and E_2 ($E_1 \neq E_2$) may induce polarization in the ab-plane which is the vector sum of P_a and P_b.

There are another kinds of E-AFM orders, we denote them as E*-AFM orders, which with up-up-down-down (or up-down-down-up) in-plane spin ordering, but parallel align-

ment inter-plane. There are also two order parameters of E*-AFM structure:

$$\mathbf{E_1^*} = \mathbf{S_1} + \mathbf{S_2} - \mathbf{S_3} - \mathbf{S_4} + \mathbf{S_5} + \mathbf{S_6} - \mathbf{S_7} - \mathbf{S_8} \tag{1.62}$$

$$\mathbf{E_2^*} = \mathbf{S_1} - \mathbf{S_2} - \mathbf{S_3} + \mathbf{S_4} + \mathbf{S_5} - \mathbf{S_6} - \mathbf{S_7} + \mathbf{S_8} \tag{1.63}$$

corresponding to Fig. 1.12(a) and (b). After employing normal collinear orders (A,C,G,F), the crystal structure keeps its $Pbnm$ space group, whereas by imposing E-type orders, the structure decomposes into $P2_1nm$, which is a maximal non-isomorphic subgroup of $Pbnm$.

1.3 Microscopic model

In this section we discuss a general microscopic model that enables the unified description of all the aforementioned spin orders. The parameters of this model can be determined from DFT calculations.

1.3.1 General model

For a magnetic system, we can write a general Hamiltonian:

$$H = -\sum_{i,j}\sum_{\alpha,\beta} J_{ij}^{\alpha\beta} S_i^{\alpha} S_j^{\beta}. \tag{1.64}$$

Here, i and j indicate the positions of the spins in the crystal lattice, while α and β refer to spin components. We can further write the formula into a matrix form:

$$H = -\sum_{i,j} (S_i^1, S_i^2, S_i^3) \begin{pmatrix} J_{ij}^{11} & J_{ij}^{12} & J_{ij}^{13} \\ J_{ij}^{21} & J_{ij}^{22} & J_{ij}^{23} \\ J_{ij}^{31} & J_{ij}^{32} & J_{ij}^{33} \end{pmatrix} \begin{pmatrix} S_j^1 \\ S_j^2 \\ S_j^3 \end{pmatrix}. \tag{1.65}$$

the trace of the symmetric part corresponds to the isotropic exchange interaction:

$$J_{ij} = \frac{1}{3}\sum_{\alpha} J_{ij}^{\alpha\alpha}. \tag{1.66}$$

The off-diagonal part is related to the Dzyaloshinskii-Moriya (DM) interactions:

$$D_{ij}^{\gamma}\epsilon^{\gamma\alpha\beta} = \frac{1}{2}(J_{ij}^{\alpha\beta} - J_{ij}^{\beta\alpha}). \tag{1.67}$$

The off-diagonal terms of the specific self-interaction case $i = j$, give rise to the single-ion anisotropic interaction. In the following, we are going to provide detailed discussions of these three interactions.

1.3.2 Exchange interaction

We employ a classical Heisenberg model [29] to describe the microscopic interaction between magnetic atoms, in which the spins of the magnetic atoms are treated as classical vectors. The Heisenberg Hamiltonian describes the exchange interaction between two different individual spins $\mathbf{S_1}$ and $\mathbf{S_2}$, and can be written as:

$$H = -J_{12}\mathbf{S_1} \cdot \mathbf{S_2}, \tag{1.68}$$

where J is the exchange interaction parameter determined by the overlap of the electron wave functions subjected to Pauli' s exclusion principle. When $J > 0$, the exchange interaction favors the parallel orientation of spins which is the ferromagnetic (FM) order, otherwise, for $J < 0$ the interaction favors the antiparallel spin alignment, forming antiferromagnetic (AFM) order. In a crystal lattice structure, the exchange interaction term in a general Hamiltonian involves the sum over all spin pairs:

$$H_{EX} = -\sum_{i,j} J_{ij}\mathbf{S}_i \cdot \mathbf{S}_j \tag{1.69}$$

i and j represent different coordinates of the lattice. Since there is almost no overlap of electron for distant pairs, compared to the near neighboring pairs, the interaction between distant pairs can be neglected.

Taking the xy-plane spiral as an example, for the most simple model of the interaction, we consider a FM nearest-neighbor (NN) and AFM next-nearest-neighbor (NNN) interactions in the xy plane (which is the easy plane), inter-plane interaction along z is excluded. The Hamiltonian can be reduced to

$$H = -J_1 \sum_i \mathbf{S}_i \cdot (\mathbf{S}_{i+x} + \mathbf{S}_{i-x} + \mathbf{S}_{i+y} + \mathbf{S}_{i-y}) + J_2 \sum_i \mathbf{S}_i \cdot (\mathbf{S}_{i+x+y} + \mathbf{S}_{i-x-y} + \mathbf{S}_{i-x+y} + \mathbf{S}_{i+x-y}). \tag{1.70}$$

The AFM NNN interaction tends to destabilize the FM NN interaction, forming the spin spiral state. The spin can be parametrized as

$$\mathbf{S}_i = S\cos(\mathbf{Q} \cdot \mathbf{r}_i)\hat{\mathbf{x}} + S\sin(\mathbf{Q} \cdot \mathbf{r}_i)\hat{\mathbf{y}}, \tag{1.71}$$

in which the wave vector $\mathbf{Q} = \frac{Q}{\sqrt{2}}(1, 1, 0)$. By directly substituting it into the hamiltonian (equation (1.70)) and minimizing the total energy with respect to Q, we got the energy minimum of the spiral $E_S = J_1^2 S^2/J_2$ when $\cos(Q/\sqrt{2}) = J_1/(2J_2)$. Comparing E_S with the energy of FM state $E_{FM} = 4J_1(1 - J_2/J_1)S^2$, we can determine that the spiral state is stable when $J_2 > J_1/2$. This means that when the NNN interaction J_2 exceeds half of the NN interaction $J_1/2$, the system is inclined to stabilize as spiral state. We can use this

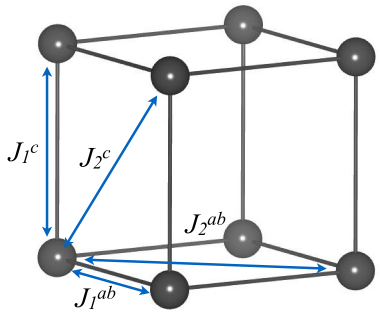

Figure 1.13: Schematic diagram of exchange interactions in *Pbnm* lattice, for simplicity, only magnetic atoms (B-site) are shown. J_{ab} and J_c are the in-plane and out-of-plane nearest interactions, while J_a is the in-plane next-nearest interaction.

simple model to explain the stabilization the spin spiral state in the orthorhombic manganites $R\mathrm{MnO_3}$, which is due to the competition between isotropic exchange interactions. And such isotropic exchange interactions are strongly affected by the size of A-site ion. The plane of the spiral is determined by a subtle competition between SIA and DM interaction, which are strongly dependent on specific compound and its condition. Therefore this competition can be controlled by external stimuli such as magnetic field, pressure or epitaxial strain.

We take the orthorhombic *Pbnm* perovskite structure as a typical example. In Figure 1.13, we include both the NN and NNN interactions, in which in-plane and out-of-plane are distinguished with each other. Therefore we obtain the exchange interaction part of the hamiltonian

$$H_{EX} = J_1^{ab} \sum_{\langle i,j \rangle}^{ab} \mathbf{S}_i \cdot \mathbf{S}_j + J_1^c \sum_{\langle i,j \rangle}^{c} \mathbf{S}_i \cdot \mathbf{S}_j + J_2^{ab} \sum_{\langle\langle i,j \rangle\rangle}^{ab} \mathbf{S}_i \cdot \mathbf{S}_j + J_2^c \sum_{\langle\langle i,j \rangle\rangle}^{c} \mathbf{S}_i \cdot \mathbf{S}_j \tag{1.72}$$

where J_1^{ab} and J_1^c are the in-plane and out-of-plane NN interactions, J_2^{ab} and J_2^c are the in-plane NNN interactions. In a sense, the exchange interaction has already been considered as anisotropic at this level. Nevertheless, it remains isotropic that it only depends on the relative orientation of the spins. For a *Pbnm* structure, each magnetic atom is surrounded by 4 in-plane NN atoms, 2 out-of-plane NN atoms, 4 in-plane NNN atoms and 8 out-of-plane NNN atoms.

1.3.3 Single-ion anisotropy

Magnetic anisotropy is the dependence of magnetic properties on a preferred direction. Inside a crystal, the orbital state of a magnetic ion is obviously affected by the crystal field produced by its surrounding charges. This effect will act on its spin via spin-orbit

coupling, leading to a dependence of the magnetic energy on the spin orientation relative to the crystalline axes. Such a dependence is the so-called single-ion anisotropy (SIA). The SIA drives the separation of easy and hard axes. In a cubic perovskite structure, the SIA contribution to the Hamiltonian can be expressed as

$$H_{SIA} = K \sum_i (S_{i,x}^2 S_{i,y}^2 + S_{i,y}^2 S_{i,z}^2 + S_{i,z}^2 S_{i,x}^2) \tag{1.73}$$

Thus, when $K > 0$, the easy-axes are along the [100], [010] and [001] directions, whereas $K < 0$, they are along the [111] directions. If the local environments become uniaxial, the single-ion anisotropy can be written as

$$H_{SIA} = -\sum_i [K_i S_{i,z}^2 + K_i'(S_{i,x}^2 - S_{i,y}^2)] \tag{1.74}$$

in such expression, the anisotropy is determined by two parameters, K_i and K_i'. If $K_i > 0$ the anisotropy is of the easy axis type while if $K_i < 0$ it is of the easy plane type. The other parameter K_i' determines the direction of the spin in the xy-plane.

1.3.4 Dzyaloshinskii-Moriya interaction

The Dzyaloshinskii-Moriya (DM) interaction [30, 31, 32], or antisymmetric anisotropic exchange, arises from the interplay between broken inversion symmetry and spin-orbit coupling. For a simple two magnetic atoms model [see Figure 1.16], its hamiltonian is written as

$$H_{DM} = -\mathbf{D}_{12} \cdot (\mathbf{S}_1 \times \mathbf{S}_2), \tag{1.75}$$

where $\mathbf{D}_{12}$ is the DM vector for magnetic atom 1 and 2, which contains at most three independent parameters, is constrained by symmetry. Normally, the DM interaction favors the perpendicular alignment of spins with respect to their original orientation. It competes with the isotropic exchange interaction preferring the (anti-)parallel alignment of nearest-neighboring spins. Thus the DM interaction represents an important source of magnetic frustration. In fact, two spins interacting via equations (1.68) and (1.75) will tend to be perpendicular to the DM vector with a the relative angle $\theta_{12} = \arctan(D_{12}/J_{12})$ modulo a π angle (such that, in the limit $D_{12} \to 0$, $\theta_{12} \approx 0$ if $J_{12} > 0$ while $\theta_{12} \approx \pi$ if $J_{12} < 0$). This basically explains many of the non-collinear magnetic orderings, *e.g.* spin spiral, spin canting and weak FM.

In a *Pbnm* perovskite crystal structure, the overall hamiltonian has a more complex

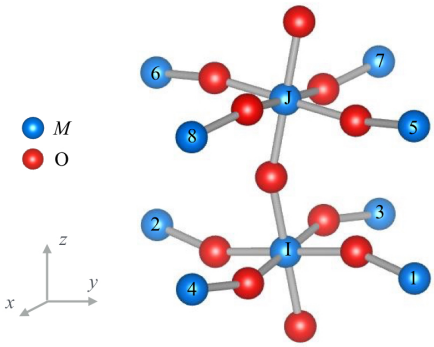

Figure 1.14: Schematic plot of perovskite *Pbnm* structure for the description of the Dzyaloshinsky-Moriya interactions associated with different Mn-O-Mn bonds, Mn is in blue and O is in red, the A-site ions are neglected for simplicity.

expression, which includes all neighboring spin pairs.

$$H_{DM} = -\sum_{<i,j>} \mathbf{D}_{ij} \cdot \mathbf{S}_i \times \mathbf{S}_j, \tag{1.76}$$

in which $\mathbf{D}_{ij}$ is the DM vector for magnetic atom i and j. They follow the antisymmetric relation: $\mathbf{D}_{ij} = -\mathbf{D}_{ij}$. In the perovskites, *e.g.* manganites, the exchange interactions are mediated by the oxygen atoms, the DM vector is defined on the Mn_i-O-Mn_j bond. Each $\mathbf{D}_{ij}$ can be expressed in terms of five parameters $\alpha_{ab}, \beta_{ab}, \gamma_{ab}, \alpha_c, \beta_c$

$$\mathbf{D}_{i,\ i+x} = \begin{bmatrix} -(-1)^{i_x+i_y+i_z}\alpha_{ab} \\ (-1)^{i_x+i_y+i_z}\beta_{ab} \\ (-1)^{i_x+i_y}\gamma_{ab} \end{bmatrix}, \tag{1.77}$$

$$\mathbf{D}_{i,\ i+y} = \begin{bmatrix} (-1)^{i_x+i_y+i_z}\alpha_{ab} \\ (-1)^{i_x+i_y+i_z}\beta_{ab} \\ (-1)^{i_x+i_y}\gamma_{ab} \end{bmatrix}, \tag{1.78}$$

$$\mathbf{D}_{i,\ i+z} = \begin{bmatrix} (-1)^{i_z}\alpha_c \\ (-1)^{i_x+i_y+i_z}\beta_c \\ 0 \end{bmatrix}. \tag{1.79}$$

We show an example in Figure 1.14, where the Mn atoms are labelled accordingly. Associated with different Mn-O-Mn bonds in perovskite structure, the corresponding DM vectors are $D_{I1} = D_{I2} = (-\alpha_{ab}, \beta_{ab}, \gamma_{ab})$, $D_{I3} = D_{I4} = (\alpha_{ab}, \beta_{ab}, \gamma_{ab})$, $D_{J5} = D_{J6} = (\alpha_{ab}, -\beta_{ab}, \gamma_{ab})$, $D_{J7} = D_{J8} = (-\alpha_{ab}, -\beta_{ab}, \gamma_{ab})$, $D_{IJ} = (\alpha_c, \beta_c, 0)$.

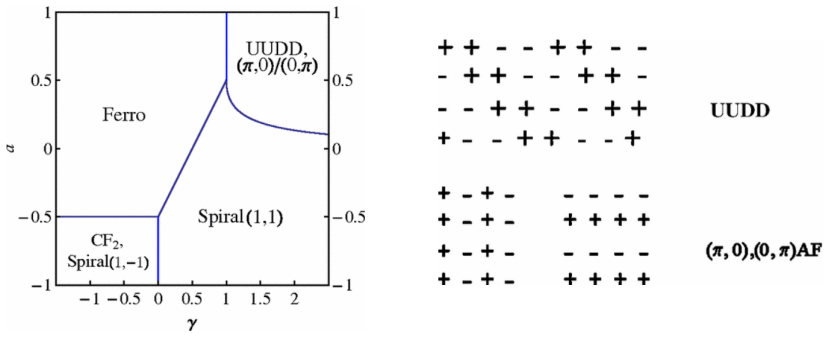

(a) (b)

Figure 1.15: (a) Phase diagram and (b) the corresponding ground states UUDD and (π, 0) (0, π)

1.3.5 Biquadratic interaction

The biquadratic interaction

$$H_{BI} = -\sum_{<i,j>} B_{ij}(\mathbf{S}_i \cdot \mathbf{S}_j)^2, \tag{1.80}$$

is isotropic. This interaction results from fourth-order perturbation theory within the Hubbard model in the limit $t/U \ll 1$. Such high-order exchange interaction [see Equation (1.80)] can be incorporated into the frustrated Heisenberg model, in order to search for the origin of collinear E-type (up-up-down-down) order. Such interaction is originating from the spin-phonon coupling, which is derived by integrating out the phonon degrees of freedom. The stabilization of E-type state is cooperatively determined by the frustrated exchange interaction and its competition with biquadratic coupling

In Fig. 1.15, we show the the phase diagram in terms of the parameter a and γ [33], where $a = B/|J_1|$ and $\gamma = J_2/|J_1|$, the parameters B, J_1 and J_2 have been defined as above. The physical meaning of a and γ correspond to the biquadratic interaction and frustrated effect respectively. The schematic diagram of ground state up-up-down-down, (π, 0) and (0, π) are plotted in Figure 1.15(b). As we can see, the alone frustrated effect is not able to stabilize E-type order, no matter how large it is. Only when a strong biquadratic interaction is involved, the uudd E-type ground state can be obtained.

An effective way to enhance this interaction is by applying external pressure. A pressure-induced transition from the bc cycloidal spiral state to the E-AFM state has been observed at around $4 \sim 5$ GPa, accompanied with the spontaneous polarization flopping from c to a axis and its amplitude increases about ten times with respect to the magnitude [22].

Another approach to tune multiferroicity is the application of epitaxial strain [23, 34]. Neutron diffraction and electric measurement reveal that in highly strained (010) oriented thin film on $YAlO_3$ substrate, the magnetic order in $TbMnO_3$ stabilized into a commensurate E-AFM order along with an enormous increase of the polarization compare to that of bulk materials [23].

1.3.6 Spin-orbit coupling

In the above sections, we have clarify the microscopic origin of the emergence of spin spirals and E-AFM orders. In this section, we describe two microscopic mechanisms on the spin spirals induced ferroelectricity in perovskites.

One the one hand, the electric polarization can emerge due to the dependence of the symmetric exchange interactions on the atomic displacements (*i.e.* symmetric magnetostriction). That is, due to the dependence of the wavefunction overlaps on the specific positions of the atoms. In perovskites, these interactions are mediated by the oxygen atoms (superexchange) and hence $J(r_i, r_j; r^o_{ij})$, where $r_{i(j)}$ represents the position of the magnetic atoms and r^o_{ij} corresponds to that of the oxygen. These positions can be expressed as $\mathbf{r} = \mathbf{r}^{(0)} + \delta\mathbf{r}$, where $\delta\mathbf{r}$ accounts for the corresponding displacement. Thus, the aforementioned dependence can formally be written as

$$J(r_i, r_j; r^o_{ij}) = J_{ij} + \mathbf{J}^{(i)}_{ij} \cdot \delta\mathbf{r}_i + \mathbf{J}^{(j)}_{ij} \cdot \delta\mathbf{r}_j + \mathbf{J}^{o}_{ij} \cdot \delta\mathbf{r}^o_{ij} + \dots \tag{1.81}$$

where $J_{ij} = J(\mathbf{r}^{(0)}_i, \mathbf{r}^{(0)}_j; \mathbf{r}^{o(0)}_{ij})$ and the form of vector $\mathbf{J}^{\alpha}_{ij}$ can be deduced from symmetry considerations. If one considers the displacements associated to the electric polarization: $\mathbf{J}^{(i)}_{ij} \cdot \delta\mathbf{r}_i + \mathbf{J}^{(j)}_{ij} \cdot \delta\mathbf{r}_j + \mathbf{J}^{o}_{ij} \cdot \delta\mathbf{r}^o_{ij} = \mathbf{J'}_{ij} \cdot \mathbf{P}$. Then, whenever $\mathbf{J'}_{ij} \neq 0$, the spin order can induce this polarization because the minimization of the total energy implies:

$$\mathbf{P} \propto \sum_{ij} \mathbf{J'}_{ij} (\mathbf{S}_i \cdot \mathbf{S}_j) \tag{1.82}$$

This mechanism is rather general, and in fact can be triggered by purely electronic effects. In the case of the orthorhombic $R\mathrm{MnO_3}$ manganites, the ferroelectricity induced by the particular collinear E-AFM order is due to this mechanism. The parameter $\mathbf{J'}_{ij}$ is determined by the symmetry of the system. It also works when the system has two species of spins, which is the case of perovskites like $GdFeO_3$ or $DyFeO_3$. However, this mechanism is ineffective if the spiral is in the *bc* plane.

On the other hand, the same reasonings can be applied to DM interaction. In general, this interaction also depends on the atomic displacements (*i.e.* antisymmetric magne-

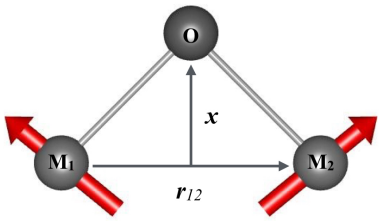

Figure 1.16: Schematic plot of a M-O-M bonding example for description of Dzyaloshinsky-Moriya interactions, M represents a magnetic ion and O is an oxygen ion.

tostriction):

$$\mathbf{D}(\mathbf{r}_i, \mathbf{r}_j) = \mathbf{D}_{ij} + \mathbf{D}_{ij}^{(i)} \cdot \delta\mathbf{r}_i + \mathbf{D}_{ij}^{(j)} \cdot \delta\mathbf{r}_j + \mathbf{D}_{ij}^{o} \cdot \delta\mathbf{r}_{ij}^{o} + \ldots \tag{1.83}$$

and therefore can produce an electric polarization:

$$\mathbf{P} \propto \sum_{ij} D'_{ij}(\mathbf{S}_i \times \mathbf{S}_j) \tag{1.84}$$

whenever these changes are associated to polar displacements. This is the so-called inverse DM mechanism [35].

Specifically, the exchange between spins of magnetic ions is usually mediated by an oxygen ion, forming M-O-M bonds, see Figure 1.16. In the first-order approximation, the magnitude of the DM vector $\mathbf{D}_{12}$ is proportional to the displacement of oxygen ion ($\mathbf{x}$) away from the "original" middle point

$$\mathbf{D}_{12} \propto \mathbf{x} \times \hat{\mathbf{r}}_{12}, \tag{1.85}$$

where $\hat{\mathbf{r}}_{12}$ is a unit vector along the line connecting the magnetic ions 1 and 2, and $\mathbf{x}$ is the shift of the oxygen ion from this line, indicating in Fig. 1.16. Thus, the energy of the DM interaction decreases with $\mathbf{x}$, describing the degree of inversion symmetry breaking at the oxygen site. Minimize the total energy with respect to the oxygen displacement $\mathbf{x}$, we got:

$$\mathbf{x} \propto \hat{\mathbf{r}}_{12} \times (\mathbf{S}_1 \times \mathbf{S}_2). \tag{1.86}$$

In the spiral state, the vector product has the same sign for all pairs of neighboring spins, the negative oxygen ions are pushed to the same direction, which is perpendicular to the spin chain formed by positive magnetic ions, giving arise to a macroscopic ferroelectric polarization.

It also has a purely electronic version, in which the electric polarization can be associated to the spin current generated by the vector chirality $\mathbf{S}_i \times \mathbf{S}_j$ of non-collinear spins. In this case, it is called the spin-current mechanism [36]. More phenomenologically, this type of polarization can be seen as due to coupling terms of the type $\mathbf{P} \cdot [(\mathbf{M} \cdot \nabla)\mathbf{M} - \mathbf{M}(\nabla \cdot \mathbf{M})]$ in expression (1.50) which, in contrast to the symmetric magnetostriction, is always allowed by symmetry. The specific form of these couplings, however, depends on the specific symmetry of the system.

In the particular case of the orthorhombic $R\mathrm{MnO_3}$ manganites the antisymmetric magnetostriction yields $\mathbf{P} \propto \sum_{ij} \hat{\mathbf{r}}_{ij} \times (\mathbf{S}_i \times \mathbf{S}_j)$, as we have defined above, $\hat{\mathbf{r}}_{ij}$ is the unit vector connecting the corresponding spins. Specifically, for the bc cycloidal spiral (the ground state of $\mathrm{TbMnO_3}$), $\mathbf{r}_{ij}$ is along b direction and $\mathbf{S}_i \times \mathbf{S}_j$ is along a-axis, therefore the oxygen is pushed along the c-axis, thus induce polarization along c direction.

1.4 Conclusions

In conclusion, we have given a brief introduction on the (multi-)ferroics based on the phenomenological theory and the microscopic models. We started with the Landau description of three types of ferroelectrics – the proper, improper and pseudo-proper ferroelectrics. These provided the fundamentals for the phenomenological study on confined geometrics in Chapter 3. And then we reviewed various magnetic orders in rare-earth manganites, especially inversion-symmetry breaking orders – the spin spirals and the E-AFM orders – that give rise to the multiferroicity. We discussed the emergence of these orders and the mechanism of magnetically-induced ferroelectricity in these materials. Finally, we illustrate the general microscopic model that enables the unified description of all these magnetic orders. These discussions serve as the background of our DFT study on the magnetic phase instability of $\mathrm{EuMnO_3}$ and $\mathrm{TbMnO_3}$ in Chapter 4 and 5.

2

First principles calculations

"The underlying physical laws necessary for the mathematical theory of a large part of physics and the whole of chemistry are thus completely known, and the difficulty is only that the exact application of these laws leads to equations much too complicated to be soluble. It therefore becomes desirable that approximate practical methods of applying quantum mechanics should be developed, which can lead to an explanation of the main features of complex atomic systems without too much computation."[37]

– Paul Dirac

2.1 Introduction

In 1929, just three years after the Schrödinger derived his famous equation [38], Paul Dirac made the above prospective opinions, emphasizing on the difficulty of solving the equations of quantum mechanics and desirability of developing practical methods of applying quantum mechanics to explain complex systems. During the same period, Thomas [39] and Fermi [40] proposed a scheme based on the density of the electrons in the system $n(r)$, it stands separate from the wave function theory as being formulated in terms of the electronic density alone. This Thomas-Fermi model is viewed as a precursor to modern density functional theory (DFT). In the following several decades, physicists made great efforts on solving Schrödinger-type equations with local effective potentials and improving numerical methods [41, 42, 43, 44, 45], which have been decisive in carrying out density functional calculations. Until 1965, Kohn and Sham introduced the famous Kohn-Sham equation, suggesting an alternative way to implement the DFT [46]. Within the framework of Kohn-Sham DFT, the complex many-body problem of interacting electrons is reduced to a tractable problem of non-interacting electrons moving in an effective potential. DFT is that powerful "approximate practical methods, which can lead to an explanation of the main features of complex atomic systems without too much computation".

In the first three sections of this chapter we describe the precursor methods before DFT, including Born-Oppenheimer approximation, Hartree-Fock and Thomas-Fermi approach. In the next two sections, we introduce the fundamentals of DFT and the related exchange-correlation approximations. Finally, we show the details of the practical numerical implementation as it is used in this thesis: basis sets, k-point mesh and pseudopotentials.

2.2 The many-body Schrödinger Equation

In the time-independent many-body quantum theory, a system of interacting particles is described by the following many-body Schrödinger equation:

$$H\Psi = E\Psi, \tag{2.1}$$

where H is the Hamiltonian of the system, Ψ is the wave function for all the particles and E is the corresponding energy. For a solid state system, the hamiltonian is decomposed into the kinetic energy and potential of electrons and nuclei plus the interactions between them, which can be written as:

$$\begin{aligned} H(\mathbf{R},\mathbf{r}) &= T_e(\mathbf{r}) + V_{ee}(\mathbf{r}) + V_{en}(\mathbf{R},\mathbf{r}) + T_n(\mathbf{R}) + V_{nn}(\mathbf{R}) \\ &= -\frac{\hbar^2}{2m_e}\sum_i \nabla_i^2 + \frac{1}{2}\sum_{i\neq j}\frac{e^2}{|\mathbf{r}_i-\mathbf{r}_j|} + \sum_{i,I}\frac{Z_I e^2}{|\mathbf{r}_i-\mathbf{R}_I|} \\ &\quad -\sum_I \frac{\hbar^2}{2m_I}\nabla_I^2 + \frac{1}{2}\sum_{I\neq J}\frac{Z_I Z_J e^2}{|\mathbf{R}_I-\mathbf{R}_J|}, \end{aligned} \tag{2.2}$$

where the subscript e and n indicate the electron and nucleus, m_e and m_I are the mass of electron and nucleus. Different electrons and nuclei are denoted by lower case i, j and upper case subscripts I, J respectively. Z_I is the charge of nuclei. Since the difference of the mass of electrons and nuclei is huge, we can assume that the motion of electrons and nuclei are separated. The electrons follow the nuclear motion adiabatically, thus to rearrange instantaneously to the ground state for the given atomic coordinates. The total wave function can be written into the multiplication of electronic and nuclear parts, this is called Born-Oppenheimer approximation [47]. Due to the large nuclei mass, kinetic energy of the nuclei can be treated as a perturbation on the electronic hamiltonian,

$$\begin{aligned} H(\mathbf{R},\mathbf{r}) &= T_e(\mathbf{r}) + V_{int}(\mathbf{r}) + V_{ext}(\mathbf{R},\mathbf{r}) + V_{nn}(\mathbf{R}) \\ &= -\frac{1}{2}\sum_i \nabla_i^2 + \frac{1}{2}\sum_{i\neq j}\frac{e^2}{|\mathbf{r}_i-\mathbf{r}_j|} + \sum_{i,I} V_I(|\mathbf{r}_i-\mathbf{R}_I|) + V_{nn}. \end{aligned} \tag{2.3}$$

Here we adopt Hartree atomic units $\hbar = m_e = e = 4\pi\epsilon_0 = 1$. In this expression, the electronic hamiltonian includes four distinct operators: the kinetic energy of the electrons T_e, electronic interactions V_{int}, the fixed external nuclear potential acting on the electrons V_{ext} and the classical nuclear interaction V_{nn}, which can be trivially obtained. This hamiltonian is central to the theory of electronic structure.

2.3 Hartree-Fock approximation

When we discuss the electronic properties in a solid state, it is natural to consider the many-electron wave function, $\Psi(\mathbf{r})$, where $\mathbf{r}$ denotes the particle coordinates. One of the earliest and most widely used of all approximations is the Hartree-like approximation [48, 49], which treats the many-electron wave function as a product of single-particle functions, *i.e*

$$\Psi(\mathbf{r}_1, \mathbf{r}_2, ..., \mathbf{r}_N) = \psi_1(\mathbf{r}_1)...\psi_N(\mathbf{r}_N). \tag{2.4}$$

Each of the functions satisfies a one-electron Schrödinger equation

$$[-\frac{1}{2}\nabla^2 + V_{ext} + V_i]\psi_i(\mathbf{r}) = \varepsilon_i\psi_i(\mathbf{r}), \tag{2.5}$$

with a potential term arising from the average field of the other electrons, *i.e*. the Coulomb potential V_i which is given by

$$V_i = \sum_{j(\neq i)}^{N} \int d\mathbf{r}' \frac{1}{|\mathbf{r} - \mathbf{r}'|}\psi_j^*(\mathbf{r}')\psi_j(\mathbf{r}') \tag{2.6}$$

and an external potential due to the nuclei V_{ext}. Fermi statistics can be incorporated into this picture by replacing the product wave function by a properly determinant function for a fixed number N of electrons. Due to the Pauli exclusion principle, the total wavefunction for the system must be antisymmetric under particle exchange:

$$\Psi(\mathbf{r}_1, \mathbf{r}_2, ..., \mathbf{r}_i, ..., \mathbf{r}_j, ..., \mathbf{r}_N) = -\Psi(\mathbf{r}_1, \mathbf{r}_2, ..., \mathbf{r}_j, ..., \mathbf{r}_i, ..., \mathbf{r}_N), \tag{2.7}$$

where $\mathbf{r}_i$ includes coordinates of position. A Slater determinant wavefunction [50] which satisfies antisymmetry is used instead of the simple product form,

$$D = \begin{vmatrix} \psi_1^\sigma(\mathbf{r}_1) & \psi_1^\sigma(\mathbf{r}_2) & ... & \psi_1^\sigma(\mathbf{r}_N) \\ \psi_2^\sigma(\mathbf{r}_1) & \psi_2^\sigma(\mathbf{r}_2) & ... & \psi_2^\sigma(\mathbf{r}_N) \\ ... & ... & ... & .... \\ \psi_N^\sigma(\mathbf{r}_1) & \psi_N^\sigma(\mathbf{r}_2) & ... & \psi_N^\sigma(\mathbf{r}_N) \end{vmatrix}, \tag{2.8}$$

where σ indicates the spin. We can rewrite the Schrödinger equation into the Hartree-Fock form [51]:

$$[\frac{1}{2}\nabla^2 + V_{ext}(\mathbf{r}) + V_{Hartree}(\mathbf{r}) + V_x^i(\mathbf{r})]\psi_i^\sigma(\mathbf{r}) = \varepsilon_i\psi_i^\sigma(\mathbf{r}) \tag{2.9}$$

with

$$V_{Hartree}(\mathbf{r}) = \sum_j \int d\mathbf{r}' \frac{1}{|\mathbf{r}-\mathbf{r}'|}\psi_j^{\sigma*}(\mathbf{r}')\psi_j^\sigma(\mathbf{r}'), \tag{2.10}$$

$$V_x^i(\mathbf{r}) = -\sum_j \int d\mathbf{r}' \frac{1}{|\mathbf{r}-\mathbf{r}'|}\psi_j^{\sigma*}(\mathbf{r}')\psi_i^\sigma(\mathbf{r})\frac{\psi_j^\sigma(\mathbf{r})}{\psi_i^\sigma(\mathbf{r})}. \tag{2.11}$$

$V_{Hartree}(\mathbf{r})$ being the classical Coulomb potential (Hartree potential). Additionally, the Hartree-Fock approximation leads to nonlocal exchange term V_x, which makes the Hartree-Fock equations difficult to solve.

2.4 Thomas-Fermi approach

Thomas [39] and Fermi [40, 52] are taking a different approach, which is a scheme based on the electronic density of the system, $n(\mathbf{r})$:

$$n(\mathbf{r}) = N\int d\mathbf{r}_2 ... \int d\mathbf{r}_N \Psi(\mathbf{r}, \mathbf{r}_2, ..., \mathbf{r}_N)\Psi^*(\mathbf{r}, \mathbf{r}_2, ..., \mathbf{r}_N). \tag{2.12}$$

The Thomas-Fermi method assumed that the motions of the electrons are uncorrelated, the electron-electron interaction energy only comes from the electrostatic energy and that the corresponding kinetic energy can be written into an explicit functional of the density, describing the free electrons in a homogeneous gas with density equal to the local density at any given point.

$$E_{TF}[n] = C\int d\mathbf{r} n(\mathbf{r})^{5/3} + \int d\mathbf{r} V_{ext}(\mathbf{r})n(\mathbf{r}) + \frac{1}{2}\int d\mathbf{r}\int d\mathbf{r}' \frac{n(\mathbf{r})n(\mathbf{r}')}{|\mathbf{r}-\mathbf{r}'|}. \tag{2.13}$$

The first term is the local approximation to the kinetic energy with $C = \frac{3}{10}(3\pi^2)^{2/3} = 2.871$ in atomic units. The second and third terms are the external energy and the classical electrostatic Hartree energy respectively. The density and energy of the ground state can be obtained by the method of Lagrange multipliers, to minimize the above functional $E_{TF}[n]$ for all possible $n(\mathbf{r})$ subject to the constraint of total constant number of electrons:

$$N = \int d\mathbf{r} n(\mathbf{r}), \tag{2.14}$$

leads to the following stationary condition,

$$\delta\{E_{TF}[n] - \mu \int d\mathbf{r} n(\mathbf{r})\} = 0. \tag{2.15}$$

The Lagrange multiplier μ is the Fermi energy. Finally, we got the Thomas-Fermi equations,

$$\frac{5}{3} n(\mathbf{r})^{3/2} + V_{ext}(\mathbf{r}) + \int \frac{n(\mathbf{r}')}{|\mathbf{r} - \mathbf{r}'|} - \mu = 0. \tag{2.16}$$

that can be solved directly to obtain the density of the ground state.

Thomas-Fermi theory suffers from many deficiencies, probably the most serious defect is that it does not predict bonding between atoms, so that solids cannot form in this theory. The main source of error comes from the crude approximation of the kinetic energy, which represents a substantial portion of the total energy of the system. Another shortcoming is the over-simplified description of the electron-electron interactions. It is treated classically and thus neglect the exchange interaction which was lately extended and formulated by Dirac [41]. In next Section, we will introduce the density functional formalism, which is developed based on the Thomas-Fermi model for the electronic structure of materials.

2.5 Density Functional Formalism

In view of the extensive study of the Thomas-Fermi scheme and its well-known deficiencies, we discuss the further developments and improvements of the density functional formalism in this section. Two basic theorems of the density functional formalism were first derived by Hohenberg and Kohn [53]. These remarkably powerful theorems formally established the electron density as the central quantity describing electron interactions in many-body systems. As an exact theory of many-body systems, they can be applied to any system of interacting particles in an external potential, $V_{ext}(\mathbf{r})$. The two theorems are now stated as follows:

- **Theorem 1**. *For any system of interacting particles under the influence of an external potential $V_{ext}(\mathbf{r})$, the external potential $V_{ext}(\mathbf{r})$ is a unique functional of the electron density $n(\mathbf{r})$.*

- **Theorem 2**. *The exact ground state energy can be obtained variationally for any particular $V_{ext}(\mathbf{r})$, the density $n(\mathbf{r})$ that minimises the total energy is the exact ground state density $n_0(\mathbf{r})$.*

According to these two theorems, the total energy functional can be viewed as a functional of $n(\mathbf{r})$ and written in the following form,

$$E_{HK}[n] = T[n] + E_{int}[n] + \int d\mathbf{r} V_{ext}(\mathbf{r}) n(\mathbf{r}) + E_{nn}. \tag{2.17}$$

The functional includes all internal energies $E_{int}[n]$, kinetic energy $T[n]$, the energy of external potential and interaction energy of nuclei E_{nn}. Although the Hohenberg-Kohn theorems are extremely powerful, they do not offer a way of computing the ground-state density of a system in practice. About one year after the seminal DFT paper by Hohenberg and Kohn, Kohn and Sham developed a simple method for carrying-out DFT calculations, that retains the exact nature of DFT [46]. They assume that the ground state density of interacting system is equal to that of certain non-interacting system. This enable us to use the independent-particle Kohn-Sham equation (KS equation) to describe the non-interacting system, which is exactly soluble by incorporating all the difficult many-body terms into an exchange-correlation functional. Therefore, we can obtain the ground state density and energy of the interacting system by solving the KS equations, with the accuracy limited only by the approximations in the exchange-correlation functional.

In the framework of Kohn-Sham approach, the Hohenberg-Kohn expression (2.17) is rewritten as

$$E_{KS}[n] = T_s[n] + E_{Hartree}[n] + \int d\mathbf{r} V_{ext}(\mathbf{r}) n(\mathbf{r}) + E_{nn} + E_{ex}[n], \tag{2.18}$$

which includes the independent-particle kinetic energy,

$$T_s[n] = \frac{1}{2} \sum_{\sigma} \sum_{i=1}^{N^\sigma} |\nabla \psi_i^\sigma|^2, \tag{2.19}$$

the classic Coulomb interaction energy among electrons $E_{Hartree}[n]$ (have been defined as in $E_{TF}[n]$, Eq. (2.13)),

$$E_{Hartree}[n] = \frac{1}{2} \int d\mathbf{r} \int d\mathbf{r}' \frac{n(\mathbf{r}) n(\mathbf{r}')}{|\mathbf{r} - \mathbf{r}'|}, \tag{2.20}$$

the energy of the external potential, interaction of nuclei E_{nn} (the same as in HK expressions) and exchange-correlation energy $E_{ex}[n]$. The exchange-correlation term $E_{ex}[n]$ contains all approximations of many-body effect, which can be comprehended as

$$E_{xc}[n] = \langle T \rangle - T_s[n] + \langle V_{int} \rangle - E_{Hartree}[n]. \tag{2.21}$$

This expression shows explicitly that E_{xc} is just the difference of the kinetic and internal interaction energies of true many-body system from the independent-particle system with

classical Coulomb interaction. For a spin-polarized system with $N = N\uparrow + N\downarrow$ independent electrons, the density is given by the sums of the squares of the orbitals for each spin

$$n(\mathbf{r}) = \sum_{\sigma} n(\mathbf{r}, \sigma) = \sum_{\sigma} \sum_{i=1}^{N^{\sigma}} |\psi_i^{\sigma}(\mathbf{r})|^2. \tag{2.22}$$

The variational equation for the exact functional can be obtained by minimizing the KS expression with respect to the density. In the KS expression of energy (2.18), the kinetic term T_s is written as a functional of orbitals while all other terms are expressed as functionals of the density. Thus, we vary the wavefunctions to derive the variational equation:

$$\frac{\delta E_{KS}}{\delta \psi_i^{\sigma *}(\mathbf{r})} = \frac{\delta T_s}{\delta \psi_i^{\sigma *}(\mathbf{r})} + \Big[\frac{\delta E_{Hartree}}{\delta n(\mathbf{r})} + V_{ext}(\mathbf{r}) + \frac{\delta E_{xc}}{\delta n(\mathbf{r})}\Big] \frac{\delta n(\mathbf{r})}{\delta \psi_i^{\sigma *}(\mathbf{r})} = 0. \tag{2.23}$$

and subject to the normalization constraints

$$\langle \psi_i^{\sigma} | \psi_j^{\sigma'} \rangle = \delta_{i,j} \delta_{\sigma,\sigma'}. \tag{2.24}$$

Using the definitions (2.19) and (2.22) for $n(\mathbf{r})$ and T_s together with the Lagrange multiplier method, we will eventually arrive to the famous Kohn-Sham equation

$$\Big[\frac{1}{2}\nabla^2 + V_{KS}(\mathbf{r})\Big] \psi_i^{\sigma}(\mathbf{r}) = \varepsilon_i \psi_i^{\sigma}(\mathbf{r}) \tag{2.25}$$

with

$$V_{KS}(\mathbf{r}) = \int d\mathbf{r}' \frac{n(\mathbf{r}')}{|\mathbf{r} - \mathbf{r}'|} + V_{ext}(\mathbf{r}) + V_{ex}[n]. \tag{2.26}$$

and

$$n(\mathbf{r}) = \sum_{\sigma} \sum_{i=1}^{occ} |\psi_i^{\sigma}(\mathbf{r})|^2. \tag{2.27}$$

in which ε_i is the eigenvalues and $V_{ex}[n] = \delta E_{xc}[n]/\delta n(\mathbf{r})$ is the functional derivative of the exchange-correlation energy, which is referred to as the "exchange-correlation potential" and is a functional of the electron density.

Compared to the Schrödinger equation, both $\int d\mathbf{r}' \frac{n(\mathbf{r}')}{|\mathbf{r}-\mathbf{r}'|}$ and $V_{ex}[n]$ in the KS equations depend on the density $n(\mathbf{r})$, hence the V_{KS} is a functional of the density. The problem of solving KS equations is non-linear. They can be solved by starting from a trial density $n(\mathbf{r})$ and iterate to self-consistency with the following procedure:

- The KS potential V_{KS} is constructed from the trial density by Eq. (2.26);
- KS orbitals $\psi_i^{\sigma}(\mathbf{r})$ can be obtained by solving Eq. (2.25) with the above KS potential;
- A new density $n'(\mathbf{r})$ is achieved from the KS orbitals $\psi_i^{\sigma}(\mathbf{r})$ related to Eq. (2.27);

- If difference exists between the new density $n'(\mathbf{r})$ and the previous density $n(\mathbf{r})$, repeat the above procedure by starting from a mix of $n(\mathbf{r})$ and $n'(\mathbf{r})$.

The procedure stops until it self-consistently reaches the target precision.

2.6 Exchange and correlation functionals

As we described above, the KS approach can be exactly applied to any many-body system, if the exact exchange-correlation functional $E_{xc}[n]$ is known. This term is very complex, approximations should be used. $E_{xc}[n]$ is often written as a sum of exchange and electron correlation contribution $E_{xc}[n] = E_x[n] + E_c[n]$. KS approach is widely used by reasonably approximating the $E_{xc}[n]$ as a local or nearly local functional of the density.

2.6.1 The Local Density Approximation (LDA)

One of the most widely-used approximations is called The Local Density Approximation (LDA). LDA was firstly proposed by Kohn and Sham in their seminal paper [46]. The $E_{xc}[n]$ simply depends on the density locally and it was constructed exactly in the same spirit as the local approximation to the kinetic energy functional that we discussed in section 2.4.

$$E_{xc}^{LDA}[n] = \int \epsilon_{xc}^{hom}[n] n(\mathbf{r}) d\mathbf{r}. \tag{2.28}$$

From the non interacting homogeneous electron gas, the exchange energy is explicitly known as an analytic term:

$$\epsilon_x^{LDA}[n] = -\frac{3}{4\pi}(3\pi^2 n)^{1/3}. \tag{2.29}$$

The explicit expression of the correlation part $\epsilon_c^{LDA}[n]$ is achieved from accurate quantum Monte-Carlo simulations of the homogeneous electron gas at selected densities [54].

It can be naturally generalized to spin-polarized system, known as Local Spin Density Approximation (LSDA). For a partially polarized homogeneous electron gas, the exchange-correlation energy per electron depends on both the total mean electron density $n = n_\uparrow + n_\downarrow$ and the spin polarization $\sigma = n_\uparrow - n_\downarrow$. By interpolating between the unpolarized and the fully polarized case, we obtain the exchange-correlation energy for LSDA:

$$E_{xc}^{LSDA}[n, \sigma] = \int \epsilon_{xc}^{hom}(n(\mathbf{r}), \sigma(\mathbf{r})) n(\mathbf{r}) d\mathbf{r}. \tag{2.30}$$

Despite its simplicity, the LDA works quite well in many systems, no matter they are quasi-homogeneous or not. It is because LDA fulfils the sum rule on exchange-correlation hole, which gives rise to error compensation on computing the exchange-correlation energy.

Typically, LDA overestimates exchange energy E_x and underestimates correlation energy E_c. LDA has many drawback, we list a few of them:

- The LDA tends to overestimate cohesive energies, resulting in overbinding.
- The electrons are not localised enough in space.
- LDA is appropriate for some s and p electrons, but not for d and f electrons, since it is generalized from homogeneous electron gas.
- The long-range effects (*e.g.* image effects, van der Waals bonds) are completely missing, due to the extremely local nature of the LDA. Therefore, the potential that an electron feels when approaching an atom or a surface is badly described by the LDA. The hydrogen bond is also poorly reproduced in many chemical reactions.

2.6.2 The Generalized Gradient Approximation (GGA)

As expected, any real electron system is non-homogeneous with electron density varying in space. Reasonably, the gradients of the density should be considered into the approximations to describe such variations. However, it was realized that there is no need to include the gradient expansion order by order. Instead, the density and its gradient, is good enough to construct the new functionals, which are currently known as generalized gradient approximations (GGA) [55]:

$$E_{xc}^{GGA}[n,\sigma] = E_{xc}^{LSDA}[n,\sigma] + \int \epsilon_{xc}^{GGA}(n(\mathbf{r}),\sigma(\mathbf{r}))n(\mathbf{r})d\mathbf{r}. \tag{2.31}$$

In many cases, GGA can largely improve LDA results with accuracy, *e.g.* GGA describes XC effects in atoms and molecules much better than LDA. It also has its own drawbacks:

- GGA often overcorrects LDA. Bond lengths are estimated 0-2% larger than experimental values and cohesive energy is resulted in 10-20% smaller.
- GGA cannot describe long-range effects, such as Van der Waals, which is the same as LDA.
- GGA is generally not suitable for strongly correlated electron systems.

2.6.3 DFT+U

The standard approximations in DFT calculations normally give poor answers on the "strongly correlated" systems, in which the potential energy dominates over the kinetic

energy and often involve transition element or rare earth atoms. A common way of modifying DFT calculations is the addition of an on-site Coulomb repulsion ("Hubbard U") as done in the "DFT + U" scheme [56, 57]. The on-site Coulomb interactions are particularly strong for localized d and f electrons, but can be also important for p localized orbitals. The strength of the on-site interactions are usually described by parameters U (on site Coulomb) and J (on site exchange), and practically, by an effective $U_{eff} = U - J$ parameter, while the rest of valence electrons are treated at the level of "standard" approximate DFT functionals. Within DFT+U the total energy of a system can be written as follows:

$$E_{DFT+U} = E_{DFT} + \sum_{\alpha} \frac{U_{eff}}{2} \mathrm{Tr}(\rho^a - \rho^a \rho^a) \tag{2.32}$$

where ρ^a is the atomic orbital occupation matrix. The DFT+U can be understood as adding a penalty functional to the DFT total energy expression that forces the on-site occupancy matrix in the direction to either fully occupied or fully unoccupied levels.

2.7 Computational implementation

2.7.1 Basis sets

In order to solve the KS equations, each orbital $\psi_j(\mathbf{r})$ can be expended on a basis set $f_\alpha(\mathbf{r})$:

$$\psi_j(\mathbf{r}) = \sum_{\alpha} c_{j,\alpha} f_\alpha(\mathbf{r}). \tag{2.33}$$

So that we can transform the problem of solving KS equations into solving a set of linear equations by standard diagonalization method. Here the basis functions are defined on the real space and should form a complete functional space. Any arbitrary function could be expanded as in (2.33).

Plane wave is the most general basis set for the expansion, while for a periodic crystal, according to the Bloch theorem, the KS orbital can be decomposed into a product of a plane wave and a function $u_n(\mathbf{k}, \mathbf{r})$:

$$\psi_{n,\mathbf{k}}(\mathbf{r}) = \frac{1}{\sqrt{\Omega}} u_{n,\mathbf{k}}(\mathbf{r}) e^{i\mathbf{k}\cdot\mathbf{r}}, \tag{2.34}$$

where Ω is the volume of the cell, $\mathbf{k}$ is a wave vector of the reciprocal space. $u_{n,\mathbf{k}}(\mathbf{r})$ is a periodic function, $u_{n,\mathbf{k}}(\mathbf{r} + \mathbf{R}) = u_{n,\mathbf{k}}(\mathbf{r})$. It can be further expanded in a discrete Fourier expression:

$$u_{n,\mathbf{k}}(\mathbf{r}) = \sum_{\mathbf{G}} c_{n,\mathbf{k}}(\mathbf{G}) e^{i\mathbf{G}\cdot\mathbf{r}}, \tag{2.35}$$

where $\mathbf{G}$ is the vector of reciprocal space, $c_{n,\mathbf{k}}(\mathbf{G})$ are the Fourier coefficients in the wave vector space. In practice, we cannot include infinite number of plane waves, such an expansion should be truncated at a crucial energy level, which is called cut-off energy E_{cut}:

$$\frac{\hbar^2}{2m}|\mathbf{k}+\mathbf{G}|^2 \leq E_{cut}. \tag{2.36}$$

Optimization of E_{cut} is determined through a compromise between numerical accuracy and computational burden.

2.7.2 K-points mesh

Consider a finite system with an integer number $N = N_1N_2N_3$ of unit cells. Because of the Born-von Karman conditions, the number of k wave-vectors in the Brillouin zone (BZ) is equal to $N = N_1N_2N_3$ and their density to $\Omega_0/(2\pi)^3$. The electronic density in DFT is calculated through the integration of the square modulus of the Bloch functions on all occupied energy bands and over the Brillouin zone. The integration over the reciprocal space involves the choice of an optimal finite set of k-points, which is often referred to as Brillouin zone sampling. The method proposed by H. J. Monkhorst and J. D. Pack [58] is one of the most widely used sampling techniques, which allows to sample a uniform grid of k-points along each direction, using a simple formula:

$$\mathbf{k}_{n_1,n_2,n_3} = \sum_{i}^{3} \frac{2n_i - N_i - 1}{2N_i}\mathbf{G}_i. \tag{2.37}$$

We notice that, the high symmetric points (points in the center and boundary of the BZ) are excluded in this method. Indeed, the electronic bands may be flat or degenerate in highly symmetric k-points, which would artificially reinforce the computed weight of such electronic transitions. The k-points sampling depends on the symmetry of the system and must be converged in each case study by increasing its size.

2.7.3 Pseudo-potentials

Problems arise when we are using the plane waves to describe the core electrons. Since these electrons are closely around the nucleus, the wave function oscillates rapidly due to the large attractive potential of the nucleus. It needs a large number of plane waves to describe correctly the behavior of these electrons, which largely increases the time consuming of the calculations. To solve this problem, we refer to the methods that are based on plane waves in conjunction with pseudopotentials [59]. The pseudopotential is an effective potential that "froze" the core electrons together with the nuclei, so that the ionic potential screened by the core electrons is replaced by such a smoothly varying potential.

This allows us to use fewer Fourier modes to describe pseudo-wavefunctions, making plane-wave basis sets practical to use. The pseudopotentials are constructed so as to reproduce the total effect of the nucleus and core electrons on the valence electron wave-functions, requiring the pseudo potential wavefunctions to reproduce the exact wavefunction beyond a certain cut-off radius from the core. Pseudopotentials with larger cut-off radius are said to be softer, that is more rapidly convergent, however, at the same time less transferable, that is less accurate to reproduce realistic features in different environments.

In our calculations we adopted to a more general approach, projector augmented wave method (PAW), which naturally generalizes both the pseudopotential method and the linear augmented-plane-wave method [60]. The strategy is to seek a linear transformation $\hat{T}$ which linked from an auxiliary smooth wave function $|\tilde{\psi}_n\rangle$ to the true all electron Kohn-Sham single particle wave function $|\psi_n\rangle$

$$|\psi_n\rangle = \hat{T}|\tilde{\psi}_n\rangle \tag{2.38}$$

where $\hat{T}$ is explicitly written as

$$\hat{T} = 1 + \sum_i \sum_a (|\phi_i^a\rangle - |\tilde{\phi}_i^a\rangle)\langle\tilde{p}_i^a| \tag{2.39}$$

including three sets of quantities: all-electron partial waves $|\phi_i\rangle$, pseudo wave $|\tilde{\phi}_i\rangle$ and projector functions $|\tilde{p}_i\rangle$. Following the above strategy, we have separated the original wave functions into auxiliary smooth wave functions and a contribution which contains rapid oscillations, but only contributes in augmentation spheres.

2.8 Polarization

In this subsection, we introduce the fundamentals of the modern theory of polarization. The macroscopic polarization is an essential property of ferroelectrics and the dielectric materials in the phenomenological theory. As we have described in the first chapter, the spontaneous polarization is an important order parameter indicating the ferroelectric phase transition. Classically, it is defined as a vector quantity equal to the electric dipole moment per unit volume. The standard picture is based on the venerable Clausius-Mossotti (CM) model, in which the presence of identifiable polarizable units is assumed. The charge distribution of a polarized system is regarded as the superposition of localized contributions, each of them provides an electric dipole. In a crystalline structure, the CM macroscopic polarization is defined as the sum of the dipole moments in a given cell divided by the cell volume.

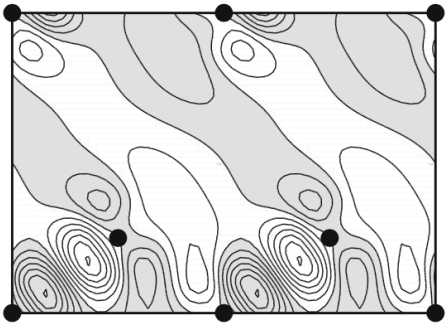

Figure 2.1: Example of charge density in real materials. Shaded areas indicate regions of negative charge; circles indicate atomic positions [5]

However, in real materials, the picture is more inhomogeneous. Specially in typical FE oxides, the bonding has a mixed ionic/covalent character, with a sizeable fraction of the electronic charge being shared among ions in a delocalized manner, for example see Figure 2.1. This fact makes any CM picture inadequate.

Experimentally, the method to estimate the spontaneous polarization of ferroelectric materials is through measurement of the hysteresis loop of P versus electric field E. This hysteresis loop is obtained experimentally by the measurement of the integrated macroscopic current $j(t)$ through the sample during a time t:

$$\Delta P = \int_0^{\Delta t} j(t)dt = P(\Delta t) - P(0) \tag{2.40}$$

In periodic systems, the Born-Oppenheimer approximation allows us to decompose the total polarization into two parts, ionic and electronic contributions:

$$\mathbf{P} = \mathbf{P}_{ion} + \mathbf{P}_{el} \tag{2.41}$$

The ionic part can be written by following the classic definition

$$\mathbf{P}_{ion} = \frac{e}{\Omega} \sum_{\kappa} Z_{\kappa} \mathbf{R}_{\kappa} \tag{2.42}$$

where Ω is the volume of the cell and Z_κ is the charge of the core ion κ at position $\mathbf{R}_\kappa$. While the electronic contribution is formalised as the Berry phase of the occupied bands [61]:

$$\mathbf{P}_{el} = -\frac{2ie}{(2\pi)^3} \sum_{n=1}^{m} \int_{BZ} < u_{n\mathbf{k}} | \nabla_{\mathbf{k}} | u_{n\mathbf{k}} > d\mathbf{k} \tag{2.43}$$

where m is the number of occupied electronic states, u_{nk} is the lattice-periodical part of the Bloch wave function. We should notice that $A(k) = i < u_{n\mathbf{k}} | \nabla_{\mathbf{k}} | u_{n\mathbf{k}} >$ is a "Berry connection" or "gauge potential" and its integral over the Brillouin zone is known

as a "Berry phase". The expression requires that the system must remain insulating everywhere along the path in order to keep the adiabatic condition. Remarkably, in the adiabatic condition, the result is independent of the path traversed through parameter space, so that the result depends only on the final state. In practice, the integration is over a discrete grid of k-points in the Brillouin zone, and the polarization is modulated by a quantum $e\mathbf{R}/\Omega$,

$$\Delta\mathbf{P} := (\mathbf{P}_{\lambda=1} - \mathbf{P}_{\lambda=0}) \mod \frac{e\mathbf{R}}{\Omega} \tag{2.44}$$

where $\mathbf{R}$ is the lattice vector. The symbol ":=" is introduced here to indicate that the value on the left-hand side is equal to one of the values on the right-hand side.

3

Ferroelectric instability in nanotubes and spherical nanoshells

Due to the finite-size effects, in most of the small particles, the transition temperature T_c can drop dramatically as the size reduces. Such a ferroelectric instability limits the applications of ferroelectrics in nano devices. In this chapter, we use phenomenological approach to investigate the emergence of ferroelectricity in the novel confined geometries, *i.e.* nanotubes and spherical nanoshells, due to their special topologies. Specifically, we study semi-analytically the size and thickness dependence of the ferroelectric instability, as well as its dependence on the properties of the surrounding media and the corresponding interfaces. By properly tuning these factors, we demonstrate possible routes for enhancing the ferroelectric transition temperature and promoting the competition between irrotational and vortex-like states in ultra-thin limit.

3.1 Introduction

Ferroelectric nanoparticles, such as nanodots, nanowires, nanotubes et al. receive a considerable research attention [62, 63, 64, 65, 66, 67, 68, 69, 70, 71, 72] and novel fabrication methods are being developed [73, 74]. The case of ferroelectric nanotubes and nanoshells is particularly interesting, as their specific topology can be exploited for engineering additional functionalities relevant for technological applications [62, 63, 75].

However, one of the limiting factors of these systems is the ferroelectric instability itself, as the corresponding transition temperature T_c can drop drastically due to finite-size effects. Such a phenomenon has been investigated in both experimental and theoretical studies.[5, 63, 67, 76, 77, 78, 79, 80, 81, 82]. Levanyuk et al. investigated the ferroelectric

phase transition in both 2D and 3D nanostructures within Landau-Ginzburg-Devonshire theory. They studied the stability of a paraelectric phase with respect to different polarization distributions (homogeneous polarization and vortex structures) to find the phase transition temperature and the profile of polarization appearing at the phase transition. The loss of stability is indicated by the appearance of nontrivial solutions of equations consisting of linearized governing equations for polarization, the electrostatic equations, and the boundary conditions [67].

In this chapter, we address this crucial point within the Ginzburg-Landau-like formalism, with which we describe analytically the ferroelectric transition in nanotube and nanoshell geometries. Thus, we extend the considerations reported in [65, 66, 67, 68, 71] to novel geometries of experimental relevance. Specifically, in the case of ferroelectric nanotubes, we will consider the electric polarization perpendicular to their axis. In addition to the overall size effect, we analyse the impact of the thickness, relative permittivities, and boundary conditions on the possible competition between different type of polarization distributions.

3.2 Method

The emergence of ferroelectricity in a finite-size system is ultimately determined by two fundamental factors [79, 83].

On one hand, there is the tendency towards ferroelectricity itself, which can satisfactorily be modelled within the Ginzburg-Landau formalism [79]. For this we consider the free energy:

$$F = \frac{1}{2}aP^2 + \frac{1}{4}bP^4 + \frac{1}{2}g\big(|\nabla P_x|^2 + |\nabla P_y|^2 + |\nabla P_z|^2\big) + \mathbf{P}\cdot\nabla\phi, \tag{3.1}$$

where $\mathbf{P}$ is the ferroelectric polarization, $a = a'(T - T_{c0})$ is the inverse susceptibility, with T_{c0} being the nominal transition temperature ($a' = \text{const.}$), g is associated to the gradient term, and ϕ is the electric potential. This provides the constitutive equation that, to our purposes, can be linearized and taken as

$$(a - g\nabla^2)\mathbf{P} = -\nabla\phi, \tag{3.2}$$

For the sake of simplicity, the response of the ferroelectric is assumed to be isotropic – either completely (nanoshell) or within the ferroelectric plane (nanotube). As in [67, 71], this approximation is expected to capture the key qualitative features of the ferroelectric instability [1].

[1] A more realistic description including *e.g.* strain fields is beyond the scope of this inaugural work

On the other hand, there is a purely electrostatic aspect described by Gauss's law:

$$\nabla \cdot (\varepsilon \nabla \phi - \mathbf{P}) = 0, \tag{3.3}$$

where ε is the so-called background permittivity [84], and the corresponding boundary conditions [79, 83]. Thus, whenever $\nabla \cdot \mathbf{P} \neq 0$, the spontaneous polarization will be penalised by the accompanying electric potential and the corresponding increase of electrostatic energy.

3.3 Irrotational polarization

Following [67], the task is to find the nontrivial solution of the above equations that can appear at the highest T (*i.e.*, for the maximum value of the coefficient a). This search can be restricted to the family of divergenceless distributions of polarization ($\nabla \cdot \mathbf{P} = 0$) that automatically minimize (most of) the electrostatic energy in the ferroelectric. Furthermore, two subfamilies can be identified among the targeted distributions: i) irrotational distributions ($\nabla \times \mathbf{P} = 0$) and ii) vortex-like states ($\nabla \times \mathbf{P} \neq 0$). In the first case the gradient energy is minimised at the expense of some electrostatic energy generated by interfacial bound charges (depolarizing field). In the second case the situation is reversed, and the electrostatic energy is minimised at the expense of some gradient energy in the ferroelectric. These cases will be analysed separately for the different geometries of interest, and the results will be illustrated by considering the material parameters of $BaTiO_3$. In the case of a cylinder or a sphere, the only possible irrotational distribution of polarization corresponds to the $\mathbf{P}$ = constant (homogeneous polarization). The presence of the internal boundary in the nanotube or the nanoshell, however, introduces more complex patterns. In this case, since $\nabla^2 \mathbf{P} = \nabla(\nabla \cdot \mathbf{P}) - \nabla \times (\nabla \times \mathbf{P}) = 0$, the above equations reduce to the Laplace equation $\nabla^2 \phi = 0$ ($\mathbf{P} = -a^{-1} \nabla \phi$). We thus adopt cylindrical (r, θ, z) and spherical (r, θ, φ) coordinates for the nanotube and the nanoshell respectively, and consider the solutions:

$$\phi_{2D}(r, \theta) = (A_n r^n + B_n r^{-n}) \cos(n\theta), \tag{3.4}$$

$$\phi_{3D}(r, \theta) = (A_n r^n + B_n r^{-n-1}) P_n(\cos\theta), \tag{3.5}$$

for the electrostatic potential, where $P_n(x)$ represent the Legendre polynomials. Hereafter $R_{1(2)}$ represents the internal (external) radius. The irrotational distributions of polarization are illustrated in Fig. 1. $n = 1$ corresponds to the homogeneous polarization for $R_1 = 0$ [see Fig. 1(a)]. Whenever $R_1 \neq 0$, however, the resulting polarization is inhomoge-

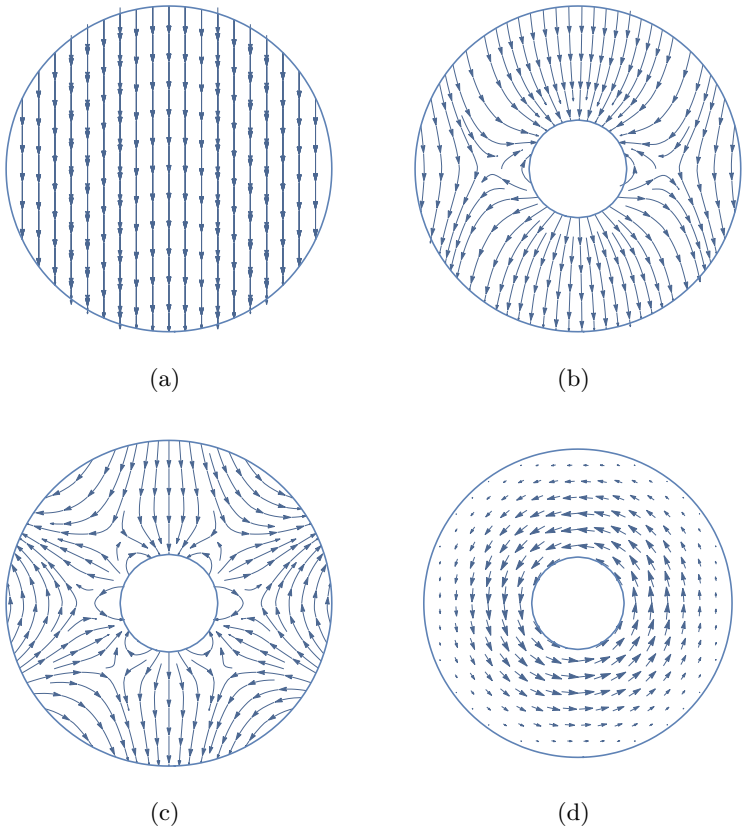

Figure 3.1: Irrotational distributions of polarization (a)∼(c) and vortex-like polarization (d) across the cross section of a ferroelectric nanotube. (a) and (b) correspond to $n = 1$, while (c) to $n = 3$.

neous [Fig. 1(b)], and this inhomogeneity increases with the corresponding order n [Figs. 1(c)].

We consider first the (2D) case of a nanotube. The electric potential ϕ has to be continuous at R_1 and R_2, while its gradient has to be such that $\varepsilon \boldsymbol{n} \cdot \nabla\phi\big|_{R_i^-}^{R_i^+} = \sigma_{R_i}$. Here $\boldsymbol{n}$ is the normal unit vector to the interface while σ_{R_i} represents the interfacial charge density. In order to ensure charge neutrality, the interfacial charge densities can be taken as $\sigma_{R_1} = -\left(\frac{R_1}{R_2}\right) P_0 \cos(n\theta)$ and $\sigma_{R_2} = P_0 \cos(n\theta)$, with P_0 being a constant. Thus, the solutions (3.4) become compatible with the boundary conditions whenever the condition

$$(\varepsilon_{FE} + \varepsilon_2)(\varepsilon_{FE} + \varepsilon_1) = (\varepsilon_2 - \varepsilon_{FE})(\varepsilon_1 - \varepsilon_{FE}) \left(\frac{R_1}{R_2}\right)^{2n} \tag{3.6}$$

is satisfied. Here $\varepsilon_{FE} = \varepsilon + a^{-1}$ is the permittivity of the ferroelectric, while ε_1 and ε_2 are those of inner and outer medium respectively. Eq. (3.6) determines the hypothetical T_c associated to the irrotational solutions (3.4) as a function of R_1/R_2 and the corresponding order n, which is illustrated in Fig. 2. As we can see, while all orders tend to be degenerate

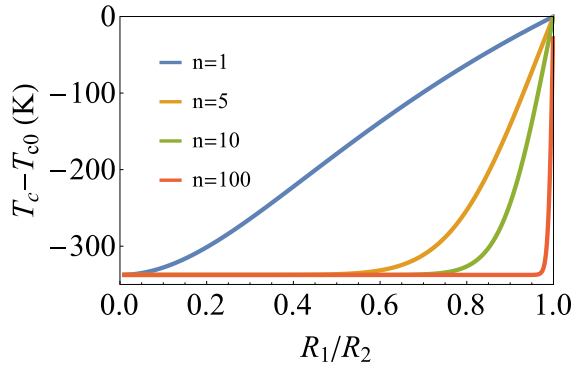

Figure 3.2: T_c associated to irrotational distributions of polarization in ferroelectric nanotubes. $R_2 = 25$ nm, $a' = 6.6 \times 10^5$J m C^{-2}K^{-1}, $\varepsilon_1 = 100\varepsilon_0$ and $\varepsilon_2 = 500\varepsilon_0$.

in the limits $R_1 = 0$ and $R_1 = R_2$, the highest T_c corresponds to the $n = 1$ solution and this hierarchy is maintained for all the radii R_1/R_2.

In the (3D) case of the nanoshell, the interfacial charge densities can be taken as $\sigma_{R_1} = -\left(\frac{R_1}{R_2}\right)^2 P_0 P_n(\cos\theta)$ and $\sigma_{R_2} = P_0 P_n(\cos\theta)$. Thus, the compatibility between the solutions (3.5) and the electrostatic boundary conditions implies

$$\begin{aligned}&[n\varepsilon_{FE} + (n+1)\varepsilon_2]\,[(n+1)\varepsilon_{FE} + n\varepsilon_1] = \\ &\quad n\,(n+1)\,(\varepsilon_2 - \varepsilon_{FE})\,(\varepsilon_1 - \varepsilon_{FE})\left(\frac{R_1}{R_2}\right)^{2n+1}.\end{aligned} \tag{3.7}$$

We now have two different situations depending on the relative permittivities ε_1 and ε_2. If $\varepsilon_1 < \varepsilon_2$ the degeneracy at $R_1 = 0$ is lifted, although the $n = 1$ solution has always the highest T_c as in the previous (2D) case. If $\varepsilon_1 > \varepsilon_2$, however, this hierarchy is reversed for small R_1 and, interestingly, a crossover is obtained as the R_1/R_2 ratio increases.

Interestingly, in both 2D and 3D cases, the strong suppression of the T_c of the irrotational polarization can be moderated in the limit $R_1/R_2 \to 1$. However, the question of whether they can be realised experimentally eventually depends on the competition with other families of solutions. In the following we consider the vortex-like patterns, as they are the most serious contenders.

3.4 Vortex state

In our systems, a vortex-like distribution of polarization implies $\nabla \cdot \boldsymbol{P} = 0$ everywhere, and hence $\phi = 0$. Thus, the emergence of this type of polarization is simply governed by the equation $(a - g\nabla^2)\boldsymbol{P} = 0$ under the corresponding boundary conditions. The solutions

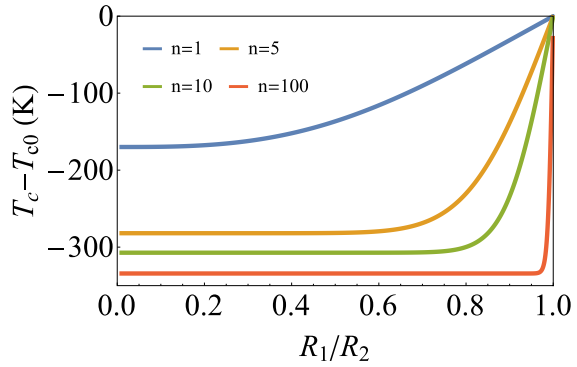

(a) $\varepsilon_1 < \varepsilon_2$

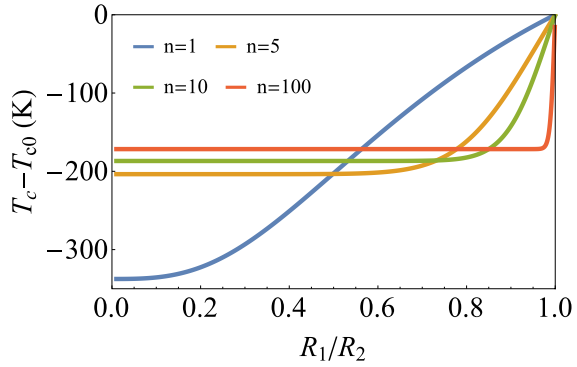

(b) $\varepsilon_1 > \varepsilon_2$

Figure 3.3: The relation between T_c-T_{c0} and R_1/R_2 with respect to different orders of FE nanoshell structure. (a) $\varepsilon_1 = 100\varepsilon_0$ and $\varepsilon_2 = 500\varepsilon_0$ while for (b) $\varepsilon_1 = 1000\varepsilon_0$ and $\epsilon_2 = 100\varepsilon_0$, other parameters are the same as nanotube.

of interest can be written as $\boldsymbol{P} = P_\varphi(r)\hat{\mathbf{e}}_\varphi$ where

$$P_\varphi^{2D}(r) = C_1 J_1(r/r_c) + C_2 Y_1(r/r_c), \tag{3.8}$$

$$P_\varphi^{3D}(r) = C_1 j_1(r/r_c) + C_2 y_1(r/r_c), \tag{3.9}$$

for the (2D) nanotube and (3D) nanoshell geometries respectively. Here $r_c = (g/a)^{1/2}$ is the correlation length, J_1 and Y_1 are Bessel functions of first and second kind, while j_1 and y_1 are spherical Bessel functions of first and second kind respectively. The T_c associated to these vortex-like distributions of polarization depends on the boundary conditions. We consider the general boundary conditions $(1 \pm \lambda\partial_r)P|_{R_i} = 0$, where λ is the so-called extrapolation length [79]. Thus, in the (2D) case of a nanotube T_c is determined by

$$\begin{aligned}\left[J_1\left(\frac{R_1}{r_c}\right) - \frac{\lambda}{r_c}J_1'\left(\frac{R_1}{r_c}\right)\right]\left[Y_1\left(\frac{R_2}{r_c}\right) + \frac{\lambda}{r_c}Y_1'\left(\frac{R_2}{r_c}\right)\right] = \\ \left[J_1\left(\frac{R_2}{r_c}\right) + \frac{\lambda}{r_c}J_1'\left(\frac{R_2}{r_c}\right)\right]\left[Y_1\left(\frac{R_1}{r_c}\right) - \frac{\lambda}{r_c}Y_1'\left(\frac{R_1}{r_c}\right)\right].\end{aligned} \tag{3.10}$$

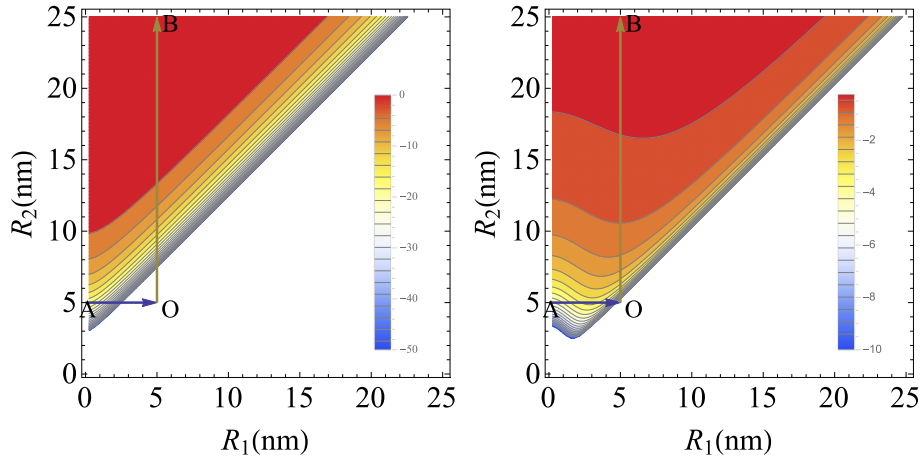

(a) $\lambda = 0nm$ (b) $\lambda = 25nm$

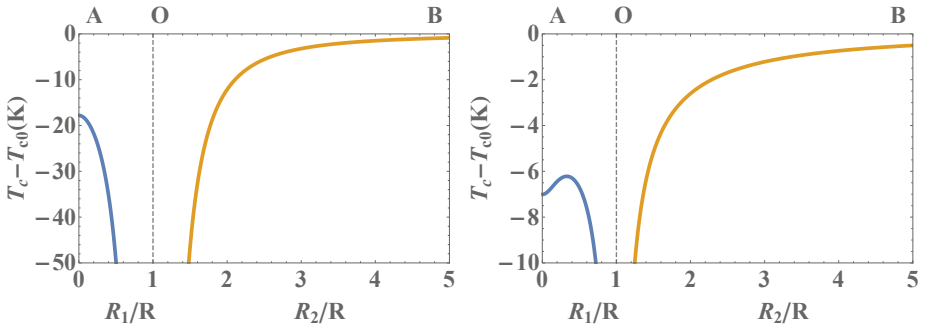

(c) $\lambda = 0nm$ (d) $\lambda = 25nm$

A similar equation is obtained for the (3D) nanoshell case with J_1 $(Y_1) \rightarrow j_1$ (y_1). For the sake of simplicity, we consider that the two interfaces are described by the same λ [1].

We find that the T_c as a function of R_1 and R_2 can show rather different behaviors when these parameters are varied separately. This is eventually determined by the extrapolation length λ, as illustrated in Fig. 4 for the case of a ferroelectric nanotube. Specifically, the "topography" of the $T_c(R_1, R_2)$ map changes in such a way that its maximum gradient rotates by 45° as λ goes from 0 to ∞. Thus, for $\lambda = 0$, T_c decreases by decreasing the thickness of the shell. That is, by either increasing R_1 or decreasing R_2 [A-O and B-O paths respectively in Fig. 4(a), which correspond to blue and orange lines in the bottom plot]. For a finite λ [Fig. 4(b)-(c)], however, T_c initially increases by increasing R_1 and then decreases after reaching a maximum. By decreasing R_2, in contrast, the behavior is monotonous and T_c always decreases. For $\lambda = \infty$, which corresponds to the so-called natural boundary conditions $\partial_r P = 0$, the dependency on the nanotube thickness is different for different paths [Fig. 4(d)]. While T_c increases by increasing R_1, it decreases by decreasing R_2. This unequivalence in the finite-size effect is related to the

[1] Qualitatively, the same results are obtained for different extrapolation lengths

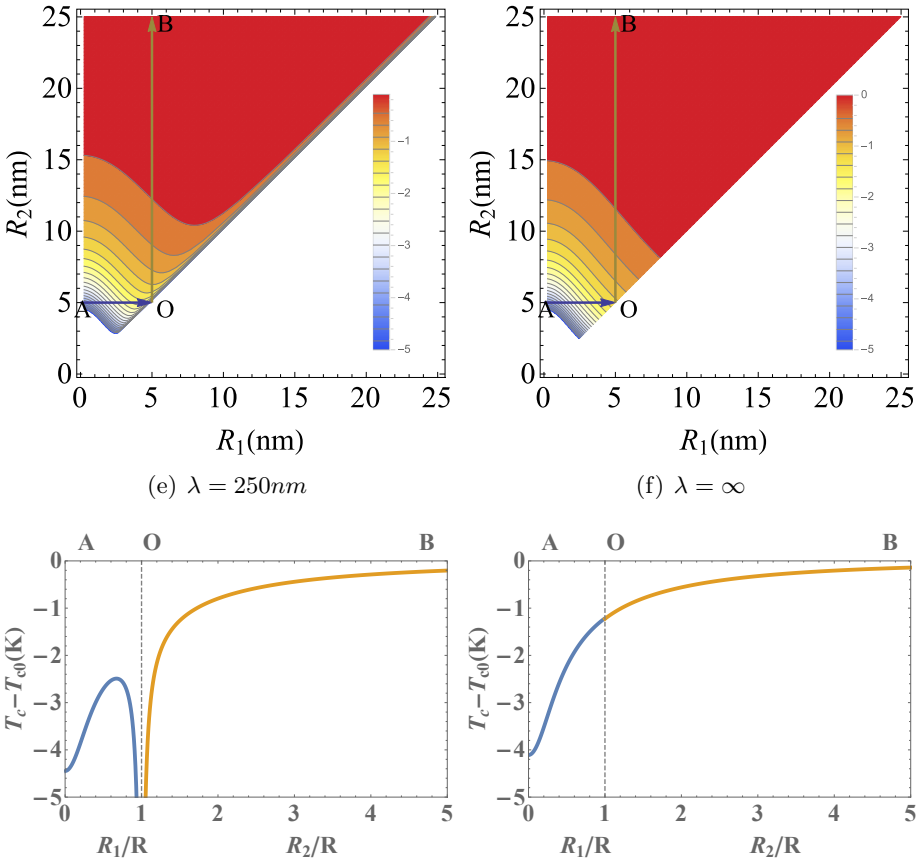

(e) $\lambda = 250nm$ (f) $\lambda = \infty$

(g) $\lambda = 250nm$ (h) $\lambda = \infty$

Figure 3.4: Transition temperature for vortex-like polarization state in a ferroelectric nanotube ($g = 2 \times 10^{-11}$J m^{-3}C^{-2}). (a)(b)(e)(f) Contour plots for T_c-T_{c0} as a function of internal (R_1) and external (R_2) radii of the nanotube. (c)(d)(g)(h) T_c-T_{c0} along the paths A-O (blue) and B-O (orange).

specific topology of the systems under consideration. In fact, in the case of the nanoshell, the T_c associated to the vortex-like distribution of polarization behaves qualitatively in the same way within the approximations of our model.

We note that, compared to the irrotational states, the T_c associated to vortex-like distributions of polarization is generally much closer to its nominal value T_{c0} (irrespective of the properties of the surrounding media). However, when $R_1/R_2 \to 1$, the T_c for the vortices can drop significantly while that of the irrotational distributions approaches T_{c0}. Thus, we find that the specific topology of these systems enables the competition between different type of polarization distributions in the ultra-thin limit.

3.5 Conclusions

In summary, we have studied theoretically the ferroelectric instability in nanotubes and spherical nanoshells. Specifically, we have considered semi-analytically different families of polarization distributions and examined how their emergence is affected by the thickness of the nanoparticle, the dielectric properties of the surrounding media, and the interfacial boundary conditions. We have found an intriguing topological finite-size effect that can promote the competition between different types of ferroelectricity in the ultra-thin limit. These results illustrate new routes to control the ferroelectric instability and engineer ferroelectric properties at the nanoscale. This possibility is expected to motivate both extended theoretical analyses and future experimental work.

4

Pressure-induced insulator-metal transition in $EuMnO_3$

Taking a different route from the previous chapter, in the following chapters, we turn to the theoretical study on distorted lattice structures by applying external stimuli. Specifically, we investigate the multi-functionality of orthorhombic perovskites by first-principles method.

In this chapter, we study the influence of external pressure on the magnetic and electronic structure of $EuMnO_3$. We find a pressure-induced insulator-metal transition at which the magnetic order changes from A-type antiferromagnetic to ferromagnetic with a strong interplay with Jahn-Teller distortions. In addition, we find that the non-centrosymmetric E^*-type antiferromagnetic order can become nearly degenerate with the ferromagnetic ground state in the high-pressure metallic state. This situation can be exploited to promote a magnetically-driven realization of a non-centrosymmetric (ferroelectric-like) metal.

4.1 Introduction

Manganese-based perovskite oxides are well known for displaying the colossal magnetoresistance (CMR) phenomenon. This intriguing feature is associated to a paramagnetic-insulator to ferromagnetic-metal transition taking place in these systems. CMR compounds mainly derive from the prototypical perovskite $LaMnO_3$, where the insulator-metal transition can be induced by either doping with divalent cations such as Ca, Sr and Ba [85, 86] or external pressure [87, 88, 89]. One the other hand, the rare-earth manganites $R\mathrm{MnO}_3$ (R = Eu, Gd, Tb, ..., Lu) provide an outstanding subfamily of manganites with a very rich temperature-composition phase diagram [90]. These $R\mathrm{MnO}_3$ compounds display

in particular multiferroicity, a property that holds great promises for a novel generation of spintronic devices and related applications.

In contrast to the CMR manganites, no insulator-metal phase transition has been reported in the multiferroic RMnO$_3$ systems so far. Broadly speaking, the multiferroic RMnO$_3$ compounds are found to be insulators whose magnetic ground state can evolve from an A-type antiferromagnetic (A-AFM) state to spin-spiral order and then to an E-type antiferromagnet (E-AFM). This happens in particular if the effective R-ion radius is reduced. Such a "chemical-pressure"-induced transformation can be interpreted in terms of enhanced magnetic frustration and its likely competition with biquadratic coupling, which favor non-collinear spiral states and collinear E-AFM states respectively [91, 92]. As a result of this interplay, two prominent realizations of magnetically-induced ferroelectricity can be observed in these systems. On one hand, we have the spontaneous electric polarization due to spin spiral order as originally observed in TbMnO$_3$ [18]. This is currently understood as due to antisymmetric magnetostriction via the so-called inverse Dzyaloshinskii-Moriya or spin-current mechanism [35, 36, 93]. On the other hand, we also have ferroelectricity linked to collinear E-AFM order as observed in HoMnO$_3$ [94, 95]. In this case, the spontaneous polarization is expected from symmetric magnetostriction terms and is generally much larger than other spin-driven ferroelectrics [96], as we have already discussed in Sec 1.3.6.

Recently, the application of external pressure has been found to have a similar effect to that of "chemical-pressure" in multiferroic RMnO$_3$ [22, 97]. The spontaneous polarization of TbMnO$_3$, in particular, has been found to increase dramatically above ~ 4.6 GPa, which is interpreted as due to the stabilization of the E-AFM order over the initial spiral order of the Mn spins [22]. A similar increase of the polarization has subsequently been observed in GdMnO$_3$ and DyMnO$_3$ [97]. At the same time, the behavior of the corresponding polarization under magnetic field suggests that the rare-earth magnetic moments can interact with the Mn spins and hence have a substantial interference with their pressure-induced multiferroic properties. Motivated by these findings, here we study the effect of pressure on the magnetic order of EuMnO$_3$ from first-principles calculations.

EuMnO$_3$ has the R-ion with the largest ionic radius among the multiferroic RMnO$_3$ compounds. Interestingly, its magnetic properties clearly emerge from the Mn spins since, unlike the other rare-earth manganite multiferroics, the Eu-ion is in a non-magnetic state. Multiferroicity can be induced by *e.g.* Y doping in this system. Thus, as a result of the Y-induced chemical-pressure, the system undergoes the whole sequence of phase transitions A-AFM $\leftrightarrow$ spiral state $\leftrightarrow$ E-AFM by varying the Y content [91, 92]. In view of this, the application of external pressure can be expected to have a similar effect on this system. In this paper we show from first-principles calculations that external pressure has,

however, a dramatically different influence on $EuMnO_3$. Specifically, the application of pressure transforms the A-AFM-insulator state directly into a FM-metal. This unexpected pressure-induced insulator-to-metal transition, although similar to the observed in CMR $LaMnO_3$, is unprecedented within the multiferroic RMnO$_3$ series. In addition, we find that the non-centrosymmetric E*-AFM state is also metallic in this system and becomes quasi-degenerate with the FM ground state under pressure. These features make $EuMnO_3$ an unique compound among the manganites because it behaves differently with respect to physical and "chemical" pressure, and hosts a genuinely new type of ferroelectric-like metallic state. To some extent, $EuMnO_3$ can be regarded as bridging the gap between the CMR and multiferroic manganite compounds.

4.2 Methods

Our density functional theory (DFT) based calculations are performed with projected augmented waves (PAW) potentials as implemented in the VASP code [98, 99]. We use the generalized gradient approximation (GGA) PBEsol [100] exchange correlation functional and apply an on-site Coulomb correction for the Mn-3d states characterized through DFT+U scheme [57]. The Eu-4f electrons are treated as core electrons. We consider the most relevant Mn-spin collinear orders found in manganites. Namely, ferromagnetic (FM), A-, E- and E*-AFM orders as discussed in Chapter 1. Note that E- and E*-AFM states correspond to the same in-plane Mn spin ordering but with AFM and FM inter-plane coupling respectively. In addition, we also consider two representative cases of non-collinear spin-spiral antiferromagnetic order: the 60° spiral order with propagation vector $k = 1/3$ in the bc plane and its 90° version with $k = 1/2$. In our calculations we neglect the spin-orbit coupling. This coupling produces corrections that are at most one order of magnitude smaller than the symmetric exchange interactions [see *e.g.* Ref. [101]]. Thus, even if it plays a key role for the multiferroic properties (by *e.g.* determining the value and orientation of the spin-driven electric polarization in the spiral phases [35, 36, 93]), it does not introduce qualitative changes in the magnetic phase diagram of the rare-earth manganites [22, 91]. For the collinear orders and the 90° spiral order we use an $a \times 2b \times c$ orthorhombic $Pbnm$ supercell with $6 \times 3 \times 4$ Monkhorst-Pack k-points sampling, while the 60° spiral configuration is constructed in an $a \times 3b \times c$ supercell using $4 \times 2 \times 3$ k-points grid. The cutoff energy for plane waves is set at 500 eV.

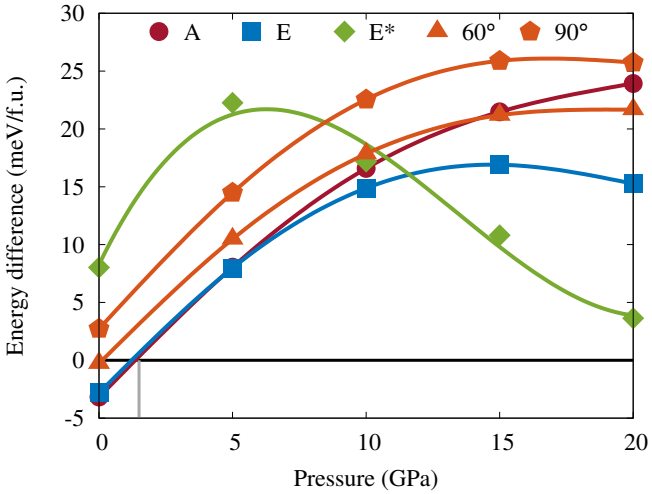

Figure 4.1: Energy of the A-AFM, E-AFM, E*-AFM 60° and 90° spiral states as a function of pressure taking the FM state as the reference state. The FM state becomes the ground state at $\sim$ 2 GPa.

4.3 Results

4.3.1 A-AFM to FM transition

In Figure 4.1, we plot the energy difference between the A-AFM, E-AFM, E*-AFM, 60° and 90° spiral states and the FM state as a function of pressure. The results are obtained by fully relaxing the lattice parameters and internal atomic positions with a Hubbard parameter $U = 1$ eV. We find that the A-AFM state has the lowest energy from ambient pressure to $\sim$2 GPa, while the next energy state corresponds to the E-AFM order. However, by increasing the pressure, the reference FM state eventually has the lowest energy, and hence becomes the ground state of the system. We find that the transition between A-AFM and FM orders occurs at $\sim$ 2 GPa. This transition corresponds to a first-order phase transition in which the net magnetization jumps from 0 to 3.7 μ_B/Mn.

Together with this transition, we find that the E-AFM order could display a lower energy compared to the A-AFM order when the pressure exceeds 5 GPa. This is in tune with what is observed in the Tb, Gd and Dy compounds [22, 97]. In addition, we observe that, while they can compete with the E*-AFM state at low pressure, both 60° and 90° spiral orders are always above in energy compared with the FM state. When it comes to the E*-AFM state, its energy displays an intriguing behavior under pressure. As can be seen in Figure 4.1, the energy of this state shows an important decrease from 5 GPa and tends to the value of the FM state at high pressure ($\Delta E = 3.6$ meV/f.u. at 20 GPa and further decrease to 2.0 meV/f.u. at 22 GPa).

The zigzag spin-order of the E*-AFM breaks inversion symmetry and transforms the

initial *Pbnm* space-group symmetry of the system into the non-centrosymmetric $P2_1nm$ one with a spontaneous polar distortion that emerges via symmetric magnetostriction [96]. This distortion defines two domains and in principle can be switched by means of its direct link to the E*-AFM underlying structure. The stabilization of this state then could bring multifuntional properties in $EuMnO_3$ in analogy with the one observed in $TbMnO_3$. However, according to our calculations, in $EuMnO_3$ the E*-AFM state stays nearly degenerate with the FM state above 20 GPa but it never becomes the ground state of the system.

4.3.2 Metallic character of the FM state

In Figures 4.2(a) and 4.2(b), we show the density of states (DOS) of the A-AFM state at 0 GPa and the FM state at 5 GPa respectively. The A-AFM DOS displays a gap of 0.5 eV and is symmetric between spin-up and spin-down states. The DOS of FM state, on the contrary, has no gap at the Fermi energy for spin-up state, whereas it is gaped for spin-down state. This finite DOS is dominated by the contribution of Mn-3d orbitals, with a non-negligible contribution of O-2p ones. We note that this band structure does not come from a mere shift of the A-AFM one, but results from important reconstruction in which structural distortions play a role as we show below. Using different values of the U parameter we obtain essentially the same results, and hence we conclude that the FM state in $EuMnO_3$ is therefore a half-metal. Thus, we find that the pressure-induced A-AFM to FM transition is, in addition, an insulator-metal transition.

In addition, the DOS associated to the E*-AFM order reveals that this state is also metallic as shown in Figure 4.2(c). In this case, the contribution of the Mn-3d orbitals in the DOS at the Fermi level is even more dominant compared to the FM state. Since type of order is accompanied with a polar distortion of the crystal structure that in principle can be switched, the E*-AFM state in $EuMnO_3$ can be seen as an intriguing realization of a magnetically-induced ferroelectric-like metal.

4.3.3 Interplay between metallicity and Jahn-Teller distortions

The insulator-metal transition in the reference compound $LaMnO_3$ takes place from a highly Jahn-Teller distorted structure to weakly distorted one and hence is strongly interconnected to the lattice [89, 102, 103]. In order to investigate this aspect in $EuMnO_3$, we performed a symmetry-adapted mode analysis of the distortions that accompany the magnetic orders using the program ISODISTORT [104]. Thus, we compare the virtual cubic structure with the *Pbnm* structures obtained for the FM, A-AFM and 60° spiral orders and the $P2_1nm$ structures obtained for the E-AFM and E*-AFM ones. All these

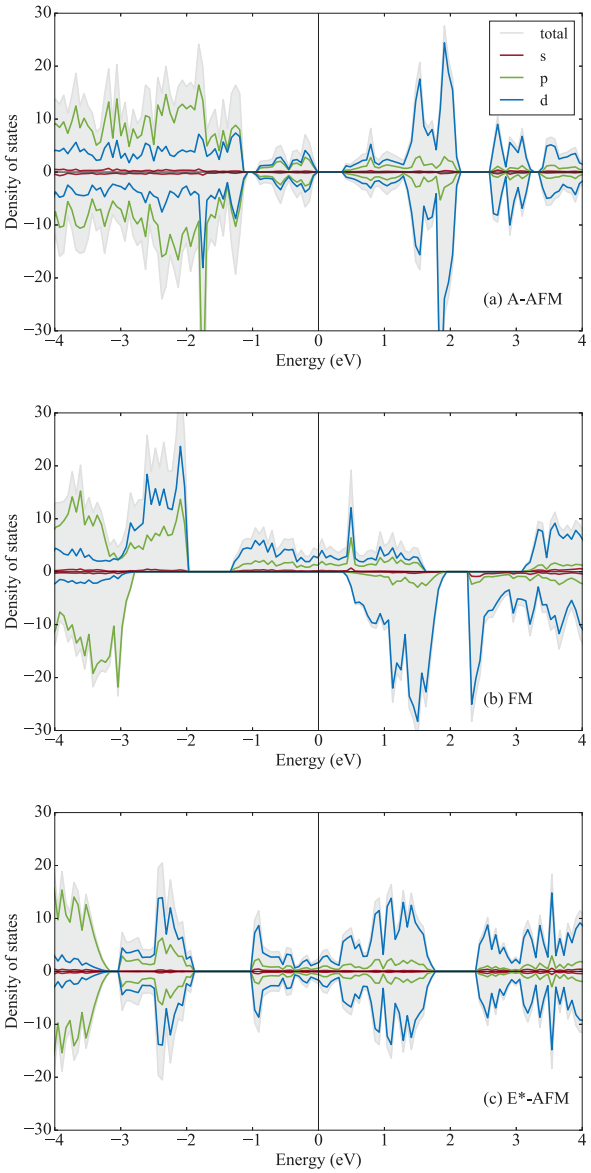

Figure 4.2: Spin-polarized DOS of (a) A-AFM (0 GPa), (b) FM (5 GPa) and (c) E*-AFM (20 GPa) states of $EuMnO_3$, where the Fermi level has been shifted to 0 (vertical black line). Total (grey area) and partial (s, p and d-electrons) DOS are shown, spin-up and -down electrons are mapped on positive and negative area separately. The initial A-AFM ground state transforms into the metallic FM state under pressure. The metastable E*-AFM state is also metallic and tends to be nearly degenerate with the FM state at high pressure.

structures contain Jahn-Teller distortions associated to the M_3^+ and the Γ_3^+ modes (Q_2 and Q_3 respectively in the traditional notation, see *e.g.* [105]). The evolution of these distortions as a function of pressure is shown in Fig. 4.3.

As we can see, the system displays an abrupt decrease of the Jahn-Teller distortions at the metal-insulator transition due to the different weight of these modes in the A-AFM and FM states. Besides, the amplitude of these distortions taken separately decreases

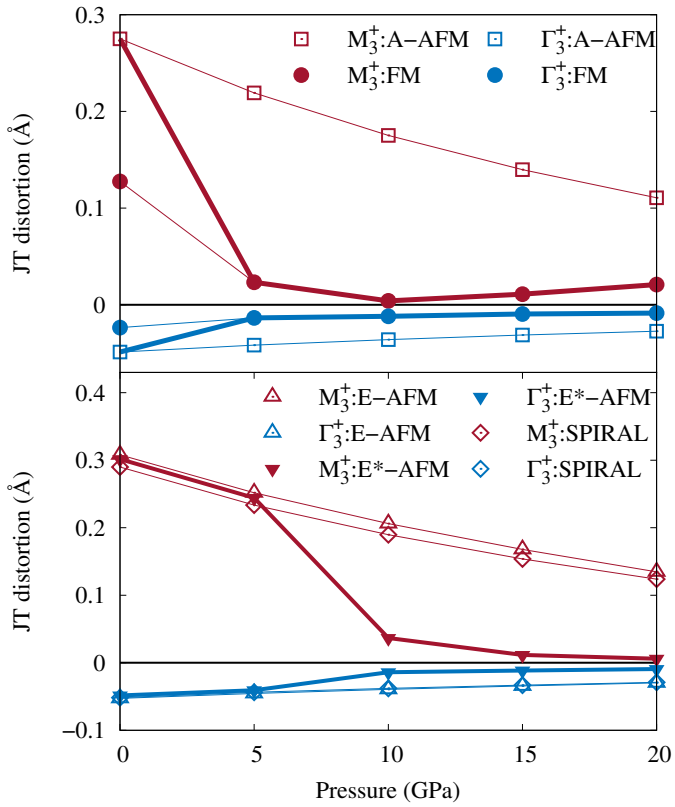

Figure 4.3: Amplitude of the M_3^+ (red) and Γ_3^+ (blue) Jahn-Teller modes as a function of pressure for the different magnetic orders considered above. Open (close) symbols indicate insulating (metallic) states. The thick lines in the top panel highlight the evolution of the Jahn-Teller distortions in the ground state across the insulator-metal transition. The thick lines in the bottom panel highlight the evolution in the (metastable) E*-AFM metallic state.

for each state by increasing the pressure, which can be interpreted as an increase of the corresponding stiffness. This reduction, however, has a step-like feature for the metallic FM and E*-AFM states while it is gradual for the insulating states. This interplay between Janh-Teller distortion and metallicity has indeed a correspondence to the one observed in $LaMnO_3$ [see *e.g.* [87, 88, 89, 102, 103]], and hence establishes a parallelism between these two compounds unnoticed so far.

4.4 Discussion

4.4.1 Robustness of the first-principles calculations

Our first-principles calculations suggest that an insulator-to-metal transition can be induced in $EuMnO_3$ by applying external pressure. In order to assess the reliability of this prediction, we have carefully analyzed the main premises of these calculations.

First of all, we checked the dependence of the results on the Hubbard U parameter [see Sec. 4.4.1.1]. It has been shown that the U correction applied on Mn d orbitals can be taken as zero in other compounds of the RMnO$_3$ series such as TbMnO$_3$ [22]. In EuMnO$_3$, however, $U = 0$ eV gives the E-AFM state as the ground state of the system at ambient pressure, and hence is inconsistent with the A-AFM state observed experimentally [see table 4.1 in Sec. 4.4.1.1]. The experimental ground state at ambient pressure is correctly reproduced with $U \geq 1$ eV. Thus, the need of a small but non-zero U parameter in EuMnO$_3$ makes this system a genuinely correlated system compared to other multiferroic manganites. Nonetheless, in order to avoid artifacts due to unphysical correlations, we take the lowest possible value of the U parameter that is compatible with the experiments [*i.e.* $U = 1$ eV, see Sec. 4.4.1.1].

The optimization of the crystal structure turns out to be a crucial point in our calculations. To verify our method, we carried out a comparative study of TbMnO$_3$ and EuMnO$_3$ [see Sec. 4.4.1.2]. While we reproduce the results reported in Ref. [22] for TbMnO$_3$, where the authors did their calculation at fixed cell parameters by imposing A-AFM order, we however find that these results are strongly affected by structural relaxations. The results for EuMnO$_3$, in contrast, are totally robust with respect to structure changes, which supports the predictive power of our calculations. Specifically, the observed competition between spiral and E-AFM order in TbMnO$_3$ is captured only by means of the very specific optimization procedure followed in Ref. [22], while usual optimization schemes fail. This seems to be related to an overestimation of the corresponding magnetostriction couplings and possibly to the interplay between the Mn spins and the additional order of the Tb ones. In this respect, EuMnO$_3$ turns out to be a more robust system where the insulator-to-metal transition is always obtained, together with the accompanying changes in the magnetic properties.

The evolution of EuMnO$_3$ under pressure presented in this work has been studied with full atomic and cell relaxations. The lattice parameters obtained in this way are compared to the experimental data [106] in Figure 4.4. As we can see, the PBEsol functional produces a good agreement (within a 2% error) with the experimental data for all the magnetic structures. We note that the distortions along b axis are slightly larger in the FM and E*-AFM states, which turns out to be an important parameter to minimize the overall energy. Thus, we expect a correct description of the predicted transition at the qualitative level, although the precise value of the *e.g.* transition pressure has to be taken with a grain of salt. This is illustrated in our analysis of the dependence of the transition against the U parameter and the structure optimization procedure [see Sec. 4.4.1.1 and 4.4.1.2]. From this analysis we see that different U's produce different values of the transition pressure, and a similar shift is obtained as a function of the optimization procedure. The important

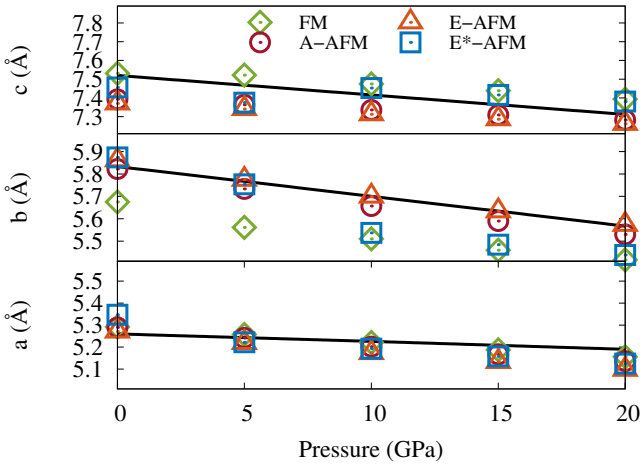

Figure 4.4: Experimental lattice parameters as a function of pressure obtained from Ref. [106] (black lines) and calculated ones for FM, A-AFM, E-AFM and E*-AFM orders.

U value	FM	A-AFM	E-AFM
0 eV	0	-2.3	**-18.4**
1 eV	0	**-3.2**	-2.8
2 eV	0	**-4.5**	4.8

Table 4.1: Total energy (unit: meV/f.u.) of A-AFM and E-AFM phase with respect to FM one for $U = 0, 1, 2$ eV at ambient pressure.

point is, however, that the application of external pressure, no matter which calculation procedure we follow, systematically results into a insulator-metal transition in $EuMnO_3$ that, fundamentally, is always the same. This calls for experimental studies on $EuMnO_3$ under pressure to determine the exact critical pressure of the transition.

4.4.1.1 Dependence on the Hubbard U parameter

In table 4.1, we list the total energy of A-AFM and E-AFM order by taking FM one as the reference state, calculated with U =0, 1, 2 eV at ambient pressure. The results show the ground state is E-AFM phase for $U = 0$ eV, whereas A-AFM one for U =1, 2 eV, as we stated in the main text. In Figure 4.5(a) we show the results obtained for $U = 2$ eV. As for $U = 1$ eV, both the lattice parameters and the internal positions are obtained self-consistently for each magnetic state. In Figure 4.5(a) we see that, compared to the results of $U = 1$ eV (Figure 4.1), the relative energy of the E-AFM and E*-AFM states is shifted upwards. At the same time, the relative energy between the A-AFM order and the FM one remains basically the same and the same crossover is obtained at a slightly higher pressure of ~ 4 GPa. The qualitative picture is thus similar for $U = 1$ and $U = 2$ eV. The

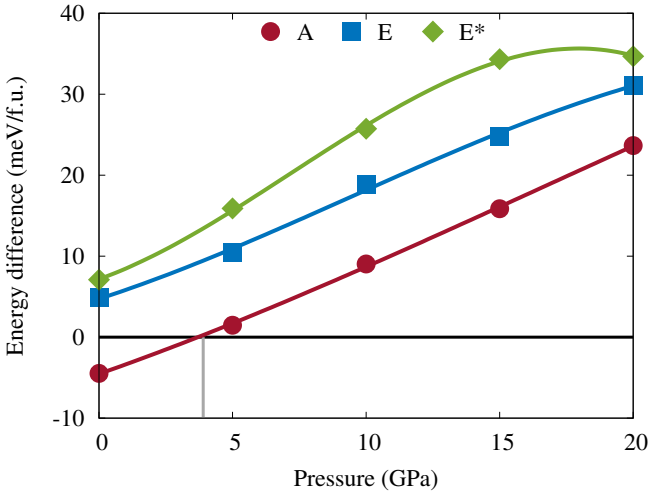

(a)

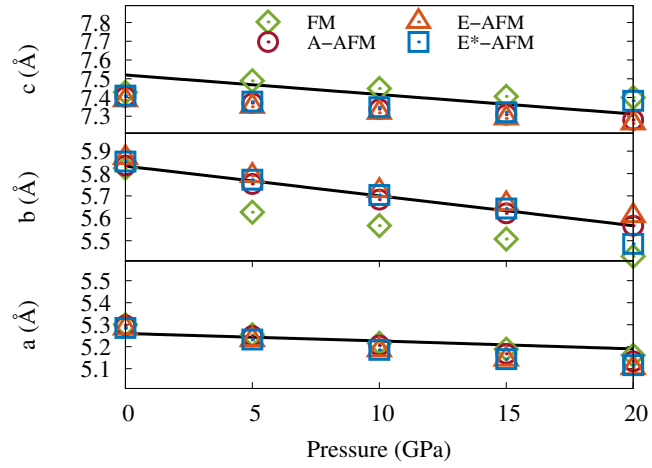

(b)

Figure 4.5: (a) Relative energy of the different magnetic orders as a function of pressure for $U = 2$ eV. The lattice parameters and the internal atom positions are obtained self-consistently for each magnetic order. (b) Experimental lattice parameters (black lines) and calculated ones for $U = 2$ eV.

lattice parameters obtained in this way are compared with the experimental data in Figure 4.5(b). The degree of agreement is essentially the same as the one obtained for $U = 1$ eV [see Figure 4.4]. This confirms that the qualitative prediction of pressure-induced A-AFM (insulator) to FM (metal) transition in $EuMnO_3$ is robust with respect to the choice of the U parameter.

4.4.1.2 Dependence on the structure optimization scheme

In Figure 4.7 we compare the results obtained for $TbMnO_3$ and $EuMnO_3$ according to different schemes of structure optimization. For $TbMnO_3$ we took $U = 0$ eV as in Ref.

[22]. For $EuMnO_3$ we took $U = 1$ eV to obtain the correct ground state at ambient pressure as explained in the main text. In Figure 4.7(a) and 4.7(b) we plot the results obtained by following the structure optimization described in Ref. [22]. In their paper they relaxed the internal coordinates within the A-AFM state at the experimental cell parameters and kept this peculiar relaxed structure fixed to compute the energy of the other magnetic states. Even if the A-AFM state is never observed to be the ground state in $TbMnO_3$ at any pressure, the results obtained in this way reproduce the experimental transition remarkably well [see Figure 4.7(a) and Ref. [22]]. The overestimation of the transition pressure in our calculations could be related to different convergence precision used in Ref. [22] (2 meV/f.u.). In the case of $EuMnO_3$, if we follow this procedure the A-AFM to FM transition occurs at a much higher pressure (not shown in 4.7(b)). Otherwise, as we discussed in the main text, the qualitative picture remains basically the same.

In Figure 4.7(c) and 4.7(d) we show the results obtained according to a more physical procedure of structure optimization. In this case the lattice parameters are also fixed to the experimental values, but the internal atomic coordinates are relaxed for each magnetic phase at each value of the pressure. This procedure captures magnetostriction effects that are ignored in the previous procedure. These effects can indeed be important as they promote *e.g.* the spin-driven spontaneous electric polarization. As we see in Figure 4.7(c), this method changes completely the picture in $TbMnO_3$. Specifically, among the considered states, the E-AFM state becomes the ground state already at zero pressure (while it becomes the ground state beyond 9 GPa if one uses the A-AFM structural parameters). Experimentally, however, the ground state corresponds to the spiral order. This means that, once magnetostriction effects are switched on, none of the considered spirals reproduce adequately the actual ground state of $TbMnO_3$. $EuMnO_3$, in contrast, does not have this complication. For this crystal the overall qualitative picture remains the same, even if the energy difference between the different states is now reduced due to the additional energy minimization that comes from magnetostriction effects [see Figure 4.7(d)]. These magnetostriction couplings then pull the transition pressure down compared to the one obtained according to the procedure of Ref. [22].

For the procedure discussed in the main text, magnetostriction effects are fully taken into account as both lattice parameters and internal positions are relaxed self-consistently for each magnetic state separately. This explains the additional shift of the insulator-to-metal transition, and the subsequent possibility of achieving the quasi-degeneracy between FM and E*-AFM states.

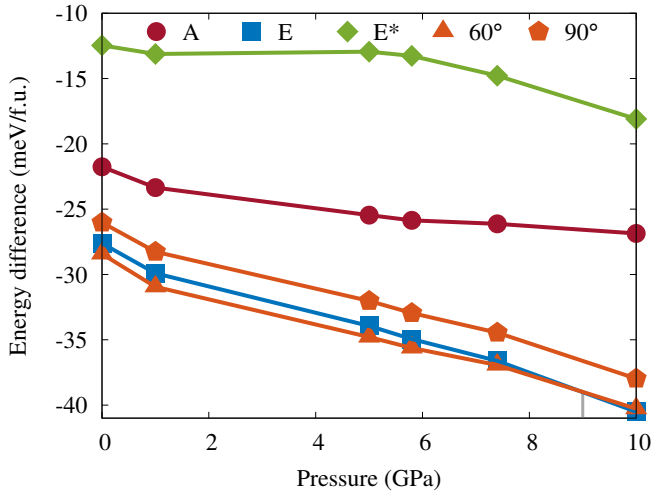

(a)

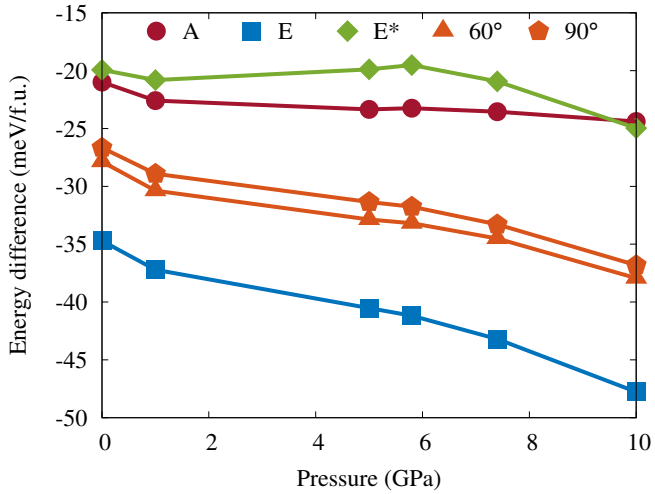

(b)

Figure 4.6: Comparative study of the structure optimization procedure in $TbMnO_3$. The lattice parameters correspond to their experimental values while the internal positions are obtained following two different methods. (a) A-AFM order is imposed and the internal positions are obtained by optimizing the internal coordinates in this magnetic state. The output is used to compute the energy associated to the other magnetic orders, with no additional optimization. This method is used in Ref. [22] for $TbMnO_3$, although the A-AFM state is not the ground state of this system. (b) The internal positions are relaxed self-consistently for each type of magnetic order separately. We note the strong sensitivity of the E-AFM against the structural relaxations, which changes the qualitative description of $TbMnO_3$ under pressure.

4.4.2 Mapping to a Heisenberg model

In order to gain additional insight about the microscopic cause of the predicted A-AFM-insulator to FM-metal transition, we follow Refs. [22, 107] map the magnetic energy of

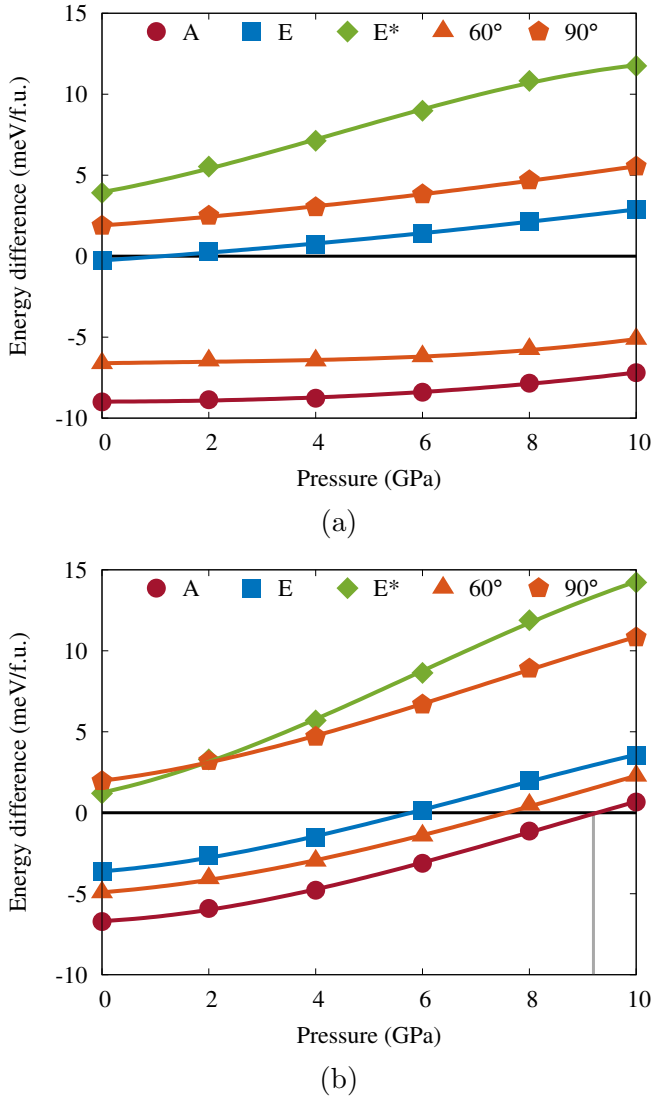

Figure 4.7: Comparative study of the structure optimization procedure in $EuMnO_3$, using the same methods as those used in $TbMnO_3$ in Figure 4.6.

the system into a simple Heisenberg model plus a biquadratic coupling term:

$$\begin{aligned}\mathcal{H} = J_{ab} \sum_{\langle n,m \rangle}^{ab} \mathbf{S}_n \cdot \mathbf{S}_m + J_c \sum_{\langle n,m \rangle}^{c} \mathbf{S}_n \cdot \mathbf{S}_m \\ + J_a \sum_{\langle\langle n,m \rangle\rangle}^{ab} \mathbf{S}_n \cdot \mathbf{S}_m + J_b \sum_{\langle\langle n,m \rangle\rangle}^{ab} \mathbf{S}_n \cdot \mathbf{S}_m \\ + B \sum_{\langle n,m \rangle}^{ab} (\mathbf{S}_n \cdot \mathbf{S}_m)^2. \end{aligned} \tag{4.1}$$

Here J_{ab} and J_c represent nearest-neighbor interactions in the ab plane and along the c axis respectively, while J_a and J_b are second-nearest-neighbor interactions along aA and

b respectively. The biquadratic coupling is restricted to nearest neighbors in the ab-plane only and its strength is determined by the B parameter. The competition between FM nearest- and AFM second-nearest-neighbor interactions is a source of magnetic frustration in the rare-earth manganites. This can be quantified by means of the ratio $J_{a(b)}/|J_{ab}|$. Thus, the frustration criterion of spiral configuration is 1/2: $J_{a(b)}/|J_{ab}| < 1/2$ favors FM order while $J_{a(b)}/|J_{ab}| > 1/2$ favors the spiral state. J_c simply determines if the stacking along c is FM or AFM, while $B \neq 0$ favors collinear orders.

In order to determine the parameters of Eq. 4.1 in the $Pbnm$ structure, we compute the energy associated to the FM, A-, C-, 90° spiral, and the E-AFM sate with the induced polarization along two perpendicular directions (E_a- and E_b-AFM with $2a \times b \times c$ and $a \times 2b \times c$ supercells respectively) for different pressures between 0 and 20 GPa. In terms of the parameters of the Hamiltonian 4.1 these energies are

$$\begin{aligned}
E_{\text{FM}} &= E_0 + 4(2J_{ab} + J_c + J_a + J_b + 2BS^2)S^2, \\
E_{\text{A-AFM}} &= E_0 + 4(2J_{ab} - J_c + J_a + J_b + 2BS^2)S^2, \\
E_{\text{C-AFM}} &= E_0 + 4(-2J_{ab} + J_c + J_a + J_b + 2BS^2)S^2, \\
E_{E_a\text{-AFM}} &= E_0 + 4(-J_c - J_a + J_b + 2BS^2)S^2, \\
E_{E_b\text{-AFM}} &= E_0 + 4(-J_c + J_a - J_b + 2BS^2)S^2, \\
E_{90^\circ\text{spiral}} &= E_0 + 4(-J_c + J_a - J_b)S^2,
\end{aligned} \tag{4.2}$$

where E_0 represents the energy of the non-magnetic state. In Figure 4.8, we plot the solution of this system of equations as a function of pressure, where the Mn^{3+} spin is taken as $S = 2$. The parameters obtained from this mapping elucidates the intriguing competition between the different magnetic orders in $EuMnO_3$. First of all, we note that the second-nearest-neighbor exchange parameters J_a and J_b are both AFM with a much weaker anisotropy than reported in $TbMnO_3$ [92, 108]. The first-order transition from A-AFM to FM state implies the abrupt change of these parameters followed by a more gradual variation. J_c, in particular, changes from positive to negative. In $TbMnO_3$ the biquadratic interaction is enhanced under pressure, which is important for the stabilization of the collinear E-AFM phase observed in this system. In $EuMnO_3$, on the contrary, the biquadratic coupling is rather small compared with the exchange interactions at ambient pressure. Furthermore, such a coupling is not enhanced by applying pressure, and therefore is not able to promote the C-AFM state. This eventually enables the emergence of the FM order and the accompanying metallicity of the system under pressure.

The mapping to the Heisenberg model, however, has to be taken with some reservations. If we estimate the Néel temperature following a mean-field treatment of the system, we obtain $T_N^{\text{A-AFM}} \approx 199$ K [see Sec. 4.4.3]. The experimental value, however, is 49

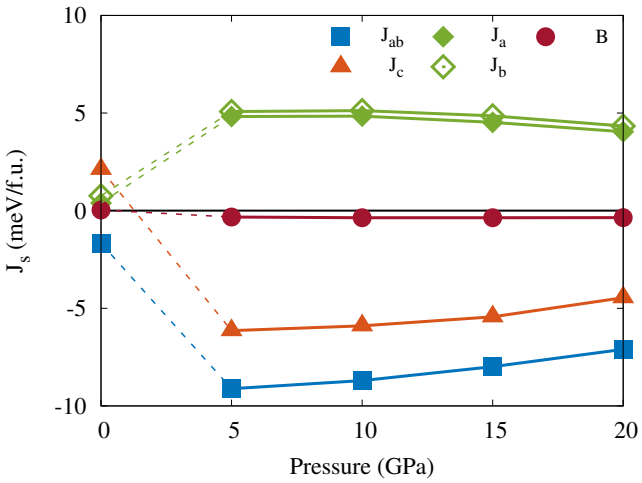

Figure 4.8: Exchange parametres J_{ab}, J_c, J_a and J_b and biquadratic coupling B of the Heisenberg model of Eq. 4.1 as a function of pressure. The abrupt change of these parameters at the A-AFM to FM transition is indicated by the dashed line.

K [109]. One of the possible reasons of this discrepancy can be related to the metallic character of the FM state itself, as we included this state to compute the $J's$. In such a state, the localized-spin picture may not be fully appropriate (even if we find a rather large magnetic moment at the Mn's in the FM state) and/or the exchange interactions can be longer ranged. This point requires further investigations that, however, are beyond the scope of the present paper.

4.4.3 Mean-field theory for Néel temperature

We estimate the Néel temperature of A-AFM using a mean field theory [110] based on the exchange parameters J's we obtained from total energy DFT calcuations. We can rewrite the hamiltonian of the i^{th} atom in term of an effective magnetic field (first consider interaction with its nearest-neighbours),

$$\mathcal{H}_i = J\mathbf{S}_i \cdot \sum_j^z \mathbf{S}_j = -g\mu_B \mathbf{S}_i \cdot \mathbf{H}_{eff}, \tag{4.3}$$

where g and μ_B are the Lande factor and Bohr magneton respectively, z is the total number of its nearest neighbours, . Then we have

$$\mathbf{H}_{eff} = -\frac{J}{g\mu_B}\sum_j^z \mathbf{S}_j = -\frac{zJ}{g\mu_B}\langle S_j \rangle, \tag{4.4}$$

here, we assume all magnetic atoms are identical and equivalent, $\langle S_j \rangle$ is related to the total magnetic moment by $M = Ng\mu_B\langle S_j \rangle$, N is the total number of atoms in the whole

cell, so that we can rewrite the H_{eff} as a function of total magnetic moment:

$$\mathbf{H}_{eff} = -\frac{zJ}{Ng^2\mu_B^2}\mathbf{M}. \tag{4.5}$$

Therefore, we obtain the molecular field coefficient for the nearest-neighbour interaction,

$$\gamma = -\frac{zJ}{Ng^2\mu_B^2}. \tag{4.6}$$

Generalize the case to include further interactions, we summarize the total field acting on an atom in the i^{th} sublattice as

$$H_i = H_0 + \sum_{k=1}^{n} \gamma_{ik} M_k, \tag{4.7}$$

M_k is the magnetic moment of the k^{th} sublattice and γ_{ik} is the molecular field coefficient for the field acting on an atom in i^{th} sublattice by its neighbors in k^{th} sublattice, which is defined as:

$$\gamma_{ik} = \begin{cases} 0 & i = k \\ -\frac{n(z_{ik}J_{ik})}{Ng^2{\mu_B}^2} & i \neq k \end{cases} \tag{4.8}$$

The first case ($i = k$) shows that an atom has no interactions with any neighbors of its own sublattice. For the second case ($i \neq k$), n is the number of sublattices, z_{ik} is the number of kth neighbors of i atom, J_{ik} is the exchange interaction between an i atom and a kth neignbor atom. It is convenient to consider only the high temperature approximation, we have

$$\begin{aligned} M_i &= \frac{C}{nT} H_i \\ &= \frac{C}{nT}(H_0 + \sum_{k=1}^{n} \gamma_{ij} M_k) \qquad i = 1, 2, 3, ..., n. \end{aligned} \tag{4.9}$$

This is a set of n linear algebraic equations, we can write them explicitly

$$\begin{aligned} M_1 - \frac{C}{nT}\gamma_{12}M_2 - ... - \frac{C}{nT}\gamma_{1n}M_n &= \frac{C}{nT}H_0 \\ -\frac{C}{nT}\gamma_{21}M_1 + M_2 - ... - \frac{C}{nT}\gamma_{2n}M_n &= \frac{C}{nT}H_0 \\ &..... \\ -\frac{C}{nT}\gamma_{n1}M_1 - \frac{C}{nT}\gamma_{n2}M_2 - ... + M_n &= \frac{C}{nT}H_0. \end{aligned} \tag{4.10}$$

To determine the transition temperatures in the generalized molecular field theory, we can simply set $H_0 = 0$ and solve a linear homogeneous set of equations. We will have non-zero

solutions for the M_i only if the determinant of the coefficients is zero.

$$\begin{vmatrix} \frac{nT}{C} & -\gamma_{12} & \cdots & -\gamma_{1n} \\ -\gamma_{21} & \frac{nT}{C} & \cdots & -\gamma_{2n} \\ \cdots & \cdots & \cdots & \cdots \\ -\gamma_{n1} & -\gamma_{n2} & \cdots & \frac{nT}{C} \end{vmatrix} = 0 \tag{4.11}$$

Since the anisotropy in the in-plane second-nearest-neighbor interactions is very weak, we simplify this interaction and consider the averaged value $J_2 = (J_a + J_b)/2$ in the following. Thus, we can construct the determinantal equation of the form

$$\begin{vmatrix} a_0 & a_1 & a_2 & a_1 & a_3 & 0 & 0 & 0 \\ a_1 & a_0 & a_1 & a_2 & 0 & a_3 & 0 & 0 \\ a_2 & a_1 & a_0 & a_1 & 0 & 0 & a_3 & 0 \\ a_1 & a_2 & a_1 & a_0 & 0 & 0 & 0 & a_3 \\ a_3 & 0 & 0 & 0 & a_0 & a_1 & a_2 & a_1 \\ 0 & a_3 & 0 & 0 & a_1 & a_0 & a_1 & a_2 \\ 0 & 0 & a_3 & 0 & a_2 & a_1 & a_0 & a_1 \\ 0 & 0 & 0 & a_3 & a_1 & a_2 & a_1 & a_0 \end{vmatrix} = 0, \tag{4.12}$$

for the eight magnetic atoms of the $a \times 2b \times c$ orthorhombic $Pbnm$ supercell. Here

$$a_0 = \frac{8T}{C}, a_1 = -4\gamma_1, a_2 = -8\gamma_2, a_3 = -8\gamma_3, \tag{4.13}$$

where T is the temperature, C is the Curie constant $C = \frac{NS(S+1)}{3k_B} g^2 \mu_B^2$, and the γ's are related to the exchange parameters J_i as

$$\gamma_i = -\frac{z_i J_i}{N g^2 \mu_B^2}, \tag{4.14}$$

with $J_1 = J_{ab}$ and $J_3 = J_c$. Among the eight solutions of the Eq. (4.12),

$$a_0 = -2a_1 - a_2 + a_3 \tag{4.15}$$

corresponds to the A-AFM state. Thus, from Eqs. (4.13) to (4.15) the Néel temperature of A-AFM state can be estimated as

$$T_N^{\text{A-AFM}} = \frac{-2S(S+1)}{3k_B} \left(2J_{ab} + J_a + J_b - J_c\right). \tag{4.16}$$

4.5 Conclusions

We performed a first-principles investigation of the structural, electronic and magnetic structure of $EuMnO_3$ under pressure. We found a pressure-induced insulator-metal transition that is unprecedented in the multiferroic rare-earth manganites $RMnO_3$. This tran-

sition is accompanied with a change of the magnetic order from E-AFM to FM, which preempts the spiral and E-AFM phases that normally promote multiferroicity in these systems. The overall transition, in addition, displays a strong interplay with Jahn-Teller distortions similar to the one observed in $LaMnO_3$. $EuMnO_3$ thus establishes an interesting link between colossal-magnetoresistance and multiferroic manganties. We also found that the non-centrosymetric E*-AFM state is metallic in $EuMnO_3$ and tends to be nearly degenerate with the FM ground state at high pressures. Thus, $EuMnO_3$ hosts a potential realization of a new type of (magnetically-induced) ferroelectric metal that can add an extra dimension to the thought-provoking question of ferroelectricity emerging in metals [111, 112, 113, 114, 115]. These findings are expected to motivate further experimental and theoretical work.

5

Epitaxial-strain-induced multiferroic and polar metallic phases in $R\mathrm{MnO}_3$

Motivated by the quasi-degenerate ground state E*-AFM of $EuMnO_3$ induced by pressure in our previous chapter, we continue to exploit more functionalities in the rare-earth manganites by DFT calculations. Instead of pressure, we use epitaxial strain, which offers more flexibilities on structural alteration.

In this chapter, we simulate the strained $TbMnO_3$ and $EuMnO_3$ thin film in both (001) and (010) orientations. We obtain the magnetic and electric phase diagrams for these compounds as a function of strain. Specifically, we predict that both the multiferroic E-AFM order and the polar metallic E*-AFM state are stabilized in $TbMnO_3$ in a particular range of epitaxial strain. In contrast, we predict that a multiferroic E-AFM order emerges in $EuMnO_3$ thin film that is not obtained from the bulk materials under pressure.

5.1 Introduction

In the previous chapter, we have demonstrated an insulator-AFM to metal-FM phase transition in $EuMnO_3$ induced by pressure from our first-principles calculations. This is an unprecedented phenomenon in multiferroic rare-earth manganites that establishes a link between these systems and colossal magnetoresistance compounds. Additionally at high pressure, we found a new phase, E*-AFM order, becoming quasi-degenerate with FM ground state. Such a E*-AFM order can be regarded as a ferroelectric-like metal, which drive a coexistence of non-centrosymmetric ionic crystal structure and half metallic electronic band structure. Polar metal is a very rare state, only being identified in several specific systems [114, 116].

These findings represent an unexpected addition to what is known in the model-case system $TbMnO_3$. In this case, $TbMnO_3$ undergoes a spin-spiral to E-AFM phase transition under hydrostatic pressure at around 3.6 GPa, which implies a significant increase of the polarization together with its reorientation from the c-axis to the a one [22, 117].

One way to further exploit all these possibilities is by means of epitaxial strain. In fact, several intriguing phenomena have recently been found by following this strategy. These include multiferroicity in AMnO$_3$ systems [118, 119], insulator-metal transitions in rare-earth nickelates thin films [120, 121] and novel polar metal states by e.g experimentally geometric design [114, 116]. In $TbMnO_3$ in particular, it has been confirmed that (001)-oriented $TbMnO_3$ thin film on $SrTiO_3$ substrate display a weak ferromagnetism within E-AFM order [122, 123], while (010)-oriented film on $YAlO_3$ substrate is stabilised in a E-AFM state [124].

In this chapter, we make a comparative study of the effect of the epitaxial strain on the properties of $TbMnO_3$ and $EuMnO_3$ by means of first-principles calculations. Specifically, we obtain the phase diagram for these compounds as a function of strain. Thus, we find several transitions between different ground states that include the transition to the polar metallic state. In addition, we compute the electric and magnetic properties of these compounds as a function of strain and for different orientations with respect to the substrate.

5.2 Methods

5.2.1 DFT calculations

Our density functional theory (DFT) based calculations are performed with projected augmented waves (PAW) potentials as implemented in the VASP code [98, 99]. We use the generalized gradient approximation (GGA) PBEsol [100] exchange correlation functional and apply an on-site Coulomb correction for the Mn-3d states following the DFT+U scheme [57]. The Eu-4f and Tb-4f electrons are treated as core electrons and relativistic spin-orbit-interaction (SOI) effects for Tb, Eu and Mn are excluded. We consider the most relevant Mn-spin collinear orders found in manganites: collinear magnetic order – ferromagnet (FM), A-, E_a-, E^*_a-, E_b- and E^*_b-AFM and noncollinear order – spin spiral states [see Sec. 1.2]. Here E- and E*-AFM correspond to the same E-type in-plane Mn spin ordering but with AFM and FM inter-plane coupling respectively. The orthorhombic $Pbnm$ supercell containing two unit cells is employed for all collinear magnetic states. Specifically, FM and A-AFM states are built in $1 \times 2 \times 1$ supercell. As for E-AFM orders, the subscript notation "a" ("b") indicates that the supercell is constructed by doubling the unit cell along $a(b)$-direction. The noncollinear spiral state is a cycloidal spin wave

with commensurate wave vector $k = 1/3$ along b-axis, built in a $1 \times 3 \times 1$ supercell. We use $6 \times 3 \times 4$ ($3 \times 6 \times 4$) Monkhorst-Pack k-points grid for $1 \times 2 \times 1$ ($2 \times 1 \times 1$) supercell and $4 \times 2 \times 3$ k-points grid in $1 \times 3 \times 1$ supercell. The cutoff energy for plane waves is set to be 500 eV. We use different U values for the different compounds. Specifically $U_{eff} = 0$ eV for Mn-3d states of $TbMnO_3$ [22], and $U_{eff} = 1$ eV for Mn-3d states of $EuMnO_3$. The choice of these values was studied in detail in the previous chapter [see Sec. 4.4.1.1].

5.2.2 Implementation of epitaxial strain

We will consider thin films subjected to in-plane biaxial strain grown on either (010) or (001)-oriented substrates.

In Figure 5.1(a), we illustrate the (010)-oriented case. Here the underlying orthorhombic substrate is indicated by the grey rectangles. The "freestanding" lattice is represented by dashed lines and, for the sake of simplicity, only the manganese atoms are shown. We consider the perovskite $YAlO_3$ as the substrate material and define the epitaxial strain as $\eta = (a - a_s)/a_s = (c - c_s)/c_s$, where a_s and c_s represent the experimental in-plane lattice parameters of $YAlO_3$. Consequently, we assume that the relative change of the lattice parameters a and c is the same. Note that, for zero strain, the $TbMnO_3$ and $EuMnO_3$ films already experience a compression with respect to the freestanding case. Specifically, the compression is 2.1% and 3.1% along a-axis, 0.4% and 1.1% along the c-axis respectively.

For the (001)-oriented case, we consider a cubic substrate as shown in Figure 5.1(b). Thus, we define the epitaxial strain as $\eta = (a - a_s)/a_s = (b - b_s)/b_s$, where we assume that the in-plane lattice parameter a_s and b_s of the substrate (in solid line) is the average of that of the "freestanding" lattice a_0 and b_0 (in dashed line), *i.e.* $a_s = b_s = (a_0 + b_0)/2$. Thus, we change the lattice by keeping the $a = b$. Correspondingly, the freestanding lattice has been already stretched along a-axis and compressed along b-axis at zero strain.

In both cases, for every given value of the in-plane lattice parameters (*i.e.* the strain), we relax both the out-of-plane lattice parameter and the internal atom positions by imposing different magnetic orders.

5.3 Results

5.3.1 $TbMnO_3$

5.3.1.1 (010)-oriented films

In Fig. 5.2, we show the total energy, polarization and band gap of (010)-oriented $TbMnO_3$ thin film as a function of epitaxial strain (from -6% to 6%) . As we can see in Fig. 5.2(a), the energy is essentially a quadratic function of the strain. However, the minimum of

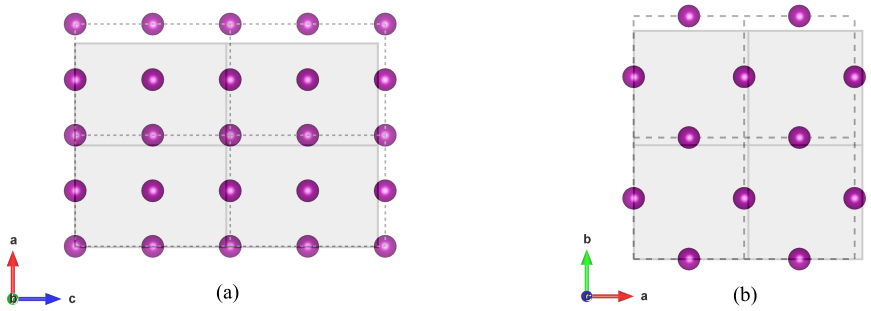

Figure 5.1: Schematic diagram of (a)(010) and (b) (001)-oriented thin films, the lattices of substrate and thin film are plotted with solid and dashed lines respectively.

Optimization procedure	E_b-AFM	FM	A-AFM	SPIRAL
Fix lp to freestanding lattice	0	27.62	5.87	**-0.81**
Fix in-plane lp to zero strain	**0**	40.93	23.48	41.53

Table 5.1: Total energy (unit: meV/f.u.) of FM, A-AFM and spiral state with respect to E_b-AFM magnetic orders calculated in two optimization methods. First, relax the internal atomic positions by fixing the lp to experimental values (freestanding lattice) and imposing A-AFM; Second, optimise the structure by fixing in-plane lp to zero strain and imposing A-AFM spin orders. **lp – lattice parameter.

the parabola is different for the different magnetic orders. This difference is highlighted in Fig. 5.2(b), where we plot the energy of these orders with respect to the reference E_b-AFM state. In this way we can clearly see the phase competitions and transitions that are induced by means of epitaxial strain. Specifically, the ground state of the system transforms according to the sequence:

$$E_b\text{-AFM} \overset{1\%}{\longleftrightarrow} E_b^*\text{-AFM} \overset{3\%}{\longleftrightarrow} \text{A-AFM}.$$

As we discussed in the previous chapter, the energy of the spiral state is very sensitive to the method of structural relaxation (see Sec. 4.4.1.2). However, the spiral state cannot be stabilised irrespective of the relaxation method. Specifically, we performed a comparative study of the energy of two different optimization procedures by taking the E_b-AFM as the reference state. The results are shown in table 5.1. If the lattice parameters are fixed at the values of freestanding bulk materials and the internal positions are optimised by imposing A-type antiferromagnetic order, then 60° spiral state is obtained to be the ground state [see Sec. 4.4.1.2]. However, as soon as we impose the epitaxial strain and the in-plane lattice parameters to those of $YAlO_3$ substrate, the ground state becomes the E_b-AFM order. The energies of the spiral state shown in Fig. 5.2(a) correspond to this second method.

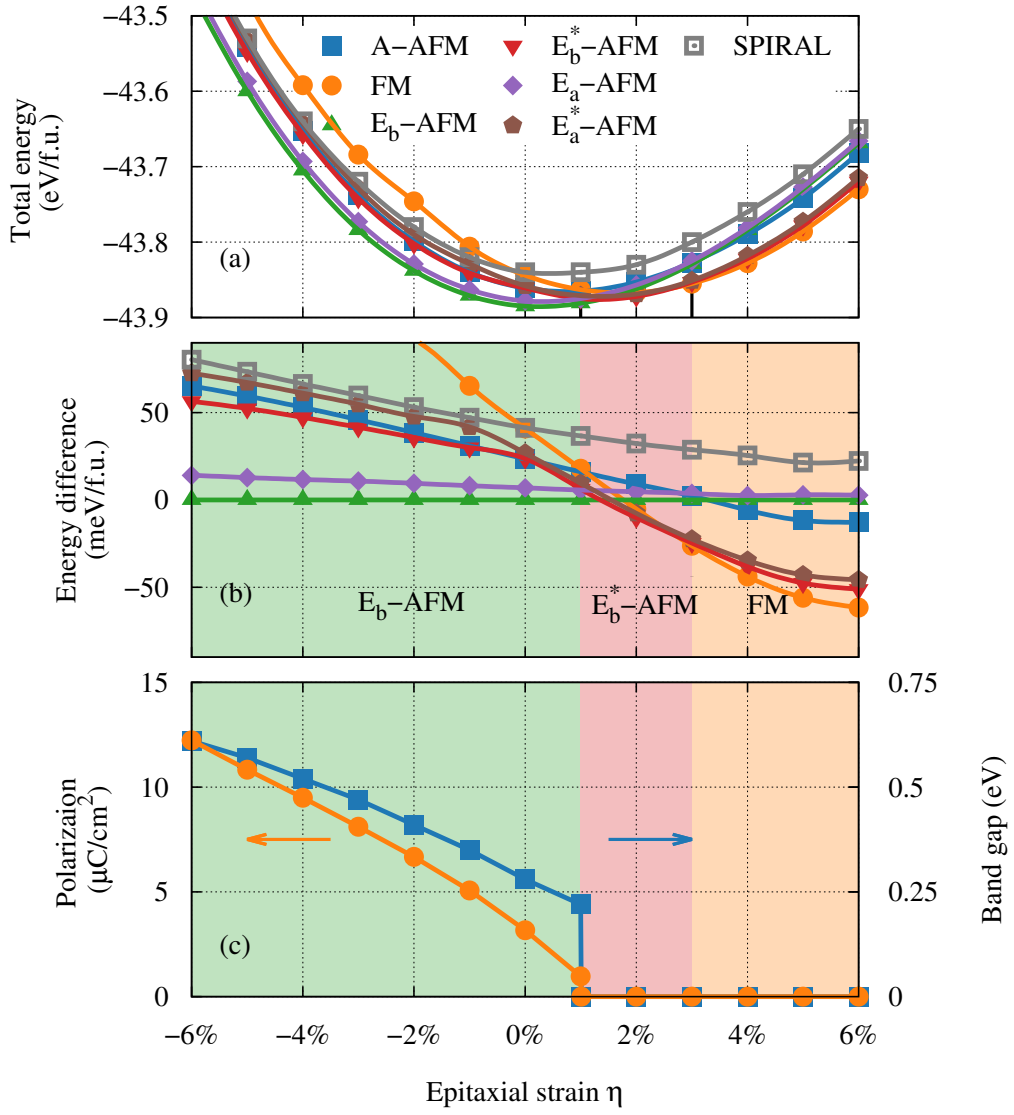

Figure 5.2: The total and relative energy, polarization and band gap as a function of epitaxial strain of (010)-oriented $TbMnO_3$ thin film.

In Fig. 5.2(c), we show the polarization and band gap as a function of epitaxial strain. When the strain is between -6% and 1%, both the polarization and the band gap decrease almost linearly by increasing the strain. Then both these quantities drop to zero. Specifically, there is a jump in the polarization of 0.97 $\mu C/cm^2$, and in the band gap of 0.22 eV. This represents a first-order transition induced by the transformation of the magnetic ground state from a E-AFM order to FM one.

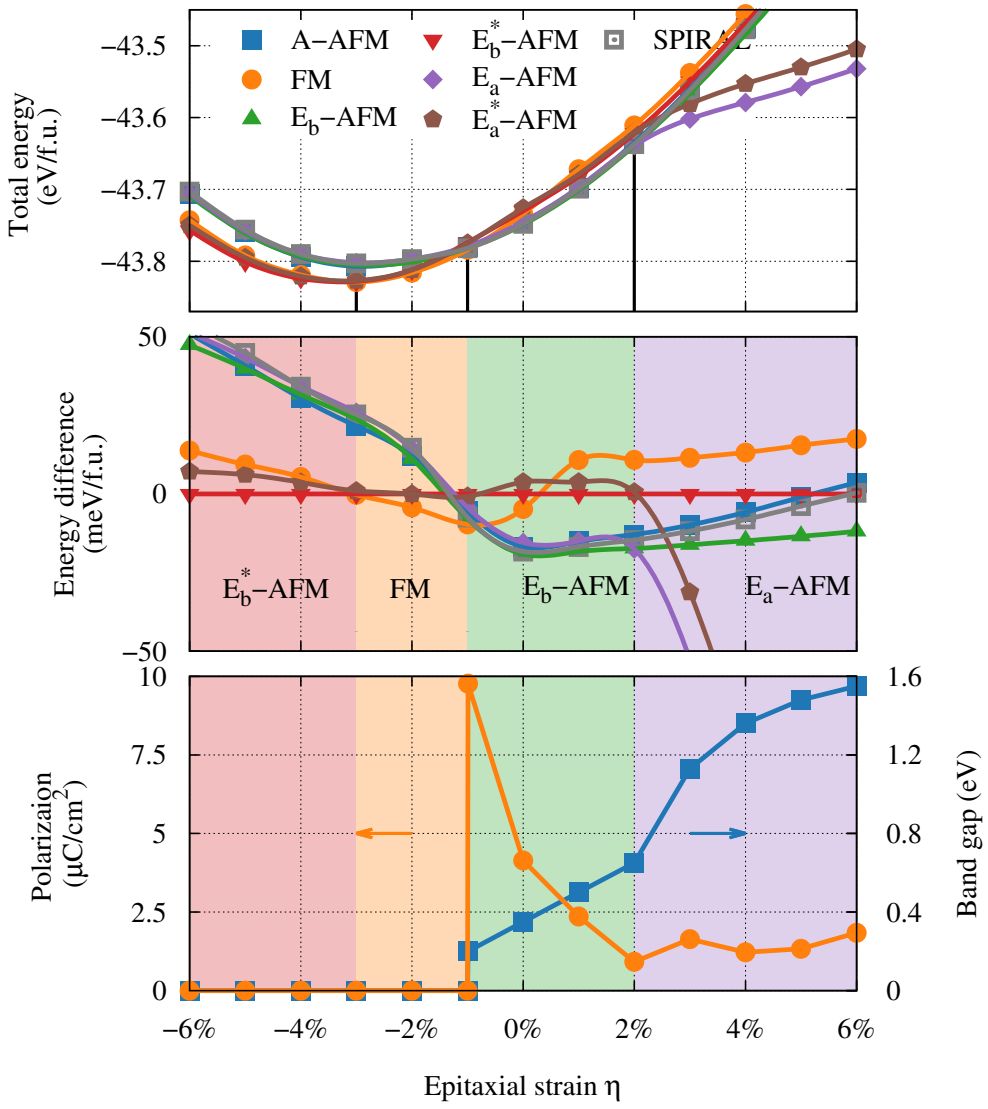

Figure 5.3: The total and relative energy, polarization and band gap as a function of epitaxial strain of (001)-oriented $TbMnO_3$ thin film.

5.3.1.2 (001)-oriented films

In Fig. 5.3, we show the total and relative energies (the E_b^*-AFM is now taken as reference state) as a function of the epitaxial strain for (001)-oriented $TbMnO_3$ thin films, together with the electric polarization and band gap of the corresponding ground state. In this case we obtain a different sequence of phase transitions:

$$E_b^*\text{-AFM} \overset{-3\%}{\longleftrightarrow} \text{FM} \overset{-1\%}{\longleftrightarrow} E_b\text{-AFM} \overset{2\%}{\longleftrightarrow} E_a\text{-AFM}$$

We note that the total energy of the E_a-AFM and E_a^*-AFM states is not exactly parabolic as for the other states. Specifically, when the strain exceeds 2%, the dependence on the strain for these two states change from parabolic to linear. We also note that in the strain range between -1% and 2%, the spiral state is only slightly higher in energy ($\sim$ 2 meV/f.u.) compared to the E_b-AFM ground state.

As we can see in Figure 5.3(c), both the electric polarization and the band gap are zero if the strain is between -6% and -1%. At $\eta = -1\%$, the polarization jumps to 9.8 μC/cm^2. This is followed by a quick decrease to 1 μC/cm^2 at $\eta = 2\%$, from which it stays practically constant ($\sim 2\mu$C/cm^2) up to $\eta = 6\%$. The band gap, in its turn, opens abruptly at $\eta = -1\%$ where it becomes $\sim$ 0.20 eV. Then, it increases and takes the value 1.55 eV at $\eta = 6\%$. Similar to the (001)-oriented case, we obtain a first-order phase transition driven by the magnetic order reorientation from a E-AFM order to FM one.

5.3.2 $EuMnO_3$

5.3.2.1 (010)-oriented films

In Fig. 5.4, we show the total and relative energy (take E_b-AFM order as reference state), as well as the polarization and the band gap of (010)-oriented $EuMnO_3$ thin film as a function of epitaxial strain, following the same procedure as $TbMnO_3$ films. From Fig. 5.4(a) and (b), we obtain the following sequence of ground states in this system:

$$E_b\text{-AFM} \overset{0.5\%}{\longleftrightarrow} \text{A-AFM} \overset{1\%}{\longleftrightarrow} \text{FM}.$$

In this case, we find the A-AFM ground state in a narrow range of strain ($\sim 0.5\%$) between E_b-AFM and FM state. This is in contrast to the (010)-oriented $TbMnO_3$, where we find the E^*-AFM state instead. As we can see in Fig. 5.4(c), by increasing the strain, the polarization and the band gap also decrease linearly in this system. However, they vanish at different strains. Specifically, we find the critical strain $\eta_c = 0.5\%$ for the polarization and $\eta_c = 1.0\%$ for the band gap. Above these strains, both of these quantities are zero. We then have two first-order phase transitions, that originate from two different magnetic order reorientations: E_b-AFM $\rightarrow$ A-AFM and A-AFM $\rightarrow$ FM respectively.

5.3.2.2 (001)-oriented films

In Fig. 5.5(a) and (b) we show total and relative energy (take FM state as reference) as a function of strain in (001)-oriented $EuMnO_3$ thin films. In this case, we obtain three different ground states according to the sequence:

$$\text{FM} \overset{-0.5\%}{\longleftrightarrow} \text{A-AFM} \overset{3\%}{\longleftrightarrow} E_a\text{-AFM}.$$

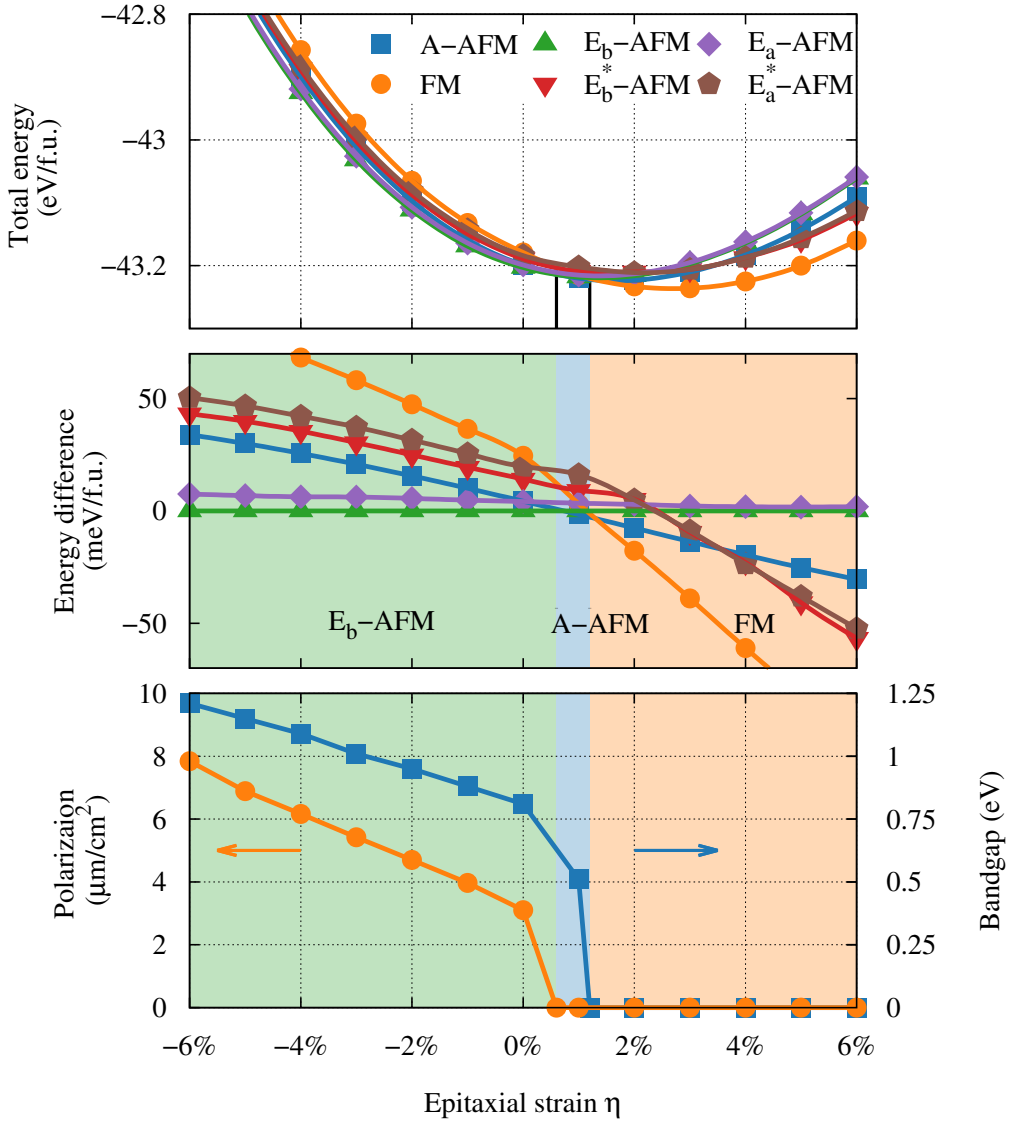

Figure 5.4: The total and relative energy, polarization and band gap as a function of epitaxial strain of (010)-oriented $EuMnO_3$ thin film.

The A-AFM order is now stable in a larger range of strain compared with the (010)-oriented case. Similar to (001)-oriented $TbMnO_3$ film, the dependence on the strain of the energy of E_a-AFM and E_a^*-AFM states change from parabolic to linear when the strain exceeds 3%. From Fig. 5.5(c) we see that the electric polarization and the band gap display a similar behavior in the sense that they emerge abruptly from zero and increase by increasing the strain. The critical strains, however, are different: $\eta_c = 3\%$ and $\eta_c = -0.5\%$ for the polarization and the band gap respectively. These strains are again

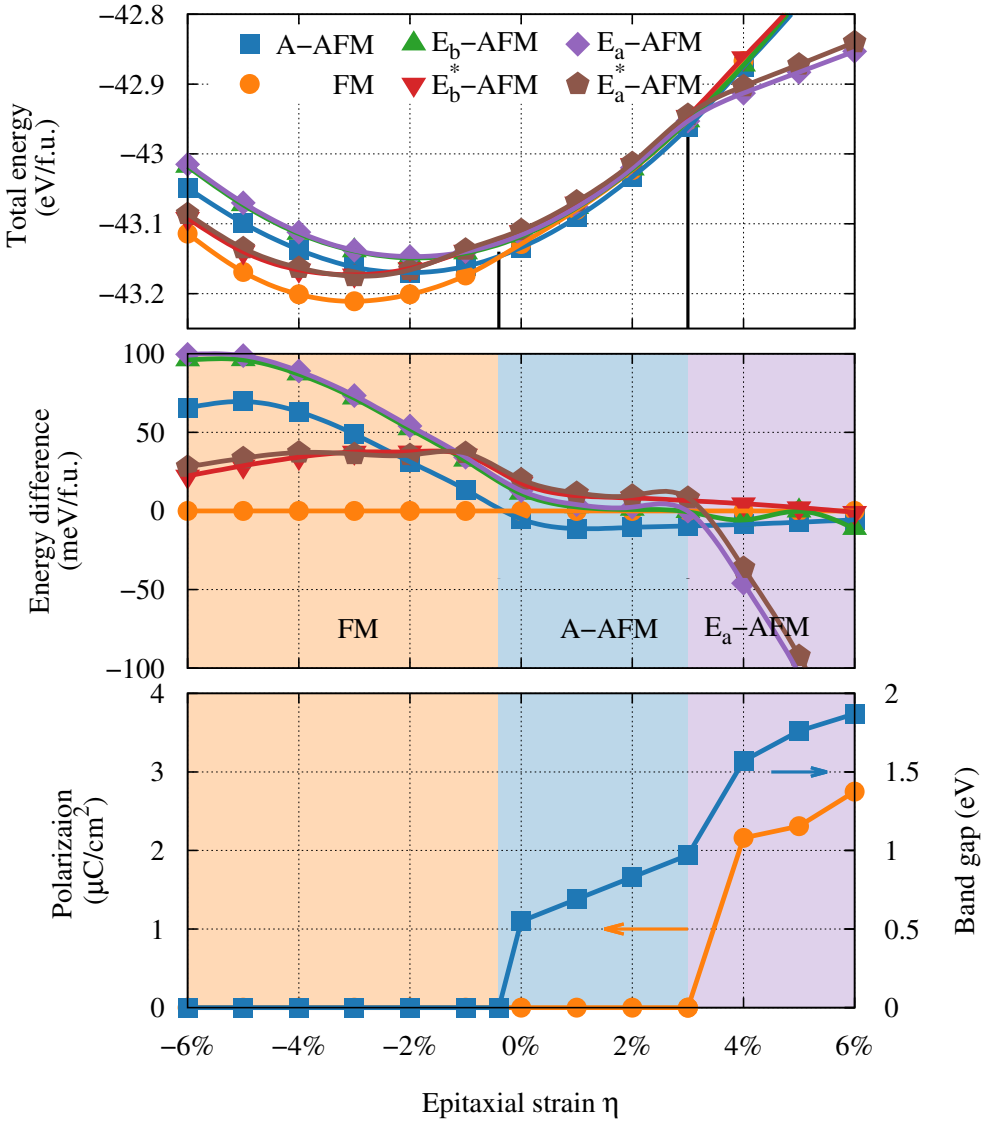

Figure 5.5: The total and relative energy, polarization and band gap as a function of epitaxial strain of (001)-oriented $EuMnO_3$ thin film.

associated to two separated first-order transitions, which in this case correspond to FM

→ A-AFM and A-AFM → E_a-AFM.

(a) (010)-oriented $TbMnO_3$

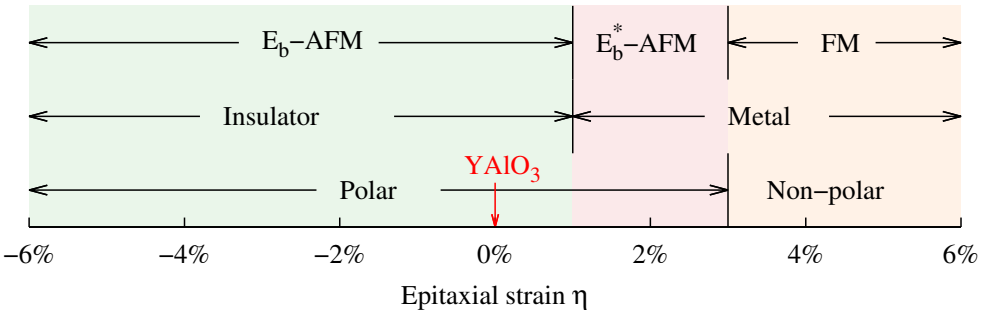

(b) (001)-oriented $TbMnO_3$

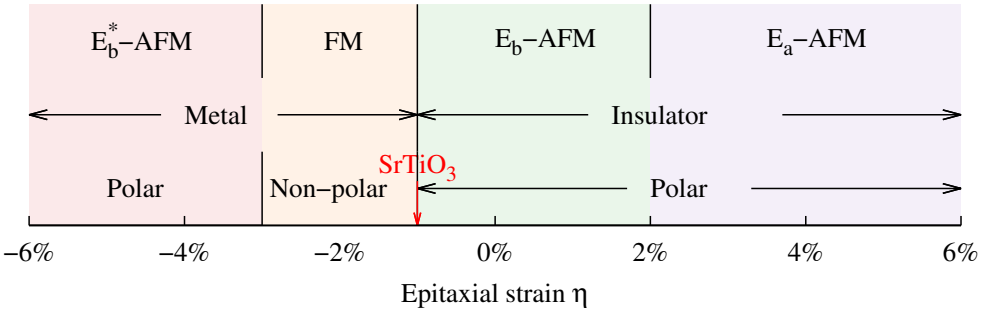

(c) (010) oriented $EuMnO_3$

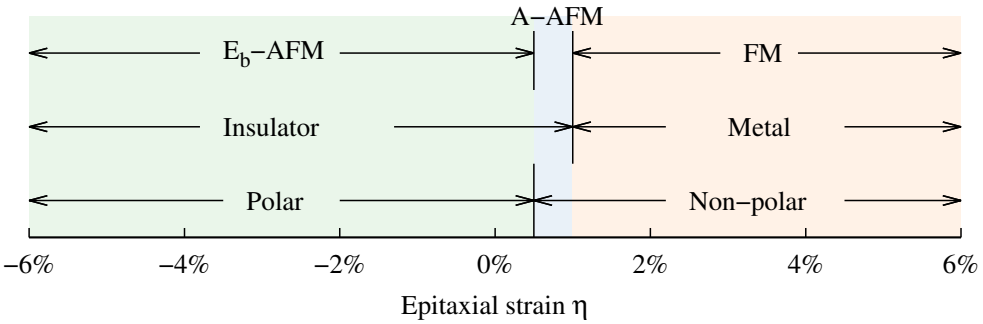

(d) (001) oriented $EuMnO_3$

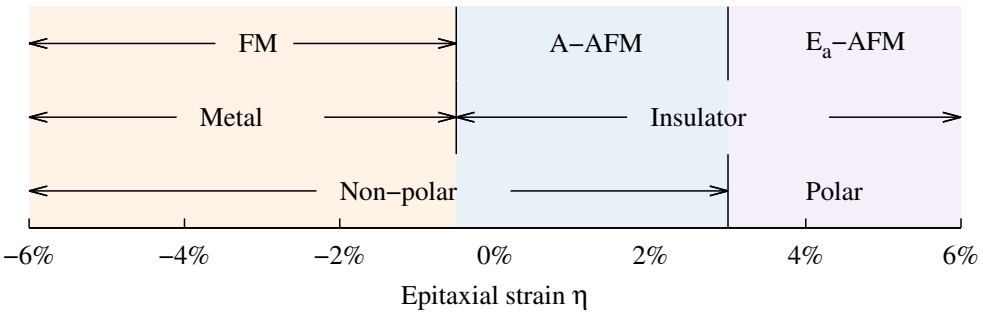

Figure 5.6: Magnetic and electric phase diagram of (a) the (010)-oriented and (b) the (001)-oriented $TbMnO_3$ thin film as well as (c) the (010)-oriented and (d) the (001)-oriented $EuMnO_3$ thin film.

5.4 Discussion

5.4.1 Predicted phase diagrams and comparison with experiments

In Figure 5.6 we show the overall magnetic and electric phase diagrams of $TbMnO_3$ and $EuMnO_3$ thin films summarising the above results. In these figures, we first indicate on the top the magnetic ground state with respect to the epitaxial strain. And then, below, we show the corresponding spin-driven electric phase transitions, *e.g.* insulator – metal transition and polar – non-polar phase transition. For the (010)-oriented $TbMnO_3$, we predict a magnetic phase transition accompanied with the spin-driven insulator – metal and polar – non-polar transitions [see Fig. 5.6(a)]. As discussed in Sec. 5.2.2, zero strain in this case corresponds to a film grown on the (010)-oriented $YAlO_3$ substrate. At this specific point, we find the E_b-AFM ferroelectric insulator state as the ground state of the system. This is totally consistent with the experimental results recently reported [23], where the authors have successfully grown $TbMnO_3$ film on the (010)-oriented $YAlO_3$ substrate and confirmed that the multiferroic E-AFM state is stabilised as the ground state. Furthermore, the polarization obtained from our calculations (3.2 $\mu C/cm^2$) is in a very good agreement with the experimental value (0.6 – 2 $\mu C/cm^2$) measured along the a direction.

More interestingly, we predict that the E_b^*-AFM order will be stabilised as the ground state in the strain range of 1% – 3%. The symmetry of the lattice resulting from this magnetic structure is reduced to the $Pmn2_1$ space group. We then have a non-centrosymmetric distortion of the original lattice due to the emergence of this particular order. At the same time, the density of states (DOS) obtained from our calculations reveals that this state is a metal Such an epitaxial-strain-induced E_b^*-AFM state then represents an intriguing realization of a polar metal [111, 112, 113, 114, 115], with coexisting both non-centrosymmetric crystal structure and half-metallic electronic properties. It is worth noting that we have already observed the tendency towards this state when the bulk $EuMnO_3$ is subjected to hydrostatic pressure. As we see, this tendency can eventually be materialised by means of epitaxial-strain in $TbMnO_3$. This is one of important results of this thesis work.

In the case of the (001)-oriented $TbMnO_3$ films we also obtain magnetically driven metal – insulator and polar – non-polar – polar transitions [see Fig. 5.6(b)]. In addition, our phase diagram explain the experimental observations reported in [123]. Here, the E-AFM state is reported together with weak ferromagnetism for a thin film grown on (001)-oriented $SrTiO_3$ cubic substrate. In this case, the film is subjected to a strain equivalent to $\eta = -1\%$ in our phase diagram as indicated by the red arrow in Fig. 5.6(b). This amount of strain locates exactly at the phase boundary between E_b-AFM and FM

state. Since this transition is expected to be a first-order transition, then the coexistance between the corresponding orders can naturally happen at this point.

We also obtain the non-centrosymmetric metallic E_b^*-AFM state for this orientation in $TbMnO_3$. This state is now stabilized for relative large compressive strains (below -3%). Then, there is a similar polar to non-polar transition associated to the transformation of the ground state from E_b^*-AFM to FM order in which the system stays metallic. Next, the subsequent transition in this case corresponds to a metal – insulator transition and non-polar – polar phase transition that take place simultaneously at the same critical strain $\eta_c = -1\%$. This is due to the stabilization of the E_b-AFM order at low levels of strain. Finally, at $\eta = 2\%$, there is an additional transition from E_b-AFM to E_a-AFM order. Even if both of these states are polar, the electric polarization changes from the a-axis to the b-axis and its magnitude becomes nearly constant as a function of strain [see Fig. 5.3].

In Fig. 5.6(c) and (d) we show the overall phase diagrams of strained $EuMnO_3$ films. The main difference compared to $TbMnO_3$ is the absence of polar metallic states, even if some tendency towards these state can be induced by means of hydrostatic pressure in bulk samples. At the same time, the A-AFM order can be stabilised in this system which is not the case for $TbMnO_3$. This A-AFM order corresponds in fact to the ground state of bulk $EuMnO_3$ [92, 125]. It survives in the range of strain from 0.5% to 1% in (010)-oriented film and from -0.5% to 3% in (001)-oriented ones. We note also that, because of the stabilization of such a A-AFM order, the insulator – metal transition and polar – non-polar transition occur separately at different critical strains.

It is worth noting that, by means of epitaxial strain, we essentially obtain the same insulating A-AFM to metallic FM phase transition obtained in the previous chapter by means of hydrostatic pressure in bulk samples. Specifically, we can achieve the transition by increasing tensile strain in (010)-oriented film or increasing compressive strain in (001)-oriented one. Additionally, we predict a multiferroic E_b-AFM phase in (010)-oriented $EuMnO_3$ (-6% – 0.5%) and a multiferroic E_a-AFM in (010)-oriented $EuMnO_3$ (3% – 6%). These latter results are totally new compared with our previous study on hydrostatic pressure.

5.5 Conclusions

In conclusion, we have presented a comparative study between $TbMnO_3$ and $EuMnO_3$ epitaxial thin films by means of first principles calculations. We have obtained the phase diagram as a function of epitaxial strain for two experimentally relevant orientations of these films, namely, the (010) and (001) orientations. And we show that epitaxial strain allows a richer phase diagram in these systems. Our results confirm the findings of recent

experiments carried out in $TbMnO_3$ films grown on $YAlO_3$ and $SrTiO_3$ substrates. In addition, we predict novel magnetically-induced insulator – metal and polar – non-polar transitions. More specifically, we find that both the multiferroic E-AFM order and the polar metallic E*-AFM state are stabilized in $TbMnO_3$ by means of expitaxial strain. For $EuMnO_3$, we predict a multiferroic E-AFM state that is not obtained from our previous study by hydrostatic pressure. We expect our results will encourage further experimental and theoretical investigations on the rare-earth manganites.

6

Conclusions

In this thesis, we have presented a theoretical study of various ferroic instabilities. We considered two particular cases: i) the ferroelectric instability in novel confined geometries and ii) magnetic instabilities controlled by the distortion of the underlying crystal lattice.

The first two Chapters were aimed at providing the relevant background for the main content of this thesis. In Chapter 1, we gave a brief introduction to ferroelectricity from the phenomenological point of view and introduced a more microscopic description of the different magnetic orders that appear in the particular case of the rare-earth manganites. In Chapter 2, we described the first-principles calculations based on the DFT framework, mainly on the associated tools to extract physical properties in condensed mater simulations.

After these two introductory chapters, in Chapter 3 we considered in detail the ferroelectric instability in confined structures, specifically, the nanotubes and the spherical nanoshells and developed a phenomenological theory for describing such an instability. We determined, in particular, how the emergence of polarization is affected by the thickness of the nanoparticle, the dielectric properties of the surrounding media and the interfacial boundary conditions. We found an intriguing topological finite-size effect that can promote an unexpected competition between two different types of distribution of polarization – irrotational and vortex-like – in the ultra-thin limit. Our work represents the first semi-analytical study of the ferroelectric instability in these particular geometries, which has the potential to be applied in new nano devices. However, it is an inaugural study in which a number of likely important factors such as the polarization anisotropy and the strain fields have been ignored. Also, we did not consider a specific ferroelectric material, but just determined the qualitative trends in the problem. All these limitations need to be overcame in future developments. Even though, we have presented a global picture that captures the main physics of the problem and our results suggest new routes to control

the ferroelectric instability and engineer ferroelectric properties at the nanoscale. This is expected to motivate and guide future experiments.

In Chapters 4 and 5 we employed a different formalism to investigate the structural, electronic and magnetic properties of the rare-earth manganites. Specifically, we conducted a theoretical investigation from first-principles calculations. In Chapter 4 we focused on $EuMnO_3$ under hydrostatic pressure. The main finding of this investigation is the prediction of a pressure-induced A-AFM insulator to FM metal transition that is unprecedented in the multiferroic rare-earth manganites $RMnO_3$. This transition displays a strong interplay with Jahn-Teller distortions similar to the one observed in $LaMnO_3$. We thus established an interesting link between colossal-magnetoresistance and multiferroic manganites via the $EuMnO_3$ compound. This investigation was extended in Chapter 5 to the study to the epitaxial strain effects on both $EuMnO_3$ and $TbMnO_3$ thin films. We thus determined the magnetic phase diagram as a function of epitaxial strain for two experimentally relevant orientations of these films, namely, the (010) and (001) orientations. We showed that epitaxial strain generates a much richer phase diagram compared to hydrostatic pressure. Our results are fully consistent with the findings of recent experiments carried out in $TbMnO_3$ films grown on $YAlO_3$ and $SrTiO_3$ substrates. In addition, we predicted novel magnetically-induced insulator – metal and polar – non-polar transitions. More specifically, we found that both the multiferroic E-AFM order and the polar metallic E*-AFM state are stabilized in $TbMnO_3$ by means of epitaxial strain. On the other hand, we found a novel epitaxial-strain-induced multiferroic E-AFM state in $EuMnO_3$ that cannot be obtained by means of just hydrostatic pressure.

When it comes to future investigations, it will be particularly interesting to clarify further the link between the two families of compounds, *i.e.* colossal-magnetoresistance and multiferroic manganites, that we have revealed during this thesis. Our results also indicate that $TbMnO_3$ thin film hosts a potential realization of a new type of (magnetically-induced) ferroelectric metal. This can add an extra dimension to the thought-provoking question of ferroelectricity emerging in metals and hence can become a reference model-case for future studies. In principle, our study can be straightforwardly extended to the ferroic instabilities to the whole series of rare-earth manganites. In addition of determining the general phase diagram of these systems, novel fundamental properties and extra multifunctionalities can be discovered in such a study. We truly hope that the results of present PhD thesis will intrigue more research activities in the field of ferroics.

Appendix A

Rare-earth Ferrites

A.1 Introduction to rare-earth ferrites

In this appendix, we discuss another important series of oxides, the orthorhombic $R\mathrm{FeO}_3$. The main character of this series is, in contrast to $R\mathrm{MnO}_3$, displaying a non-collinear magnetic orders with weak canting on both R and Fe ions.

The spin canted order is described by the combinations of the collinear orders from different directions. Considering the spatial anisotropy, there are totally 3×4 basis: $F_x, F_y, F_z, A_x, A_y, A_z, C_x, C_y, C_z, G_x, G_y, G_z$. A common notation to describe the complex magnetic canted structure of perovskites is the so-called Bertaut's notation [126]. In this notation, the magnetic structure can be labelled as $A_xB_yC_z$, where A, B, C represent different types of order, and x, y, z are the directions. For example, suppose we have a simple G-type structure in which the spins are aligned along x direction, it is labelled as G_x in Bertaut's notation, see Figure A.1(a). If this order displays an additional A-type component along y direction, we then have G_xA_y configuration as shown in Fig. A.1(b). Further if there is an extra F-type component along z axis, then the overall structure is denoted as $G_xA_yF_z$ (see Fig. A.1(c)). This is the case in most of the perovskites with the $Pbnm$ structure [90, 127]. The Bertaut's notation is convenient for describing spin orders on both A-site and B-site atoms in perovskites [128].

In Figure A.2, we show the main magnetic phase diagram of the orthorhombic $R\mathrm{FeO}_3$ (R represents the rare-earth element) [90]. As shown in Fig. A.2, the whole series has a relatively high Néel temperature of the Fe ions, which are above 600 K. Below this transition temperature, the initial magnetic order of the Fe ion is stabilized as $\mathbf{G}_xA_yF_z$ for every compound. As the temperature decreases, in the compounds with R = La, Eu, Gd and Lu, the $\mathbf{G}_xA_yF_z$ order persists to very low temperature. While in some other cases with R = Pr, Nd, Sm, Tb, Ho, Er and Yb, a spin reorientation takes place continuously from $\mathbf{G}_xA_yF_z$ to $F_xC_y\mathbf{G}_z$, which results from the continuous rotation of the

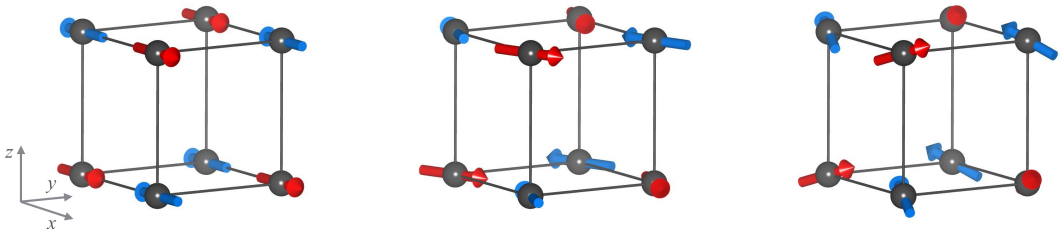

(a) $\mathbf{G}_x$ (b) $\mathbf{G}_x\mathrm{A}_y$ (c) $\mathbf{G}_x\mathrm{A}_y\mathrm{F}_z$

Figure A.1: Non-collinear spin-canted order

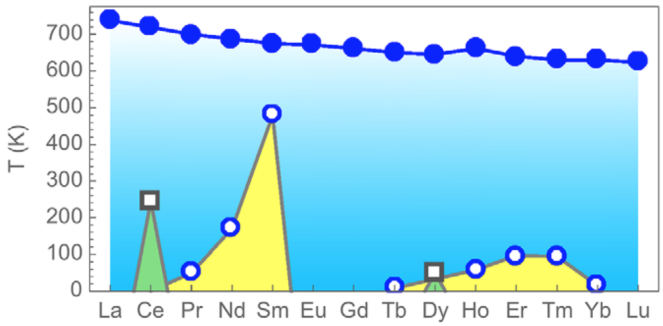

Figure A.2: Néel and spin-reorientation temperatures for the Fe spin order in $R\mathrm{FeO}_3$ perovskites. Filled circles, open circles and squares indicate the establishment of spin order $\mathbf{G}_xA_yF_z$, $F_xC_y\mathbf{G}_z$ and $A_x\mathbf{G}_yC_z$ respectively.

easy axis from x to z-axis. The reorientation temperature varies from $\sim$ 500 K to several K ($<$ 10 K). There are two special cases $R\mathrm{FeO}_3$ (R = Ce, Dy), in which the magnetic order abruptly transforms from $\mathbf{G}_xA_yF_z$ to $A_x\mathbf{G}_yC_z$. In this case, the easy axis turns from x to y discontinuously. At very low temperature ($<$ 10 K) regimes, the magnetic ordering starts to appear on the R ion, it can be collinear and non-collinear.

The spin reorientations suggest that the interplay between the R and the Fe spins is already strong at a relative high temperature, which is much higher than the ordering temperature of the rare-earth. The total magnetization of some systems reduces and reverses by decreasing the temperature [129, 130, 131]. The temperature at which the magnetization vanishes is T_{comp}, which is 7.6 K, 3.9 K and 46 K for Nd, Sm and Er respectively. Such a temperature-induced magnetization reversal has been attributed to the gradual magnetization of the R-sublattice in opposite direction to the Fe-wFM component. This unusual mechanism was proposed by Yamaguchi to originate from an effective exchange field between Fe and R spins and resulting from a competition between the Fe-Fe, R-Fe and R-R interactions [128]. Since this exchange field is negative, R and Fe spins are antiparallel, which is in agreement with the experimental observations. This series provides a good example of spin-induced ferroelectricity generated by two magnetic species via

symmetric magnetostriction, as we have discussed in Sec. 1.3.6.

In this series, $GdFeO_3$ is one of the most important examples due to its huge non-linear magnetoelectric response [132]. The spin order of Fe in $GdFeO_3$ transforms into $\mathbf{G}_x A_y F_z$ at 661 K, where the weak FM canting along z direction is due to DM interaction. The Fe spins do not reorient any more as the temperature decrease. However, the Gd spins develop an additional $G_x A_y$ order at a very low temperature $T_{Gd} = 2.5$ K[132]. From the point-group symmetry analysis of representative orders in orthorhombic perovskites, the resulting magnetism, breaks both time reversal and space inversion symmetries [see Table 1 in reference [90]]. The measured magnetization is about 0.37 μ_B/f.u. and the electric polarization is around 0.12 μC/cm^2 at 2 K [132] which is relatively large compared to the other spin-induced ferroelectrics. The electric polarization is extremely sensitive to an external magnetic field and decreases nonlinearly irrespective of the direction of the field, making $GdFeO_3$ a strong magnetoelectric crystal. Beyond a critical magnetic field, the polarization is completely suppressed due to the reorientation of both Fe and Gd spins to configurations not promoting the electric polarization.

In this appendix, we perform the first-principles calculations on magnetic interactions in the orthorhombic $GdFeO_3$. We extract the interaction parameters J's between rare-earth and Fe lattices. With these parameter, we investigate the temperature dependence of magnetization by the spin-dynamics approach.

A.2 Methods

A.2.1 First-principles calculations

We perform the first principles calculations here by following the similar procedure and settings on the manganites [see Sec. 4.2]. However, here we use a $Pbnm$ unit cell of $GdFeO_3$. We consider the magnetic moment on both Gd and Fe ions, by initiating it as $7\mu_B$ for Gd and $5\mu_B$ for Fe. The on-site Coulomb correction are applied for both Gd-4f and Fe-3d states through DFT+U scheme.

A.2.2 Spin Dynamics

To describe the equilibrium properties of the spins in $GdFeO_3$, we use the Landau-Lifshitz-Gilbert equation [133]:

$$\frac{d\mathbf{S}_i}{dt} = -\frac{\gamma_i}{(1+\lambda_i^2)\mu_i}\mathbf{S}_i \times [\mathbf{H}_i + \lambda_i \mathbf{S}_i \times \mathbf{H}_i], \tag{A.1}$$

where λ_i is the coupling to the *magnon* thermal bath which governs return to FM equilibrium. In the high damping limit equilibrium properties can be obtained by calculating

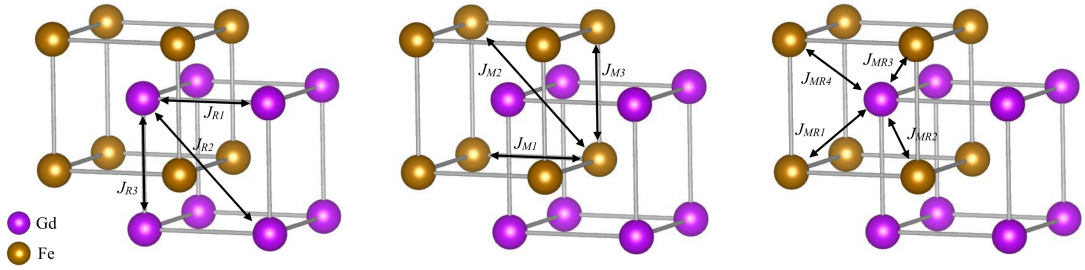

(a) Gd-Gd (b) Fe-Fe (c) Gd-Fe

Figure A.3: Exchange interaction constant J of Gd-Gd, Fe-Fe and Gd-Fe.

thermodynamic averages and is similar in spirit to quenched molecular dynamics The effective fields $\mathbf{H}_i$ at the site i are determined using a Heisenberg Hamiltonian including exchange extended with anisotropy and Zeeman terms:

$$\mathcal{H}_{\text{ASD}} = -\sum_{\langle i,j \rangle} J_{ij} \mathbf{S}_i \cdot \mathbf{S}_j - \sum_i K_i (\mathbf{S}_i \cdot \hat{\mathbf{n}})^2 - \sum_i \mu_i \mathbf{S}_i \cdot \mathbf{B}\,, \tag{A.2}$$

where K_i is a small uniaxial anisotropy constant ($K_i = 10^{-24} J$) and $\hat{\mathbf{n}}$ is the direction of the easy axis taken here to be in the x direction. The final term in Eq. (A.2) is the Zeeman term with the applied magnetic field $\mathbf{B}$. Based on a real space formalism, the magnetic moments μ_i are assumed to be localized on a given atomic site, i, with their time-dependence given by the phenomenological LLG equation. The effective field is given by the derivative of the Hamiltonian with respect to the spin:

$$\mathbf{H}_i = -\frac{\partial \mathcal{H}_{\text{ASD}}}{\partial \mathbf{S}_i} + \boldsymbol{\zeta}_i, \tag{A.3}$$

and includes stochastic thermal fluctuations $\boldsymbol{\zeta}_i$. These are included by incorporating a Langevin thermostat set to the desired magnonic temperature, T. In the present work, the noise process is assumed to be white ($\langle \zeta_i^\alpha(t) \rangle = 0$) because of the time-scale of equilibrium properties, where the heat bath (phonon or electron system) acts much faster than the spin system. The correlator of the process is defined through the fluctuation dissipation theorem as:

$$\langle \zeta_i^\alpha(t) \zeta_j^\beta(t') \rangle = \frac{2\lambda_i k_{\text{B}} T \mu_i}{\gamma_i} \delta_{ij} \delta_{\alpha\beta} \delta(t - t'). \tag{A.4}$$

The α, β represent cartesian (spin) components and i, j represent spatial indices. Full details of the derivation of the correlator can be found in Ref. [134].

A.3 Magnetic interactions

The hamiltonian of the ferrites system can be written as

$$\begin{aligned}\mathcal{H} &= \mathcal{H}_{Gd-Gd} + \mathcal{H}_{Fe-Fe} + \mathcal{H}_{Gd-Fe} \\ &= \sum_{i,j} J_{ij}\mathbf{S}_i \cdot \mathbf{S}_j + \sum_{m,n} J_{mn}\mathbf{S}_m \cdot \mathbf{S}_n + \sum_{i,m} J_{im}\mathbf{S}_i \cdot \mathbf{S}_m \end{aligned} \tag{A.5}$$

which include the interactions of Gd-Gd, Fe-Fe and Gd-Fe. The coupling constants J_{ij}, J_{mn} and J_{im} correspond to the J_{MR}, J_M and J_R in Fig. A.3.

In Figure A.3, we show the interaction between each atoms for our model. In order to determine the parameters J's, we compute the energy associated to the FM, A-, C-, G-AFM spin orders on the irons (for simplicity, we only consider the Fe-Fe interaction first). Each Fe ion is surrounded by 6 nearest neighbors (4 in-plane and 2 out-of-plane neighbors), and 8 next next nearest out-of-plane neighbors (4 in-plane next nearest neighbors are neglected because we use a 20 atom unit cell). In terms of the above Hamiltonian, these energies read:

$$E_{FM} = E_0 + 4J_{M1}S^2 + 8J_{M2}S^2 + 2J_{M3}S^2, \tag{A.6}$$

$$E_{A-AFM} = E_0 + 4J_{M1}S^2 - 8J_{M2}S^2 - 2J_{M3}S^2, \tag{A.7}$$

$$E_{C-AFM} = E_0 - 4J_{M1}S^2 - 8J_{M2}S^2 + 2J_{M3}S^2, \tag{A.8}$$

$$E_{G-AFM} = E_0 - 4J_{M1}S^2 + 8J_{M2}S^2 - 2J_{M3}S^2. \tag{A.9}$$

respectively. Therefore, we simply need to solve a linear equation to obtain the interaction constants J_M's. The Gd-Gd interactions will have the similar expressions. And if we consider the interaction between the spins of Gd and Fe, we can obtain the J_{RM}'s

In Table A.1, we summarize the coupling constant J's and Néel temperature of Fe and Gd obtained by using different U values (U_{Gd} = 1, 3, 5 eV and U_{Fe} = 5 eV). We found the results are not strongly dependent on U. The NN interactions have the relation $J_M > J_{MR} > J_R$, the differences between them are about one order of magnitude. However the NNN interaction between Fe ions, J_{M2}, is smaller than the interaction between Gd and Fe ions, J_{MR}. The Néel temperature of Fe and Gd are estimated by mean field theory in Sec. 4.4.3. We found that T_N^{Fe} is almost three order of magnitude larger than T_N^{Gd}. Compared with the experiments, $T_N^{Fe}(exp)$ = 661 K and $T_N^{Gd}(exp)$ = 2.5 K, our results from mean field theory overestimate T_N^{Fe} but fit well with T_N^{Gd}.

Table A.1: Coupling constant J's and Néel temperature of Fe and Gd obtained by using different U's on Gd (keep $U_{Fe} = 5$ eV).

	$U_{Gd} = 1$eV	$U_{Gd} = 3$eV	$U_{Gd} = 5$eV
$J_M(meV)$	2.6984	2.7239	2.7413
	0.0828	0.0841	0.0851
	2.8827	2.9008	2.9134
$J_R(meV)$	0.0186	0.0104	0.0060
	0.0003	0.0004	0.0010
	0.0134	0.0075	0.0052
$J_{MR}(meV)$	0.1631	0.0985	0.0538
	0.1647	0.1003	0.0558
	0.1055	0.0650	0.0367
	0.1430	0.0855	0.0478
T_N^{Fe} (K)	1101.0561	1108.7145	1113.9602
$T_N^{Gd}(K)$	10.7765	5.7911	3.0382

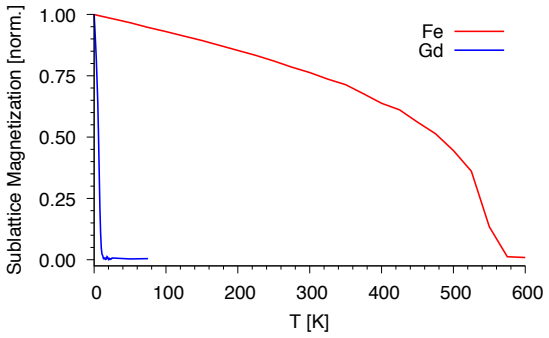

Figure A.4: Atom magnetization as a function of temperature for $GdFeO_3$, magnetization of Fe is labeled by red line, while that of Gd is by blue line.

A.4 Magnetic phase transition

In this section, we use spin dynamic method to simulate the phase transition process. The first step was to determine the Curie temperature by simulating a critical damping regime, $\lambda = 1.0$ to relax the spins. This is done as a function of temperature and at each temperature an equilibration period of 50ps was simulated followed by another 50ps of averaging where the mean and variance of the magnetization (of each spin) was monitored over time until convergence. Generally, convergence is reached at low temperature with convergence taking longer at elevated temperatures as the thermal fluctuations increase. An averaging of 50ps is, in most cases, sufficient to achieve a good magnetization curve.

In Figure A.4, we show the magnetization as a function of temperature for $GdFeO_3$. They agree very well with the experiments, with two phase transitions largely different with each other, with critical temperature of Fe is around 550 K while that of Gd is about

10 K.

A.5 Conclusions

We have preliminarily studied the magnetic interactions in $GdFeO_3$. We map the energy calculated by first principles calculations into Heisenberg model in order to determine the coupling parameters J's for three types of exchange interactions, i.e. Gd-Gd, Fe-Fe and Gd-Fe. With these parameters, we use mean field theory and spin dynamic simulations to investigate the phase transition process. Results from both methods are in a good agreement with the experiments. More work needs to be done in the future, for example, we can include more interactions such as SIA and DM interactions, to determine the easy-plane and non-collinear magnetism, and to study the temperature magnetization reversal mechanism observed in these compounds.

List of Figures

List of Tables

References

[1] Claude Ederer and Nicola A. Spaldin. Recent progress in first-principles studies of magnetoelectric multiferroics. *Current Opinion in Solid State and Materials Science*, 9(3):128 – 139, 2005. 1

[2] Silvia Picozzi and Claude Ederer. First principles studies of multiferroic materials. *Journal of Physics: Condensed Matter*, 21(30):303201, 2009. 1

[3] S. Picozzi and A. Stroppa. Advances in ab-initio theory of multiferroics. *The European Physical Journal B*, 85(7):240, Jul 2012. 1

[4] Richard M Martin. *Electronic structure: basic theory and practical methods*. Cambridge university press, 2004. 1

[5] K.M. Rabe, C.H. Ahn, and J.M. Triscone. *Physics of Ferroelectrics: A Modern Perspective*. Topics in Applied Physics. Springer Berlin Heidelberg, 2007. 1, 3, 43, 45, 98

[6] Valery L Pokrovsky. Landau and modern physics. *Physics-Uspekhi*, 52(11):1169, 2009. 1

[7] J. L. Ribeiro and L. G. Vieira. Landau model for the phase diagrams of the orthorhombic rare-earth manganites $r\mathrm{mno}_3$ (r = Eu, gd, tb, dy, ho). *Phys. Rev. B*, 82:064410, Aug 2010. 1

[8] Lev Davidovich Landau and Evgenii Mikhailovich Lifshitz. *Statistical physics*. Course of theoretical physics. Pergamon, London, 2nd edition, 1968. Trans. from the Russian. 3

[9] AP Levanyuk. Contribution to the theory of light scattering near the second-order phase transition points. *Sov. Phys.—JETP*, 9:571, 1959. 3

[10] VL Ginzburg and VL Ginzburgm. Some remarks on second order phase transitions and microscopic theory of ferroelectrics. *Fiz. Tverd. Tela*, 2(9):2031–2034, 1960. 3

[11] VL Ginzburg. Some remarks on phase transitions of the 2nd kind and the microscopic theory of ferroelectric materials. *Soviet Physics-Solid State*, 2(9):1824–1834, 1961. 3

[12] Boris A Strukov and Arkadi P Levanyuk. *Ferroelectric phenomena in crystals: physical foundations*. Springer Science & Business Media, 2012. 3, 5

[13] Lev Davidovich Landau, JS Bell, MJ Kearsley, LP Pitaevskii, EM Lifshitz, and JB Sykes. *Electrodynamics of continuous media*, volume 8. elsevier, 2013. 5

[14] Koichi Momma and Fujio Izumi. *VESTA3* for three-dimensional visualization of crystal, volumetric and morphology data. *Journal of Applied Crystallography*, 44(6):1272–1276, Dec 2011. 10, 97

[15] Yoshinori Tokura, Shinichiro Seki, and Naoto Nagaosa. Multiferroics of spin origin. *Reports on Progress in Physics*, 77(7):076501, 2014. 11, 12, 14, 97

[16] Shintaro Ishiwata, Yoshio Kaneko, Yusuke Tokunaga, Yasujiro Taguchi, Taka-hisa Arima, and Yoshinori Tokura. Perovskite manganites hosting versatile multiferroic phases with symmetric and antisymmetric exchange strictions. *Phys. Rev. B*, 81:100411, Mar 2010. 11

[17] S. Quezel, F. Tcheou, J. Rossat-Mignod, G. Quezel, and E. Roudaut. Magnetic structure of the perovskite-like compound tbmno3. *Physica B+C*, 86:916 – 918, 1977. 12

[18] T. Kimura, T. Goto, H. Shintani, K. Ishizaka, T. Arima, and Y. Tokura. Magnetic control of ferroelectric polarization. *Nature*, 426(6962):55–58, 11 2003. 12, 13, 17, 56, 97

[19] R. Kajimoto, H. Yoshizawa, H. Shintani, T. Kimura, and Y. Tokura. Magnetic structure of $tbmno_3$ by neutron diffraction. *Phys. Rev. B*, 70:012401, Jul 2004. 12

[20] M. Kenzelmann, A. B. Harris, S. Jonas, C. Broholm, J. Schefer, S. B. Kim, C. L. Zhang, S.-W. Cheong, O. P. Vajk, and J. W. Lynn. Magnetic inversion symmetry breaking and ferroelectricity in $tbmno_3$. *Phys. Rev. Lett.*, 95:087206, Aug 2005. 12

[21] S. B. Wilkins, T. R. Forrest, T. A. W. Beale, S. R. Bland, H. C. Walker, D. Mannix, F. Yakhou, D. Prabhakaran, A. T. Boothroyd, J. P. Hill, P. D. Hatton, and D. F. McMorrow. Nature of the magnetic order and origin of induced ferroelectricity in $tbmno_3$. *Phys. Rev. Lett.*, 103:207602, Nov 2009. 12

[22] T. Aoyama, K. Yamauchi, A. Iyama, S. Picozzi, K. Shimizu, and T. Kimura. Giant spin-driven ferroelectric polarization in tbmno3 under high pressure. *Nature Communications*, 5:4927 EP –, 09 2014. 13, 26, 56, 57, 58, 62, 65, 66, 74, 75, 99

[23] Kenta Shimamoto, Saumya Mukherjee, Sebastian Manz, Jonathan S. White, Morgan Trassin, Michel Kenzelmann, Laurent Chapon, Thomas Lippert, Manfred Fiebig, Christof W. Schneider, and Christof Niedermayer. Tuning the multiferroic mechanisms of tbmno3 by epitaxial strain. *Scientific Reports*, 7:44753 EP –, 03 2017. 13, 27, 83

[24] T. Kimura. Spiral magnets as magnetoelectrics. *Annual Review of Materials Research*, 37(1):387–413, 2007. 14

[25] IE Dzyaloshinskii. On the magneto-electrical effect in antiferromagnets. *Soviet Physics Jetp-Ussr*, 10(3):628–629, 1960. 17

[26] IE Dzyaloshinskii. Theory of helicoidal structures in antiferromagnets. 1. nonmetals. *Sov. Phys. JETP*, 19:960–971, 1964. 17

[27] Maxim Mostovoy. Ferroelectricity in spiral magnets. *Phys. Rev. Lett.*, 96:067601, Feb 2006. 17

[28] Mois Ilia Aroyo, Juan Manuel Perez-Mato, Cesar Capillas, Eli Kroumova, Svetoslav Ivantchev, Gotzon Madariaga, Asen Kirov, and Hans Wondratschek. Bilbao crystallographic server: I. databases and crystallographic computing programs. *Zeitschrift für Kristallographie-Crystalline Materials*, 221(1):15–27, 2006. 19

[29] P. W. Anderson. New approach to the theory of superexchange interactions. *Phys. Rev.*, 115:2–13, Jul 1959. 22

[30] I. Dzyaloshinsky. A thermodynamic theory of "weak" ferromagnetism of antiferromagnetics. *Journal of Physics and Chemistry of Solids*, 4(4):241 – 255, 1958. 24

[31] Tôru Moriya. New mechanism of anisotropic superexchange interaction. *Phys. Rev. Lett.*, 4:228–230, Mar 1960. 24

[32] Tôru Moriya. Anisotropic superexchange interaction and weak ferromagnetism. *Phys. Rev.*, 120:91–98, Oct 1960. 24

[33] L. X. Hayden, T. A. Kaplan, and S. D. Mahanti. Frustrated classical heisenberg and xy models in two dimensions with nearest-neighbor biquadratic exchange: Exact solution for the ground-state phase diagram. *Phys. Rev. Lett.*, 105:047203, Jul 2010. 26

[34] Y. S. Hou, J. H. Yang, X. G. Gong, and H. J. Xiang. Prediction of a multiferroic state with large electric polarization in tensile-strained tbmno$_3$. *Phys. Rev. B*, 88:060406, Aug 2013. 27

[35] I. A. Sergienko and E. Dagotto. Role of the dzyaloshinskii-moriya interaction in multiferroic perovskites. *Phys. Rev. B*, 73:094434, Mar 2006. 28, 56, 57

[36] Hosho Katsura, Naoto Nagaosa, and Alexander V. Balatsky. Spin current and magnetoelectric effect in noncollinear magnets. *Phys. Rev. Lett.*, 95:057205, Jul 2005. 29, 56, 57

[37] P. A. M. Dirac. Quantum mechanics of many-electron systems. *Proceedings of the Royal Society of London A: Mathematical, Physical and Engineering Sciences*, 123(792):714–733, 1929. 31

[38] E. Schrödinger. An undulatory theory of the mechanics of atoms and molecules. *Phys. Rev.*, 28:1049–1070, Dec 1926. 31

[39] L. H. Thomas. The calculation of atomic fields. *Mathematical Proceedings of the Cambridge Philosophical Society*, 23(5):542–548, 1927. 31, 34

[40] E. Fermi. Eine statistische methode zur bestimmung einiger eigenschaften des atoms und ihre anwendung auf die theorie des periodischen systems der elemente. *Zeitschrift für Physik*, 48(1):73–79, 1928. 31, 34

[41] P. A. M. Dirac. Note on exchange phenomena in the thomas atom. *Mathematical Proceedings of the Cambridge Philosophical Society*, 26(3):376–385, 1930. 31, 35

[42] E. Wigner and F. Seitz. On the constitution of metallic sodium. *Phys. Rev.*, 43:804–810, May 1933. 31

[43] E. Wigner and F. Seitz. On the constitution of metallic sodium. ii. *Phys. Rev.*, 46:509–524, Sep 1934. 31

[44] J. C. Slater. Wave functions in a periodic potential. *Phys. Rev.*, 51:846–851, May 1937. 31

[45] J. C. Slater. A simplification of the hartree-fock method. *Phys. Rev.*, 81:385–390, Feb 1951. 31

[46] W. Kohn and L. J. Sham. Self-consistent equations including exchange and correlation effects. *Phys. Rev.*, 140:A1133–A1138, Nov 1965. 31, 36, 38

[47] M. Born and R. Oppenheimer. Zur quantentheorie der molekeln. *Annalen der Physik*, 389(20):457–484, 1927. 32

[48] D. R. Hartree. The wave mechanics of an atom with a non-coulomb central field. part i. theory and methods. *Mathematical Proceedings of the Cambridge Philosophical Society*, 24(1):89–110, 1928. 33

[49] D. R. Hartree. The wave mechanics of an atom with a non-coulomb central field. part ii. some results and discussion. *Mathematical Proceedings of the Cambridge Philosophical Society*, 24(1):111–132, 1928. 33

[50] J. C. Slater. Note on hartree's method. *Phys. Rev.*, 35:210–211, Jan 1930. 33

[51] V. Fock. Näherungsmethode zur lösung des quantenmechanischen mehrkörperproblems. *Zeitschrift für Physik*, 61(1):126–148, 1930. 34

[52] E Fermi. Un metodo statistico par la determinazione di alcuno proprietà dell'atome. *Rendiconti Accademia Nazionale des Lincei, Cl. sci. fis., mat. e. nat*, 6, 1927. 34

[53] P. Hohenberg and W. Kohn. Inhomogeneous electron gas. *Phys. Rev.*, 136:B864–B871, Nov 1964. 35

[54] D. M. Ceperley and B. J. Alder. Ground state of the electron gas by a stochastic method. *Phys. Rev. Lett.*, 45:566–569, Aug 1980. 38

[55] A. D. Becke. Density-functional exchange-energy approximation with correct asymptotic behavior. *Phys. Rev. A*, 38:3098–3100, Sep 1988. 39

[56] Vladimir I. Anisimov, Jan Zaanen, and Ole K. Andersen. Band theory and mott insulators: Hubbard u instead of stoner i. *Phys. Rev. B*, 44:943–954, Jul 1991. 40

[57] Vladimir I Anisimov, F Aryasetiawan, and A I Lichtenstein. First-principles calculations of the electronic structure and spectra of strongly correlated systems: the lda + u method. *Journal of Physics: Condensed Matter*, 9(4):767, 1997. 40, 57, 74

[58] Hendrik J. Monkhorst and James D. Pack. Special points for brillouin-zone integrations. *Phys. Rev. B*, 13:5188–5192, Jun 1976. 41

[59] D. R. Hamann". Norm-conserving pseudopotentials. *Physical Review Letters*, 43(20):1494–1497, 1979. 41

[60] P. E. Blöchl". Projector augmented-wave method. *Physical Review B*, 50(24):17953–17979, 1994. 42

[61] R. D. King-Smith and David Vanderbilt. Theory of polarization of crystalline solids. *Phys. Rev. B*, 47:1651–1654, Jan 1993. 43

[62] FD Morrison, Y Luo, I Szafraniak, V Nagarajan, RB Wehrspohn, M Steinhart, JH Wendorff, ND Zakharov, ED Mishina, KA Vorotilov, et al. Ferroelectric nanotubes. *Rev. Adv. Mater. Sci*, 4:114–122, 2003. 45

[63] Alexei Gruverman and Andrei Kholkin. Nanoscale ferroelectrics: processing, characterization and future trends. *Reports on Progress in Physics*, 69(8):2443, 2006. 45

[64] JF Scott. Applications of modern ferroelectrics. *science*, 315(5814):954–959, 2007. 45

[65] Anna N. Morozovska, Maya D. Glinchuk, and Eugene A. Eliseev. Phase transitions induced by confinement of ferroic nanoparticles. *Phys. Rev. B*, 76:014102, Jul 2007. 45, 46

[66] A. N. Morozovska, M. D. Glinchuk, and E. A. Eliseev. Ferroelectricity enhancement in ferroelectric nanotubes. *Phase Transitions*, 80(1-2):71–77, 2007. 45, 46

[67] AP Levanyuk and R Blinc. Ferroelectric phase transitions in small particles and local regions. *Physical review letters*, 111(9):097601, 2013. 45, 46, 47

[68] M. Anoufa, J. M. Kiat, I. Kornev, and C. Bogicevic. Vortices of polarization in $BaTiO_3$ core-shell nanoceramics: Calculations based on ab initio derived Hamiltonian versus Landau theory. *Phys. Rev. B*, 88(14):144106, October 2013. 45, 46

[69] R. Herchig, K. Schultz, K. McCash, and I. Ponomareva. Terahertz sensing using ferroelectric nanowires. *Nanotechnology*, 24(4):045501, February 2013. 45

[70] B. Lee, S. M. Nakhmanson, and O. Heinonen. Strain induced vortex-to-uniform polarization transitions in soft-ferroelectric nanoparticles. *Applied Physics Letters*, 104(26):262906, June 2014. 45

[71] Laurent Baudry, Anaïs Sené, Igor A Luk'Yanchuk, Laurent Lahoche, and James F Scott. Polarization vortex domains induced by switching electric field in ferroelectric films with circular electrodes. *Physical Review B*, 90(2):024102, 2014. 45, 46

[72] Z. Gui, L.-W. Wang, and L. Bellaiche. Electronic Properties of Electrical Vortices in Ferroelectric Nanocomposites from Large-Scale Ab Initio Computations. *Nano Letters*, 15:3224–3229, May 2015. 45

[73] Ashley Bernal, Alexander Tselev, Sergei Kalinin, and Nazanin Bassiri-Gharb. Free-standing ferroelectric nanotubes processed via soft-template infiltration. *Advanced Materials*, 24(9):1160–1165, 2012. 45

[74] Gilles Philippot, Catherine Elissalde, Mario Maglione, and Cyril Aymonier. Supercritical fluid technology: A reliable process for high quality batio 3 based nanomaterials. *Advanced Powder Technology*, 25(5):1415–1429, 2014. 45

[75] Man Liu and Jie Wang. Giant electrocaloric effect in ferroelectric nanotubes near room temperature. *Sci. Rep.*, 5, 01 2015. 45

[76] Huaxiang Fu and L. Bellaiche. Ferroelectricity in barium titanate quantum dots and wires. *Phys. Rev. Lett.*, 91:257601, Dec 2003. 45

[77] Ivan I Naumov, L Bellaiche, and Huaxiang Fu. Unusual phase transitions in ferroelectric nanodisks and nanorods. *Nature*, 432(7018):737–740, 2004. 45

[78] Gregory Geneste, Eric Bousquet, Javier Junquera, and Philippe Ghosez. Finite-size effects in batio 3 nanowires. *Applied physics letters*, 88(11):112906–112906, 2006. 45

[79] AM Bratkovsky and AP Levanyuk. Continuous theory of ferroelectric states in ultrathin films with real electrodes. *Journal of Computational and Theoretical Nanoscience*, 6(3):465–489, 2009. 45, 46, 47, 50

[80] Engin Durgun, Ph Ghosez, R Shaltaf, Xavier Gonze, and J-Y Raty. Polarization vortices in germanium telluride nanoplatelets: A theoretical study. *Physical review letters*, 103(24):247601, 2009. 45

[81] AK Tagantsev, G Gerra, and N Setter. Short-range and long-range contributions to the size effect in metal-ferroelectric-metal heterostructures. *Physical Review B*, 77(17):174111, 2008. 45

[82] Jiawang Hong, G. Catalan, D. N. Fang, Emilio Artacho, and J. F. Scott. Topology of the polarization field in ferroelectric nanowires from first principles. *Phys. Rev. B*, 81:172101, May 2010. 45

[83] Javier Junquera and Philippe Ghosez. First-principles study of ferroelectric oxide epitaxial thin films and superlattices: role of the mechanical and electrical boundary conditions. *Journal of Computational and theoretical nanoscience*, 5(11):2071–2088, 2008. 46, 47

[84] A. K. Tagantsev and G. Gerra. Interface-induced phenomena in polarization response of ferroelectric thin films. *Journal of Applied Physics*, 100(5):–, 2006. 47

[85] S. Jin, T. H. Tiefel, M. McCormack, R. A. Fastnacht, R. Ramesh, and L. H. Chen. Thousandfold change in resistivity in magnetoresistive la-ca-mn-o films. *Science*, 264(5157):413–415, 1994. 55

[86] A P Ramirez. Colossal magnetoresistance. *Journal of Physics: Condensed Matter*, 9(39):8171, 1997. 55

[87] I. Loa, P. Adler, A. Grzechnik, K. Syassen, U. Schwarz, M. Hanfland, G. Kh. Rozenberg, P. Gorodetsky, and M. P. Pasternak. Pressure-induced quenching of the jahn-teller distortion and insulator-to-metal transition in $lamno_3$. *Phys. Rev. Lett.*, 87:125501, Aug 2001. 55, 61

[88] A. Yamasaki, M. Feldbacher, Y.-F. Yang, O. K. Andersen, and K. Held. Pressure-induced metal-insulator transition in $lamno_3$ is not of mott-hubbard type. *Phys. Rev. Lett.*, 96:166401, Apr 2006. 55, 61

[89] A. Y. Ramos, N. M. Souza-Neto, H. C. N. Tolentino, O. Bunau, Y. Joly, S. Grenier, J.-P. Itié, A.-M. Flank, P. Lagarde, and A. Caneiro. Bandwidth-driven nature of the pressure-induced metal state of lamno 3. *EPL (Europhysics Letters)*, 96(3):36002, 2011. 55, 59, 61

[90] Eric Bousquet and Andrés Cano. Non-collinear magnetism in multiferroic perovskites. *Journal of Physics: Condensed Matter*, 28(12):123001, 2016. 55, 89, 91

[91] Masahito Mochizuki and Nobuo Furukawa. Microscopic model and phase diagrams of the multiferroic perovskite manganites. *Phys. Rev. B*, 80:134416, Oct 2009. 56, 57

[92] Masahito Mochizuki, Nobuo Furukawa, and Naoto Nagaosa. Theory of spin-phonon coupling in multiferroic manganese perovskites $rmno_3$. *Phys. Rev. B*, 84:144409, Oct 2011. 56, 68, 84

[93] Sang-Wook Cheong and Maxim Mostovoy. Multiferroics: a magnetic twist for ferroelectricity. *Nat Mater*, 6(1):13–20, 01 2007. 56, 57

[94] A Munoz, MT Casáis, JA Alonso, MJ Martínez-Lope, JL Martinez, and MT Fernández-Díaz. Complex magnetism and magnetic structures of the metastable homno3 perovskite. *Inorganic chemistry*, 40(5):1020–1028, 2001. 56

[95] B. Lorenz, A. P. Litvinchuk, M. M. Gospodinov, and C. W. Chu. Field-induced reentrant novel phase and a ferroelectric-magnetic order coupling in $homno_3$. *Phys. Rev. Lett.*, 92:087204, Feb 2004. 56

[96] Ivan A. Sergienko, Cengiz Şen, and Elbio Dagotto. Ferroelectricity in the magnetic e-phase of orthorhombic perovskites. *Phys. Rev. Lett.*, 97:227204, Nov 2006. 56, 59

[97] Takuya Aoyama, Ayato Iyama, Katsuya Shimizu, and Tsuyoshi Kimura. Multiferroicity in orthorhombic rmno3 (r=dy, tb, and gd) under high pressure. *Phys. Rev. B*, 91:081107, Feb 2015. 56, 58

[98] G. Kresse and D. Joubert. From ultrasoft pseudopotentials to the projector augmented-wave method. *Phys. Rev. B*, 59:1758–1775, Jan 1999. 57, 74

[99] G. Kresse and J. Furthmüller. Efficient iterative schemes for *ab initio* total-energy calculations using a plane-wave basis set. *Phys. Rev. B*, 54:11169–11186, Oct 1996. 57, 74

[100] John P. Perdew, Adrienn Ruzsinszky, Gábor I. Csonka, Oleg A. Vydrov, Gustavo E. Scuseria, Lucian A. Constantin, Xiaolan Zhou, and Kieron Burke. Restoring the density-gradient expansion for exchange in solids and surfaces. *Phys. Rev. Lett.*, 100:136406, Apr 2008. 57, 74

[101] Igor Solovyev, Noriaki Hamada, and Kiyoyuki Terakura. Crucial role of the lattice distortion in the magnetism of $lamno_3$. *Phys. Rev. Lett.*, 76:4825–4828, Jun 1996. 57

[102] Pablo Rivero, Vincent Meunier, and William Shelton. Electronic, structural, and magnetic properties of $lamno_3$ phase transition at high temperature. *Phys. Rev. B*, 93:024111, Jan 2016. 59, 61

[103] Pablo Rivero, Vincent Meunier, and William Shelton. Uniaxial pressure-induced half-metallic ferromagnetic phase transition in $lamno_3$. *Phys. Rev. B*, 93:094409, Mar 2016. 59, 61

[104] Branton J. Campbell, Harold T. Stokes, David E. Tanner, and Dorian M. Hatch. *ISODISPLACE*: a web-based tool for exploring structural distortions. *Journal of Applied Crystallography*, 39(4):607–614, Aug 2006. 59

[105] Michael A. Carpenter and Christopher J. Howard. Symmetry rules and strain/order-parameter relationships for coupling between octahedral tilting and cooperative jahn–teller transitions in abx3 perovskites. i. theory. *Acta Crystallographica Section B*, 65(2):134–146, 2009. 60

[106] D. A. Mota, A. Almeida, V. H. Rodrigues, M. M. R. Costa, P. Tavares, P. Bouvier, M. Guennou, J. Kreisel, and J. Agostinho Moreira. Dynamic and structural properties of orthorhombic rare-earth manganites under high pressure. *Phys. Rev. B*, 90:054104, Aug 2014. 62, 63, 99

[107] Natalya S. Fedorova, Claude Ederer, Nicola A. Spaldin, and Andrea Scaramucci. Biquadratic and ring exchange interactions in orthorhombic perovskite manganites. *Phys. Rev. B*, 91:165122, Apr 2015. 66

[108] Shuai Dong, Rong Yu, Seiji Yunoki, J.-M. Liu, and Elbio Dagotto. Origin of multiferroic spiral spin order in the $r\mathrm{mno}_3$ perovskites. *Phys. Rev. B*, 78:155121, Oct 2008. 68

[109] I.O. Troyanchuk, N.V. Samsonenko, H. Szymczak, and A. Nabialek. Magnetic study of the ca1xeuxmno3(0x1) perovskites. *Journal of Solid State Chemistry*, 131(1):144 – 149, 1997. 69

[110] J.S. Smart. *Effective Field Theories of Magnetism*. Studies in physics and chemistry, 216. Saunders, 1966. 69

[111] P. W. Anderson and E. I. Blount. Symmetry considerations on martensitic transformations: "ferroelectric" metals? *Phys. Rev. Lett.*, 14:217–219, Feb 1965. 72, 83

[112] Youguo Shi, Yanfeng Guo, Xia Wang, Andrew J. Princep, Dmitry Khalyavin, Pascal Manuel, Yuichi Michiue, Akira Sato, Kenji Tsuda, Shan Yu, Masao Arai, Yuichi Shirako, Masaki Akaogi, Nanlin Wang, Kazunari Yamaura, and Andrew T. Boothroyd. A ferroelectric-like structural transition in a metal. *Nat Mater*, 12(11):1024–1027, 11 2013. 72, 83

[113] Li Yin, Wenbo Mi, and Xiaocha Wang. Ferroelectric metal in tetragonal bicoo3/bifeo3 bilayers and its electric field effect. *Scientific Reports*, 6:20591 EP –, 02 2016. 72, 83

[114] T. H. Kim, D. Puggioni, Y. Yuan, L. Xie, H. Zhou, N. Campbell, P. J. Ryan, Y. Choi, J. W. Kim, J. R. Patzner, S. Ryu, J. P. Podkaminer, J. Irwin, Y. Ma, C. J. Fennie, M. S. Rzchowski, X. Q. Pan, V. Gopalan, J. M. Rondinelli, and C. B. Eom. Polar metals by geometric design. *Nature*, 533(7601):68–72, 05 2016. 72, 73, 74, 83

[115] Nicole A. Benedek and Turan Birol. 'ferroelectric' metals reexamined: fundamental mechanisms and design considerations for new materials. *J. Mater. Chem. C*, 4:4000–4015, 2016. 72, 83

[116] Alessio Filippetti, Vincenzo Fiorentini, Francesco Ricci, Pietro Delugas, and Jorge Íñiguez. Prediction of a native ferroelectric metal. *Nature Communications*, 7:11211 EP –, 04 2016. 73, 74

[117] O. L. Makarova, I. Mirebeau, S. E. Kichanov, J. Rodriguez-Carvajal, and A. Forget. Pressure-induced change in the magnetic ordering of $tbmno_3$. *Phys. Rev. B*, 84:020408, Jul 2011. 74

[118] Masao Nakamura, Yusuke Tokunaga, Masashi Kawasaki, and Yoshinori Tokura. Multiferroicity in an orthorhombic ymno3 single-crystal film. *Applied Physics Letters*, 98(8):082902, 2011. 74

[119] Jun Hee Lee and Karin M. Rabe. Epitaxial-strain-induced multiferroicity in $srmno_3$ from first principles. *Phys. Rev. Lett.*, 104:207204, May 2010. 74

[120] R. Jaramillo, Sieu D. Ha, D. M. Silevitch, and Shriram Ramanathan. Origins of bad-metal conductivity and the insulator-metal transition in the rare-earth nickelates. *Nat Phys*, 10(4):304–307, 04 2014. 74

[121] Valentina Bisogni, Sara Catalano, Robert J. Green, Marta Gibert, Raoul Scherwitzl, Yaobo Huang, Vladimir N. Strocov, Pavlo Zubko, Shadi Balandeh, Jean-Marc Triscone, George Sawatzky, and Thorsten Schmitt. Ground-state oxygen holes and the metal–insulator transition in the negative charge-transfer rare-earth nickelates. *Nature Communications*, 7:13017 EP –, 10 2016. 74

[122] D. Rubi, C. de Graaf, C. J. M. Daumont, D. Mannix, R. Broer, and B. Noheda. Ferromagnetism and increased ionicity in epitaxially grown $tbmno_3$ films. *Phys. Rev. B*, 79:014416, Jan 2009. 74

[123] X. Marti, V. Skumryev, C. Ferrater, M. V. García-Cuenca, M. Varela, F. Sánchez, and J. Fontcuberta. Emergence of ferromagnetism in antiferromagnetic tbmno3 by epitaxial strain. *Applied Physics Letters*, 96(22):222505, 2010. 74, 83

[124] K. Shimamoto, S. Mukherjee, S. Manz, J. S. White, M. Trassin, M. Kenzelmann, L. Chapon, T. Lippert, M. Fiebig, C. W. Schneider, and C. Niedermayer. Tuning the multiferroic mechanisms of TbMnO3 by epitaxial strain. *ArXiv e-prints*, September 2016. 74

[125] Masahito Mochizuki". Spin model of magnetostrictions in multiferroic mn perovskites. *Physical Review Letters*, 105(3), 2010. 84

[126] EF Bertaut, GT Rado, and H Suhl. Magnetism iii. *Edited by Rado GT, Suhl H. New York: Academic*, 149, 1963. 89

[127] R. L. White. Review of recent work on the magnetic and spectroscopic properties of the rareearth orthoferrites. *Journal of Applied Physics*, 40(3):1061–1069, 1969. 89

[128] T. Yamaguchi. Theory of spin reorientation in rare-earth orthochromites and orthoferrites. *Journal of Physics and Chemistry of Solids*, 35(4):479 – 500, 1974. 89, 90

[129] La Chen, Tongwei Li, Shixun Cao, Shujuan Yuan, Feng Hong, and Jincang Zhang. The role of 4f-electron on spin reorientation transition of ndfeo3: A first principle study. *Journal of Applied Physics*, 111(10):103905, 2012. 90

[130] C.-Y. Kuo, Y. Drees, M. T. Fernández-Díaz, L. Zhao, L. Vasylechko, D. Sheptyakov, A. M. T. Bell, T. W. Pi, H.-J. Lin, M.-K. Wu, E. Pellegrin, S. M. Valvidares, Z. W. Li, P. Adler, A. Todorova, R. Küchler, A. Steppke, L. H. Tjeng, Z. Hu, and A. C. Komarek. $k = 0$ magnetic structure and absence of ferroelectricity in smfeo3. *Phys. Rev. Lett.*, 113:217203, Nov 2014. 90

[131] Hui Shen, Zhenxiang Cheng, Fang Hong, Jiayue Xu, Shujuan Yuan, Shixun Cao, and Xiaolin Wang. Magnetic field induced discontinuous spin reorientation in erfeo3 single crystal. *Applied Physics Letters*, 103(19):192404, 2013. 90

[132] Yusuke Tokunaga, Nobuo Furukawa, Hideaki Sakai, Yasujiro Taguchi, Taka-hisa Arima, and Yoshinori Tokura. Composite domain walls in a multiferroic perovskite ferrite. *Nat Mater*, 8(7):558–562, 07 2009. 91

[133] Thomas L Gilbert. A phenomenological theory of damping in ferromagnetic materials. *IEEE Transactions on Magnetics*, 40(6):3443–3449, 2004. 91

[134] Thomas Andrew Ostler. *Computer Simulations of Ultrafast Magnetisation Reversal*. PhD thesis, University of York, 2012. 92

List of Publications

1. Qiu, R., Bousquet, E., and Cano, A., (2015). Ferroelectric instability in nanotubes and spherical nanoshells. *EPL (Europhysics Letters)*, 112(3), 37006.
   This publication includes the main contents of Chapter 3.

2. Qiu, R., Bousquet, E. and Cano, A., (2017). Pressure-induced insulator-metal transition in $EuMnO_3$. *Journal of physics: Condensed matter*, 29(30), 305801.
   This publication includes the main contents of Chapter 4.

3. Qiu, R., Bousquet, E. and Cano, A., Epitaxial-strain-induced multiferroic and polar metallic phases in $R\mathrm{MnO}_3$. In preparation.
   This article will include the main contents of Chapter 5.

Abstract

In this thesis, we present a theoretical study of two types of ferroic instabilities: the ferroelectric instability in novel confined geometries and magnetic instabilities controlled by the distortion of the underlying crystal lattice. On the one hand, we consider in detail the ferroelectric instability, specifically, in the nanotubes and the spherical nanoshells and develop a phenomenological theory for describing such an instability. We determine how the emergence of polarization is affected by the thickness of the nanoparticle, the dielectric properties of the surrounding media and the interfacial boundary conditions. We find an intriguing topological finite-size effect that can promote an unexpected competition between two different types of distribution of polarization – irrotational and vortex-like – in the ultra-thin limit. One the other hand, we employ a different formalism to investigate the structural, electronic and magnetic properties of the rare-earth manganites. Specifically, we conduct a theoretical investigation from first-principles calculations. First, we predict a pressure-induced A-AFM insulator to FM metal transition on $EuMnO_3$ under hydrostatic pressure, that is unprecedented in the multiferroic rare-earth manganites $RMnO_3$. This investigation is extended to the study to the epitaxial strain effects on both $EuMnO_3$ and $TbMnO_3$ thin films. We show that epitaxial strain generates a much richer phase diagram compared to hydrostatic pressure. We predict novel magnetically-induced insulator – metal and polar – non-polar transitions. More specifically, we find that both the multiferroic E-AFM order and the polar metallic E*-AFM state are stabilized in $TbMnO_3$ by means of epitaxial strain. In the contrast, we find a novel epitaxial-strain-induced multiferroic E-AFM state in $EuMnO_3$ that cannot be obtained by means of just hydrostatic pressure.

Résumé

Dans cette thèse de doctorat nous présentons une étude théorique de deux types d'instabilités ferroélectriques: celles apparaissant dans des géométries confinés et celles induites par le magnétisme dans dans composés massifs de structure perovskite. Dans une première partie nous abordons le problème des instabilités ferroélectriques apparaissant dans des nanotubes et des nanocoquilles où nous développons un modèle théorique phénoménologique approprié à ces structures. Nous étudions comment l'émergence de la polarisation est affectée par (i) l'épaisseur des nanostructures, (ii) par la réponse diélectrique des matériaux environant la couche ferroélectrique et (iii) les conditions aux interfaces. Nous observons un effet de taille finie topologique qui peut promouvoir une compétition inhabituelle entre deux types de distribution de la polarization, irrotationel et en vortex, dans la limite des très petites épaisseurs. Dans une deuxième partie nous utilisons des calculs *ab-initio* à base de la théroie de la fonctionnelle de la densité pour étudier les instabilités ferroélectriques des perovskites manganites à base de terres rares ($RMnO_3$). A partir de ces calculs nous prédisons qu'il est possible d'induire une transition de phase sous pression dans $EuMnO_3$ le faisant transiter d'un ordre antiferromagnétique de type A isolant vers un ordre ferromagnétique métallique sous pression. Ce type de transition n'avait jamais été reporté précédemment dans les matériaux $RMnO_3$. Nous étendons ensuite cette analyse à l'étude des effets de strain épitaxial dans les films minces de $TbMnO_3$ et $EuMnO_3$. Nos résultats montrent que le diagramme de phase sous contrainte d'épitaxie est bien plus riche que celui sous pression hydrostatique. Nous trouvons que les types antiferromagnétiques E-AFM et E*-AFM sont stabilisés dans le cas de $TbMnO_3$, où le type E*-AFM est une phase métallique polaire. Dans le cas de $EuMnO_3$, nous trouvons une phase antiferromagnétique de type E qui n'a pas été observée sous pression hydrostatique.